eman ta zabal zazu

Universidad del País Vasco
Euskal Herriko Unibertsitatea

Digital Quantum Simulations of Spin Models with Superconducting Circuits

Urtzi Las Heras

Supervisor:

Prof. Enrique Solano

Departamento de Química Física
Facultad de Ciencia y Tecnología
Universidad del País Vasco UPV/EHU

Leioa, April 2017

Life is a play that does not allow testing. So, sing, cry, dance, laugh and live intensely, before the curtain closes and the piece ends with no applause.

Charlie Chaplin

This report, by its very length, defends itself against the risk of being read.

Winston Churchill

Contents

Abstract

In the last years, the fields of quantum technologies and quantum information have undergone dramatic advances, which suggest the advent of the second quantum revolution. In particular, superconducting circuits have experienced rapid and drastic technological growth. In this sense, architectures facilitating large numbers of quantum bits, with coherence times that allow for hundreds of quantum gates, are now feasible. On the other hand, quantum simulations are one of the most promising branches of quantum information, where digital and analog protocols allow us to reproduce a variety of systems with versatility.

Spin models, along with light-matter interactions, are one of the most studied topics in many-body systems. The microscopic description of magnetism is a relevant question that one can study in condensed matter physics and it has applications in many different disciplines including quantum field theory, metamaterials, and neuroscience models, among others. Quantum versions of spin models have interesting physical properties and, due to the high complexity of these quantum systems, the analysis with classical computers is a tough task. Hence, quantum platforms such as superconducting circuits are wonderful candidates to probe spin system's features.

In this Thesis, we propose several digital quantum simulations of quantum spin models with superconducting circuits, in which light-matter and spin-spin interactions are reproduced. Exploiting natural interactions in circuit quantum electrodynamics setups, in which qubits are coupled capacitively or by quantum buses, dynamics of prototypical spin models such as Ising and Heisenberg models are implemented and experimentally analyzed. On the other hand, Rabi and Dicke Hamiltonians are simulated with a digital-analog quantum simulation approach. For this purpose,

analog-block interactions are composed in a digital manner to exploit the resources of quantum simulators. Furthermore, we study the combination of digital methods with an adiabatic quantum computing approach, which has been implemented in an experiment involving up to nine qubits. Finally, genetic algorithms are considered as a tool to improve not only digital quantum simulation protocols but also fidelity in quantum gates. Therefore, they allow us to enhance the fidelity of quantum information processing protocols via the introduction of a new paradigm, which is conceptually distinct from the conventional approach via quantum error correcting codes.

We believe that this Thesis provides the first step towards digital quantum simulations with superconducting circuit architectures, which offer considerable potential for surpassing classical simulators in the search of quantum supremacy. We hope that our results motivate further theoretical and experimental works involving many-body spin systems and complex light-matter interactions.

Acknowledgements

MANY people may think that this Thesis is the result of the work during my PhD, which is only partially true. I cannot forget that starting the PhD in physics is just the consequence of the decisions that I have been taken since I reached the age of reason, and these decisions come from nothing more than the sum of the influences of people around me and my own essence. Since the protocol says that acknowledgements cannot be larger than the results of the Thesis, I had to reduce it infinitely, otherwise the list would be endless.

First, I would like to thank my PhD supervisor Prof. Enrique Solano for giving me the chance to start this scientific adventure. I highly value his guidance and support since I knocked his door looking for a Bachelor Thesis. At that moment, I never could have imagined I was able to do a PhD, but due to his ability to find the most motivating words, today I think I am prepared to accept any new challenge. Indeed, during these years I have developed useful skills not only for the scientific world, but for my everyday life.

Undoubtedly, this Thesis could not be written without the help of sages that have guided me reaching the peaks of highest objectives. My warmest thanks to Prof. Íñigo Egusquiza for giving so many pieces of wisdom with the maximum nearness. I would like to thank Dr. Lucas Lamata for the wonderful discussions and the invaluable attention that has made me feel confident so many times. Finally, it is more than an obligation for me to thank Dr. Mikel Sanz for supporting me all these years being, besides a committed postdoctoral fellow, a very close friend.

I want to dedicate some words to all the members of QUTIS group and university friends who have contributed to create an incredible scientific environment to work, but also friendly and open-mind atmosphere to share our interests and worries. During the PhD, I have found new features in myself that are pure reflections of the characters around, including the search of perfection, the slaughter capacity, the laconic use of words, the art, the inner zen, the empathy, the sarcasm and the good humor even in the most outrageous moments, the competitiveness (especially when playing ping-pong), and the unshakable smiles among others in a never-ending list.

Throughout the PhD, I have had the privilege of interacting and collaborating with top-level researchers from all over the world. I would like to thank Yves Salathé, Mintu Mondal, Dr. Steffan Filipp and Prof. Andreas Wallraff from ETH Zurich for the wonderful discussions and interest in the collaborations in the first steps of my PhD. Special thanks to Marios Kounalakis, Dr. Nathan Langford and Prof. Leonardo Di Carlo who, besides inviting me to the lab in Delft University of Technology with a nice welcoming by the whole group, had the patience to tell me the complexity of the experimental world. Many thanks to Dr. Rami Barends from Google for sharing not only his knowledge and scientific opinions, but also the passion in our work. I would like to express my gratitude to Stefan Pogorzalek, Dr. Kirill Fedorov, Dr. Frank Deppe, Dr. Achim Marx and Prof. Rudolph Gross, for inviting me to visit Walther Meissner Institute so many times, in which the nice environment and discussions have provided plenty of results in my PhD. Many thanks to Dr. Juan José García Ripoll for the great teamwork and help. Warm thanks to Dr. Ryan Sweke, who has always been disposed to discuss about any topic and has helped to improve my works many times. Finally, I would like to thank to all the colleges whose questions and suggestions in workshop's poster sessions or coffee breaks have contributed to the development of this Thesis.

To conclude, I could not forgive myself if I forgot the people that have been around me. Thanks to my friends for the long evenings that become short with each laugh. Many thanks to the mates of the team of Brazilian jiu jitsu, who have destroyed my body and released my soul training in the most stressing days. Thanks to my family, especially to my parents and my brother, whose love and support always have been there no matter what, where, or when. I would like to thank Kitty,

for teaching me to go ahead in the hardest moments without a single complain, and Shira, for everyday welcoming me with an unstoppable joy. Finally, my most sincere thanks to my love, Lara, who is the reason to get up every morning, since she is the one that maximizes the unique variable that matters in my life, happiness.

Resumen

A lo largo de la historia, el ser humano, consciente de su incapacidad natural para realizar diversas tareas, ha utilizado herramientas que le han permitido afrontar de forma cada vez más satisfactoria los problemas de cada época. Estos avances que van desde las lanzas prehistóricas para cazar mamuts hasta los aviones actuales para llegar al otro lado del mundo en cuestión de horas, han provisto a los humanos de habilidades que la naturaleza no nos ha brindado. No es distinto el caso particular de la computación. Desde niños hemos aprendido a hacer uso de elementos más allá de nuestra mente analítica para la realización de todo tipo de cálculos. Contar con los dedos, utilizar un ábaco o un papel y un lápiz, y en última instancia hacer uso de un ordenador son solo algunos ejemplos de ello. Hay quien podría pensar erróneamente que los superordenadores con tecnología puntera son capaces de resolver los problemas computacionales más complejos pero la verdad es que posiblemente nunca lleguen a conseguirlo.

Las primeras máquinas computadoras tenían un único propósito, es decir, estaban programadas por construcción con una única función, recibiendo el nombre de máquinas analógicas. En caso de querer realizar otra tarea, las máquinas analógicas debían desmontarse y reconstruirse, lo que resultaba ineficiente. Con el tiempo se introdujo la posibilidad de programar las computadoras sin la necesidad de alterar los distintos componentes físicos, permitiendo así la posibilidad de introducir nuevas funciones no consideradas durante el diseño y montaje de las máquinas. Estas reciben el nombre de computadoras digitales y su estructura se basa en tres partes: una entrada de datos, una función que actúa sobre estos mediante una serie de puertas lógicas y una salida de datos. Diseñando un algoritmo que codifique el problema que

se quiere resolver, la salida de datos da la solución a dicho problema. Además, debido a la posibilidad de programar el algoritmo, se puede resolver una gran variedad de problemas sin la necesidad de hacer ajustes mecánicos en la máquina.

La tecnología en el ámbito de la computación ha tenido un crecimiento sin precedentes desde la implementación del transistor, siendo esta la primera revolución cuántica. Antes de este, los ordenadores funcionaban con válvulas o tubos de vacío de gran tamaño que requerían altas cantidades de energía además de necesitar un tiempo de calentamiento. Los transistores, dispositivos que transfieren señales eléctricas unidireccionalmente, mejoraron todas las cualidades de las válvulas, especialmente en rapidez y fiabilidad. Estos elementos, cuyos efectos físicos se basan en efectos cuánticos, generaron una revolución en la historia de la computación. Como predijo Moore, la densidad de transistores en un microprocesador es duplicada cada dos años. De esta forma, hoy día disponemos de ordenadores programables de gran capacidad de cálculo aunque todavía no están a la altura de simular la complejidad de los sistemas cuánticos.

La mecánica cuántica se desarrolló durante la primera mitad del siglo XX, revelando una física exótica y contraintuitiva para muchos. Así, la interacción entre luz y materia a escala microscópica comenzó a describirse mediante modelos basados en interacciones entre partículas y campos cuánticos. Los efectos puramente cuánticos de la superposición y entrelazamiento implican una dificultad inmensa a la hora de simularlos con un ordenador que codifica los datos en bits, dígitos binarios con estados 0 o 1. Una máquina cuántica estaría compuesta de bits cuánticos (qubits) cuyos estados serían superposiciones de los estados 0 y 1, y que podrían entrelazarse con otros qubits. Así pues, el ordenador cuántico no solo posibilitaría este tipo de simulaciones sino también avanzados protocolos en el ámbito de la teoría de la información, como la factorización en números primos o la criptografía de alta seguridad. Por esa razón, la comunidad científica ha puesto grandes esfuerzos en controlar los sistemas cuánticos, dando lugar a diversas tecnologías cuánticas como iones atrapados, sistemas fotónicos o circuitos superconductores. Mediante el uso de estas tecnologías se puede estudiar el comportamiento de las propiedades cuánticas de modelos físicos en un laboratorio. Para ello, nuestro sistema cuántico ha de cumplir una serie de requisitos como la capacidad de inicializar el sistema en un estado conocido, la posibilidad

de implementar una evolución o una serie de puertas lógicas, así como la realización de medidas que den información del estado del sistema.

En esta Tesis, mostramos las primeras propuestas de simulaciones cuánticas digitales de modelos de espines en la tecnología cuántica de circuitos superconductores, que adquieren un comportamiento cuántico cuando su temperatura es de alrededor de 20 mK. En primer lugar estudiamos los distintos tipos de dinámicas que gobiernan estos sistemas y las consiguientes puertas lógicas que pueden implementarse. Además, tenemos en cuenta las limitaciones de la tecnología actual considerando los tiempos de coherencia cuántica y las imperfecciones experimentales a la hora de ejecutar puertas lógicas en uno o varios qubits. Una vez conocidas en detalle las capacidades de los circuitos con interacciones de electrodinámica cuántica, podemos realizar varias propuestas para la simulación de modelos cuánticos, en concreto, modelos de espines. El espín es una propiedad de las partículas elementales que interacciona mediante el acoplo dipolar magnético. De esta forma, estos modelos estudian las propiedades de los sistemas de partículas con espín alineados en cadenas o redes en 2 y 3 dimensiones. Adicionalmente, los modelos espín-bosón consideran las interacciones entre estos dos tipos de partículas que en muchos casos se refiere al acoplo entre la materia y la radiación electromagnética. Para simular estas interacciones, los circuitos superconductores se diseñan de tal forma que se comporten como un sistema cuántico de dos niveles, conocido como qubit superconductor. Acoplando varios de estos qubits, ya sea capacitivamente o mediante una linea de transmisión de microondas, las interacciones entre varios espines son reproducidas. Por otra parte, la línea de transmisión actúa como un resonador, por lo que los qubits también interactúan con los modos electromagnéticos dentro de la línea resultando una genuina interacción entre la luz y la materia.

Una vez establecido un mapeo entre el estado de los espines y el de los qubits superconductores, y considerando los modos bosónicos del resonador, podemos comenzar a introducir dinámicas de modelos de espín en nuestro sistema. Es necesario remarcar dos tipos distintos dentro del campo de las simulaciones cuánticas: las analógicas y las digitales. De forma similar a las primeras máquinas computadoras, los simuladores analógicos solo son capaces de reproducir dinámicas muy limitadas, siendo estas las que aparecen de forma natural en el sistema. Así pues, la dinámica de aquellos modelos que sea igual que la de un simulador analógico podrá ser testada

experimentalmente en estas plataformas. Por otra parte tenemos los simuladores cuánticos digitales que permiten la simulación de dinámicas con una gran generalidad. Estas simulaciones se basan en evoluciones realizadas por una serie discretizada de puertas lógicas. Siguiendo la fórmula de Trotter-Suzuki-Lie, la evolución unitaria de un sistema gobernado por un Hamiltoniano H puede ser descompuesta en una serie de evoluciones de Hamiltonianos H_k, donde la suma de estos es igual al Hamiltoniano simulado $H = \sum_k H_k$. Además, esta fórmula predice un error teórico en la simulación que depende de los conmutadores entre los Hamiltonianos aplicados y del tiempo simulado. Afortunadamente este error puede reducirse repitiendo la serie de puertas lógicas a la vez que se reduce el tiempo de ejecución de cada una. Lloyd, al proponer los simuladores cuánticos digitales, tomó como ejemplo la acción de aparcar un coche en línea. Un coche que se quiere aparcar a su derecha (Hamiltoniano H) tiene que descomponer su movimiento en varios pasos en los que se mueve diagonalmente hacia atrás y hacia adelante (Hamiltonianos H_K). Como resultado, el coche termina aparcando correctamente a pesar de la dependencia del tamaño del hueco. Cuando este es grande, el coche deberá realizar pocos movimientos (error mayor), pero si es pequeño se precisarán muchos movimientos. En el límite, el coche necesitará infinitos movimientos para aparcar en un hueco de su misma longitud (error nulo). Así pues, el uso de técnicas digitales permite implementar una mayor cantidad de dinámicas que las que aparecen naturalmente en los circuitos superconductores como demostramos en las propuestas reunidas en esta Tesis.

Dos de los modelos de espín más conocidos son el de Heisenberg y el de Ising, los cuales describen la física de materiales ferromagnéticos y antiferromagnéticos. Estas interacciones no aparecen de forma natural en la tecnología de circuitos por lo que hay que simularlas digitalmente. Afortunadamente la dinámica de dos qubits acoplados por un resonador en el régimen dispersivo es gobernada por la interacción XY que tiene un gran parecido con los modelos de Heisenberg e Ising. En el Capítulo 2 demostramos que realizando rotaciones sobre los qubits, antes y después de las evoluciones unitarias bajo la interacción XY, podemos cambiar las direcciones de la interacción consiguiendo los modelos XZ e YZ. Mediante una descomposición de Trotter, la suma de las tres interacciones da como resultado el modelo de Heisenberg que además tiene error digital nulo para dos qubits. De forma similar el modelo

de Ising se logra ejecutando una evolución XY seguida por otra con rotaciones locales sobre un único qubit antes y después. Considerando un campo transverso que se simula con rotaciones locales, este modelo requiere de varias repeticiones en la descomposición de Trotter para limitar el error digital. Por tanto, analizamos la cantidad de puertas lógicas requeridas para la simulación y la fidelidad de estas con parámetros realistas. Esta propuesta ha sido llevada al laboratorio por el grupo del Prof. Andreas Wallraff en el ETH Zürich en colaboración con el grupo QUTIS del Prof. Enrique Solano. Aquí, los modelos XY, Heisenberg e Ising con campo transverso fueron implementados en un chip sobre dos qubits acoplados mediante un resonador.

Seguidamente hacemos un análisis de cómo simular el modelo de Rabi cuántico que describe la interacción luz-materia. La física de este modelo es diversa y a pesar de ser propuesto hace ochenta años a día de hoy aún quedan regímenes por explorar. Este modelo consta de un espín y un modo bosónico, los cuales se pueden simular mediante un qubit superconductor acoplado a una guía de transmisión. Por el contrario, el modelo efectivo que aparece en estos sistemas es el de Jaynes-Cummings, un régimen específico del modelo de Rabi cuántico, y se requiere de Trotterización para lograr el modelo general. Haciendo uso de rotaciones locales en el estado del qubit, antes y después de la interacción Jaynes-Cummings, conseguimos la interacción anti-Jaynes-Cummings. Esta, en vez de intercambiar excitaciones entre el qubit y el resonador, excita y desexcita los dos sistemas a la vez. Estas interacciones son complejas en el sentido de que involucran modos bosónicos que actúan en un espacio de Hilbert de dimensión infinita. Debido a esto, la descomposición de estos campos en qubits en una simulación puramente digital, como lo haría un ordenador codificando la información en bits, es muy ineficiente comparado con la implementación de puertas lógicas basadas en dinámicas analógicas. Así, con una serie digitalizada de evoluciones unitarias compuesta por dos interacciones analógicas Jaynes-Cummings y dos rotaciones locales, se obtiene el modelo de Rabi en una simulación cuántica que recibe el nombre de digital-analógica. Además, demostramos que la flexibilidad en los parámetros de los circuitos permite acceder a regímenes especialmente interesantes como lo son los de los acoplos “ultrastrong” y “deep strong” o la ecuación de Dirac. En este apartado mostramos varias simulaciones numéricas estimando la cantidad de

repeticiones de Trotter requeridas para obtener fidelidades altas. Finalmente, proponemos la extensión de esta simulación digital-analógica para sistemas de varios qubits con dinámicas tipo Tavis-Cummings para la simulación del modelo de Dicke. La implementación experimental de este trabajo ha sido realizada recientemente por el grupo del Prof. Leonardo DiCarlo en la Universidad Técnica de Delft, obteniendo unos resultados que han llegado a superar los límites experimentales estimados en la propuesta inicial.

En el Capítulo 4 de esta Tesis, consideramos la implementación de varios modelos de cadenas de espines en sistemas con acoplos capacitivos entre qubits vecinos, así como acoplos no locales mediante el uso de resonadores. De esta forma, además de las interacciones empleadas en los apartados anteriores, podemos introducir interacciones de tipo ZZ entre qubits que estén conectados en nuestro sistema físico, pudiendo realizar una simulación del modelo de Ising con menos puertas lógicas. Además, demostramos que simulaciones cuánticas de modelos de mayor complejidad, con acoplos locales entre qubits que a su vez están acoplados al campo bosónico del resonador, son factibles con este tipo de arquitecturas. De hecho, proponemos la interacción Tavis-Cummings con acoplo entre espines vecinos de tipo Ising y estudiamos la forma de implementar interacciones entre múltiples cuerpos. Estas son propias de modelos de materia condensada y en este trabajo analizamos numéricamente el caso de interacciones entre tres cuerpos. Adicionalmente, proponemos el uso de técnicas digitales para la realización de evoluciones adiabáticas. En estas, el sistema se inicializa en el estado base de un Hamiltoniano conocido, y variando el Hamiltoniano que gobierna la evolución a lo largo de un cierto tiempo y tomando las precauciones pertinentes para no excitar al sistema, el estado del sistema pasa a ser el estado base del Hamiltoniano final. Nosotros demostramos que la Trotterización permite realizar este tipo de protocolos y revisamos los resultados experimentales obtenidos por el grupo del Prof. John M. Martinis en Google/Universidad de California Santa Bárbara en colaboración con el grupo QUTIS del Prof. Enrique Solano, donde se realizan evoluciones adiabáticas cuánticas digitalizadas de modelos de espines con interacciones a primeros vecinos.

Por último, proponemos el uso de algoritmos genéticos en las simulaciones digitales cuánticas. Los algoritmos genéticos son protocolos inspirados en sistemas biológicos que con el paso de los años han conseguido una adaptación al entorno

que maximiza las probabilidades de supervivencia mediante la combinación y la mutación genéticas. De esta forma son capaces de encontrar soluciones de problemas de gran robustez en tiempos mucho menores que los algoritmos de optimización de fuerza bruta que tienen que procesar todos los posibles casos. En nuestras anteriores propuestas hemos descompuesto los modelos simulados en una suma de Hamiltonianos implementables en nuestro sistema. No obstante, mediante el uso de algoritmos genéticos es posible implementar estructuras de Hamiltonianos que no cumplen esta regla dando pie a simulaciones de alta fidelidad que requieren de menos recursos. Así pues, en este trabajo demostramos numéricamente que los algoritmos genéticos aportan estructuras de puertas lógicas implementables en sistemas de qubits superconductores con acoplos capacitivos para la simulación de modelos de espines de tipo Heisenberg e Ising. Por otra parte, como alternativa a los códigos de corrección de errores cuánticos, consideramos los algoritmos genéticos para la supresión de errores experimentales en puertas lógicas y analizamos la construcción de la puerta Controlled-NOT (CNOT). Para ello, tomamos un grupo de puertas CNOT con errores arbitrarios y el algoritmo genético determina una estructura de puertas lógicas sobre qubits que tienen los roles de control, objetivo y ancillas. Así, obtenemos como resultado una puerta CNOT con un error inferior que cualquiera de las puertas empleadas en el protocolo, siendo robusta frente a pequeñas alteraciones en las puertas componentes.

En conclusión, creemos que los resultados presentados en esta Tesis han contribuido al campo puntero de simulaciones cuánticas digitales en circuitos superconductores. Hemos analizado algunas de las primeras propuestas para la simulación digital de modelos de espines, considerando en todo momento la tecnología experimental de vanguardia para una aplicación directa. Tanto es así que estos trabajos han tenido un impacto experimental inmediato, generando fructíferas colaboraciones internacionales. Se espera que la tecnología de circuitos superconductores mejore, dando lugar a una mejor controlabilidad con menores errores experimentales, mayores tiempos de coherencia y una mayor variedad de interacciones implementables. De este modo sería posible simular sistemas complejos empleando códigos de corrección de errores en ordenadores cuánticos con todo tipo de aplicaciones en física de materiales, bioquímica o física médica entre otros, logrando una supremacía cuántica frente a los ordenadores clásicos. En cualquier caso, aún hay cantidad de problemas

por resolver desde un punto de vista teórico, como la creación de un código universal de corrección de errores que involucre bloques de interacciones analógicas. El desarrollo de este y otros retos en el ámbito de la información y tecnologías cuánticas nos encamina hacia la segunda revolución cuántica que tendrá aplicaciones directas en la vida cotidiana. No olvidemos que cuando se construyeron los primeros ordenadores nadie imaginó que unos años más tarde cualquier persona podría tener un teléfono móvil en el bolsillo con capacidad para procesar información de una red de datos a nivel mundial en tiempo real.

List of Publications

Published Articles

1. U. Las Heras, A. Mezzacapo, L. Lamata, S. Filipp, A. Walraff, and E. Solano, *Digital Quantum Simulation of Spin Systems in Superconducting Circuits*, Phys. Rev. Lett. **112**, 200501 (2014).

2. A. Mezzacapo, U. Las Heras, J. S. Pedernales, L. DiCarlo, E. Solano, and L. Lamata, *Digital Quantum Rabi and Dicke Models in Superconducting Circuits*, Sci. Rep. **4**, 7482 (2014).

3. Y. Salathé, M. Mondal, M. Oppliger, J. Heinsoo, P. Kurpiers, A. Potočnik, A. Mezzacapo, U. Las Heras, L. Lamata, E. Solano, S. Filipp, and A. Wallraff, *Digital Quantum Simulation of Spin Models with Circuit Quantum Electrodynamics*, Phys. Rev. X **5**, 021027 (2015).

4. U. Las Heras, L. García-Álvarez, A. Mezzacapo, E. Solano, and L. Lamata, *Quantum Simulation of Spin Chains Coupled to Bosonic Modes with Superconducting Circuits*, Chapter in R. S. Anderssen et al. (eds.), Mathematics for Industry 11, (Springer Japan, 2015) **ISBN**: 978-4-431-55341-0.

5. R. Barends, A. Shabani, L. Lamata, J. Kelly, A. Mezzacapo, U. Las Heras, R. Babbush, A. G. Fowler, B. Campbell, Yu Chen, Z. Chen, B. Chiaro, A. Dunsworth, E. Jeffrey, E. Lucero, A. Megrant, J. Y. Mutus, M. Neeley, C. Neill, P. J. J. O'Malley, C. Quintana, P. Roushan, D. Sank, A. Vainsencher, J. Wenner, T. C. White, E. Solano, H. Neven, J. M. Martinis, *Digitized Adiabatic Quantum Computing with a Superconducting Circuit*, Nature **534**, 222 (2016).

6. U. Las Heras, U. Alvarez-Rodriguez, E. Solano, M. Sanz, *Genetic Algorithms for Digital Quantum Simulations*, Phys. Rev. Lett. **116**, 230504 (2016).

II) Other articles produced during the Thesis period and not included

Published Articles

7. U. Las Heras, L. García-Álvarez, A. Mezzacapo, E. Solano, and L. Lamata, *Fermionic Models with Superconducting Circuits*, EPJ Quantum Technology **2**, 8 (2015).

8. L. García-Álvarez, U. Las Heras, A. Mezzacapo, M. Sanz, E. Solano, and L. Lamata, *Quantum Chemistry and Charge Transport in Biomolecules with Superconducting Circuits*, Sci. Rep. **6**, 27836 (2016).

9. K. G. Fedorov, L. Zhong, S. Pogorzalek, P. Eder, M. Fischer, J. Goetz, E. Xie, F. Wulschner, K. Inomata, T. Yamamoto, Y. Nakamura, R. Di Candia, U. Las Heras, M. Sanz, E. Solano, E. P. Menzel, F. Deppe, A. Marx, and R. Gross, *Displacement of Propagating Squeezed Microwave States*, Phys. Rev. Lett. **117**, 020502 (2016).

10. M. Sanz, U. Las Heras, J. J. Garcia-Ripoll, E. Solano, and R. Di Candia, *Quantum Estimation Methods for Quantum Illumination*, Phys. Rev. Lett. **118**, 070803 (2016).

Submitted Articles

11. U. Las Heras, R. Di Candia, K. G. Fedorov, F. Deppe, M. Sanz, and E. Solano, *Quantum Illumination Unveils Cloaking*, arXiv:1611.10280 (2016).

12. K. G. Fedorov, S. Pogorzalek, U. Las Heras, M. Sanz, P. Yard, P. Eder, M. Fischer, J. Goetz, E. Xie, K. Inomata, Y. Nakamura, R. Di Candia, E. Solano, A. Marx, F. Deppe, and R. Gross, *Finite-Time Quantum Correlations of Propagating Squeezed Microwaves*, arXiv:1703.05138 (2017).

Chapter 1

Introduction

The only joy in the world is to begin. It is good to be alive because living is beginning, always, every moment. When this sensation is lacking – as when one is in prison, or ill, or stupid, or when living has become a habit – one might as well be dead.

Cesare Pavese

1.1 Quantum Simulations

For many years, several problems have been known to be too complex for solving them via classical computers, which codify information in classical bits. Material science, high-energy physics, and quantum chemistry among others, provide problems considered as intractable, meaning that classical computers cannot implement the required algorithms due to the lack of scalability with respect to the size of the resources. In 1982, Richard Feynman conjectured that quantum computers, exploiting quantum properties, made of quantum bits and capable of implementing quantum operations, might allow us to perform information processing tasks which are unreachable for classical computers [1]. For this purpose, one should make use

of a controllable quantum system to be able to make predictions about a complex problem. In particular, in quantum mechanics, the dimension of the Hilbert space increases exponentially with the number of particles so it is necessary to consider other methods to compute the dynamics of quantum systems. Indeed, the main idea of a quantum simulator is to reproduce the behavior of a physical model and measure its physical properties.

The concept of a quantum simulator can be generalized to the universal quantum computer, made of quantum bits (qubits) and capable of implementing quantum operations [2]. This, in contrast to a single purpose machine, could solve a large variety of problems, including the simulation of multipartite quantum systems. Actually, computing the dynamics of systems made of only 40 qubits is a task that cannot be accomplished even by the most powerful classical supercomputers, providing one example of the superiority of quantum computers over the classical ones. Furthermore, quantum algorithms for quantum computing have been already proposed, e.g. the Shor [3] and Grover [4] algorithms for factorizing and searching, respectively, whose complexity grows with polynomial and linear number of resources. This is in contrast to classical computing, where the best known algorithms require an exponential and quadratic number of resources, respectively. Unfortunately, universal quantum computers are unfeasible at the moment due to the fact that current technology does not allow for systems with more than a dozen fully controllable qubits.

Fortunately, although only a few type of quantum operations can be implemented in current quantum platforms, it is possible to reproduce dynamics of interesting physical models and extract information about mimicked systems [5]. In this scenario, the controllable system employed in the lab is called a quantum simulator, and the quantum system whose properties we want to reproduce is the simulated model. In order to realize a quantum simulation, a set of criteria, weaker than that for quantum computing, and currently feasible, must be satisfied.

- **Quantum system**: A quantum simulator should contain quantum systems, e.g., spins, bosons, or fermions confined in a region of space. The system must have many degrees of freedom.

- **Initialization**: The first step to control a quantum system is the preparation of the system in a certain initial state at $t = 0$. This can be either a pure or a mixed state.

- **Hamiltonian engineering**: One should be able to control the system by making use of a set of interactions with external fields or between the particles of the system. Turning on and off these interactions, it should be possible to generate the dynamics of another quantum system.

- **Detection**: It should be feasible to perform individual and/or collective measurements on the system. Once the evolution has finished, this is required to determine the state of the system, or the result of the measurement of an observable over the system.

- **Verification**: It is crucial to know whether the non-trivial predictions of the simulation are correct. In case a classical machine could not reproduce the dynamics of the simulated system, one should work with consistency arguments to be confident about the correctness of the simulation. For example, it is expected that the dynamics of two different quantum systems should be the same if the Hilbert spaces and their interactions are similar. Accordingly, two different quantum platforms should reproduce the same results when simulating the same model.

Once a quantum platform fulfills the previous points, it can be classified as belonging to one of two classes of quantum simulators, either analog or digital quantum simulator. In the following, the main properties of both classes are reviewed.

1.1.1 Analog Quantum Simulators

The main feature of this type of quantum simulator is a similarity between the naturally occuring interactions within the quantum simulator, and the model to be simulated. Usually, the quantum platform employed in the lab has a few parameters that one can tune, so that the Hamiltonian governing the dynamics can be exactly the same as the one of the system to be simulated. In this way, by establishing a mapping between the quantum states of the simulated model and the physical

quantum simuator, it is possible to implement the desired dynamics. The mapping may be simple, like a small variation in the natural dynamics, or complex, like when the particle is forced to mimic another one. For instance, a bosonic field mapped onto another bosonic field is a simple mapping, but a spin could also be mapped onto an anharmonic oscillator. Furthermore, there are mappings between particles whose properties are completely different such as Jordan-Wigner [6] and Bravyi-Kitaev [7] transformations, in which fermions can be mapped onto spins.

Usually, analog quantum simulators are large systems which do not provide many degrees of freedom [8–12]. Even analog quantum simulations are restricted to a few simulatable models, and the execution is generally a relatively easy process. Once the system is initialized in a state, the preparation of which might be the hardest part of the whole process, one only needs to let it evolve and then make the corresponding measurements. In fact, due to the continuous evolution of the natural Hamiltonian of the system, analog quantum simulations are most suitable for tackling ground state searching problems, and for obtaining phase diagrams. Accordingly, quenching experiments, in which a system of a fixed static properties is suddenly evolved with respect to a new Hamiltonian, can be straightforwardly implemented. Moreover, it is possible to measure interesting quantities including response functions, coherence times and thermalization. These kind of quantum simulations, involving not only two-level systems but also bosonic modes, are on the edge of classical computer capabilities.

Many advances in the field of quantum error correction have been developed in the last few years [13–18], but extensions to analog quantum simulators is still an open question. Often, in the field of quantum computing, quantum circuits are expressed in terms of single and two-qubit gates, whose errors are known to be correctable if one introduces redundancy by using a multi-qubit encoding for a single logical qubit. However, analog quantum simulators often involve dynamics of many qubits and bosonic fields at the same time, impeding the stepwise evaluation, and hence, making the certification of the output a tough task for classical computers.

1.1.2 Digital Quantum Simulators

As defined in the previous subsection, analog quantum simulators need to have a Hamiltonian which can be mapped to the Hamiltonian of the model to be simulated. However, if we consider a given quantum architecture, there are a variety of interactions that can be reproduced, including single, two and multi-qubit gates. In digital quantum simulations, gates of different types are implemented one by one in a way that ensures that the resulting quantum state is similar to the one produced by the unitary evolution of the simulated model, even if the latter has nothing to do with the interactions actually implemented. In the method proposed by Lloyd [19], the following condition must be fulfilled,

$$H = \sum_{k=1}^{N} H_k, \tag{1.1}$$

where H is the Hamiltonian of the simulated model and H_k are the interactions executed by the system, which may act in different Hilbert spaces. Hence, complex Hamiltonians could be in principle decomposed into k single and two-qubit gates. Once H is written in terms of the available interactions of the employed quantum technology, its dynamics can be implemented using the Trotter expansion or equivalent methods [20, 21]. Most of physical models can be written as a polynomial sum of interactions, which makes Lloyd's method efficient. Indeed, an arbitrary unitary gate would require a number of single and two-qubit gates growing exponentially with the number of qubits and, therefore, it would be inefficient even for a quantum computer.

The method that Lloyd envisioned to digitally simulate Hamiltonians of type Eq. (1.1) is the Trotter expansion [2, 19], which can be expressed as follows,

$$e^{-iHt} = \lim_{l\to\infty} (e^{-iH_1 t/l} e^{-iH_2 t/l} \cdots e^{-iH_N t/l})^l. \tag{1.2}$$

In order to approximate the unitary evolution of the simulated model e^{-iHt} to an arbitrary precision, one must divide the evolution time into l time intervals of length t/l. Then, the system must evolve sequentially according to the N decomposed interactions H_k during the time intervals of length t/l. Finally, the sequence of

interactions should be repeated l times. The error can be reduced as much as desired just by increasing the number of Trotter steps l. It is important to remark that the simulated time is just t, but the simulation time it takes to experimentally do it is $N \cdot t$, since each of the N interaction that compose the simulated Hamiltonian H_k must be executed during a time t. This feature, besides switching times and other processes, has to be taken into account especially in those systems with short relaxation and coherence times.

The Trotter expansion is no other than the lowest order approximation of the Baker-Campbell-Hausdorff formula applied to a sum of operators. Considering a Hamiltonian H decomposed into two different interactions $H = H_1 + H_2$ and applying a single Trotter step, it reads

$$e^{-i(H_1+H_2)\Delta t} = e^{-iH_1\Delta t}e^{-iH_2\Delta t} + O((\Delta t)^2). \tag{1.3}$$

Hence, by decreasing $\Delta t = t/l$, that is performing more Trotter steps l, the error is reduced quadratically. One can also execute more complex expansions whose errors decrease faster with l, just by introducing more gates per Trotter step. The second-order approximation, also known as symmetric Trotter expansion [2], reads

$$e^{-i(H_1+H_2)\Delta t} = e^{-iH_1\Delta t/2}e^{-iH_2\Delta t}e^{-iH_1\Delta t/2} + O((\Delta t)^3), \tag{1.4}$$

where the error decreases cubically with l.

Restricted to the case of quadratic error and considering a set of interactions $\{H_1, ..., H_N\}$ and l Trotter steps, the Lie-Suzuki-Trotter formula estimates the error of the protocol [22],

$$e^{-iHt} = (e^{-iH_1t/l}e^{-iH_2t/l}\cdots e^{-iH_Nt/l})^l + \sum_{i>j}[H_i, H_j]t^2/2l + \sum_{k=3}^{\infty} E(k), \tag{1.5}$$

where the high-order error terms $E(k)$ are bounded by

$$||E(k)||_{\text{sup}} \leq l||Ht/l||^k_{\text{sup}}/k! \tag{1.6}$$

Here, $||A||_{\text{sup}}$ is defined as the supremum, or the maximum expectation value, of the operator A over the states that play a role in the simulation. Hence, the total error in

approximating $e^{-iHt} = (e^{-iH_1 t/l} \cdots e^{-iH_N t/l})^l$ is less than $||l(e^{iHt/l} - 1 - iHt/l)||_{\text{sup}}$, and can be made as small as desired by taking l large enough.

In digital quantum simulators, it is necessary to make an estimation of the experimental errors of the applied gates. In fact, when one increases the number of Trotter steps in order to decrease the Trotter error according to Eq. (1.5), the number of performed gates increases as $l \cdot N$. Considering that each gate introduces a certain experimental error, a compromise between experimental and Trotter errors must be considered in order to maximize the fidelity of the simulation. Indeed, experiments implementing digital methods show that the total error in a digital quantum simulation accumulates linearly [23–26]. Hence, improvements in gate fidelities generate a linear gain on the total simulation fidelity, allowing us to avoid the error accumulation which occurs when making use of error-corrected gates.

1.1.2.1 Digital-Analog Quantum Simulators

In the last few years, digital quantum simulators have been split into two different groups, the purely digital and the digital-analog ones. Both simulators follow the Trotter expansion in order to simulate a model, but while purely digital ones execute single and two-qubit gates, digital-analog quantum simulators introduce many-body gates or involve bosonic fields. Hence, it can be said that analog interaction blocks are introduced in a stepwise fashion in these simulations are, then, often combined with simpler gates like single-qubit rotations [27–29].

Regarding quantum error correction, in those digital quantum simulations in which interactions are just single and two-qubit gates, it is possible to implement mechanisms to correct bit and phase flips. However, in digital-analog quantum simulations, it is often not possible for the same reason as in purely analog quantum simulations.

Summarizing, digital-analog quantum simulators allow us to implement complex dynamics by exploiting the many-body and bosonic interactions that appear naturally in the considered quantum plarform. However, the extension of error correction protocols to analog blocks is still an open question.

1.2 Superconducting Circuits

Up to date, many quantum platforms have been used for quantum information protocols, such as trapped ions, cold atoms, quantum dots, cavity quantum electrodynamics (QED) and superconducting circuits. The latter has probably been the quantum architecture which has advanced the most in the last decade [30]. Indeed, protocols such as Grover algorithm [31], quantum teleportation [32], quantum simulations including ultra-strong [29, 33, 34] and deep-strong coupling [35, 36] interactions have been achieved, among others.

Circuit QED was proposed [37] and experimentally realized [38, 39] in 2004. Light-matter interactions traditionally studied in cavity QED systems, where an atom is coupled with the photons within a cavity, were quickly reproduced within this revolutionary architecture. In circuit QED setups a superconducting circuit plays the role of an atom, often considered as a two-level system, and a transmission line resonator acts as a cavity, with photons in the microwave regime instead of the optical. These macroscopic devices work at temperatures below 20 mK, where materials like aluminum are in the superconducting phase.

Superconducting circuits, also known as superconducting or artificial atoms, are made of inductances, capacitances and Josephson junctions. The latter is a nonlinear element that generates an anharmonicity in the energy levels, allowing us to restrict the system to the ground and first excited state, which is also known as superconducting qubit. Originally, three type of superconducting circuits were created, each exploiting their respective degrees of freedom: charge [40, 41], flux [42] or phase qubits [43]. Since then, many other qubits have appeared with architectures similar to the first three, including quantronium [44], transmon [45], fluxonium [46], as well as further hybrid designs [47] that reduce their sensitivity to decoherence hence improving their controllability. To be concrete, transmon qubits are charge-like qubits which, by increasing the shunt capacitance, have a more flattened charge dispersion relation. As a result, these devices are much less sensitive to decoherence produced by charge fluctuations. Given the extended use of this kind of qubits in experimental labs, the proposals included in this Thesis are made for transmon qubits.

Transmission line resonators are a crucial element in superconducting circuits. Indeed, they not only play the role of a harmonic oscillator which couples to the to superconducting qubits, but they also provide for many applications, such as non-demolition measurements [48] and the execution of single qubit rotations, achieved through the use of microwave drivings [37, 39]. Moreover, several qubits can be placed within a single resonator with a dispersive coupling, allowing one to implement many-body interactions without requiring local or capacitive couplings between the qubits. Furthermore, recent architectures provide a high tunability, which gives us the chance to perform quantum operations only directly onto the considered qubits.

Standard systems composed of transmon qubits and transmission line resonators usually have coherence times of tens of microseconds, while single-qubit and two-qubit gates require a few nanoseconds and a few tens of nanoseconds respectively [17]. Therefore, in these kind of circuit QED systems, up to one thousand gates can be implemented within the coherence time. In fact, even this number has recently been surpassed in a recent experimental realization of a digital quantum simulation [26]. In addition, quantum memories have been proposed for superconducting setups with the goal of preserving quantum information, while quantum error correction codes have been implemented by several groups [17, 18] involving up to seven qubits.

In summary, superconducting circuits are a promising quantum platform to implement complex quantum protocols due to their high controllability. In particular, over the last few years they have developed extremely rapidly, and are now the most arguably advanced platform for the realization of scalable quantum processing devices.

1.3 Spin Models

The microscopic description of magnetism is one of the most pertinent questions in the field of condensed matter. Indeed, spin models are mathematical models that describe physical interactions between magnetic dipole moments of particles in ordinary materials. In the early 20th century, classical spin models based on dipole-dipole interactions, such as the Heisenberg interaction, were studied in both the ferromagnetic and antiferromagnetic regimes with external magnetic fields, and key

features of phase transitions were discovered. Moreover, spin lattices in 2D and 3D were studied, exhibiting exotic properties like frustration.

Later on, spin systems started being treated quantum mechanically. While classical spin interactions are modeled with scalar products of spin vectors, inner products of Pauli matrices are employed for the description of quantum spin interactions. This research line has provided applications in a variety of fields including quantum phase transitions [49, 50], strongly correlated systems [51], quantum information theory and quantum computing [2], among others.

Besides spin-spin interactions, spins coupled to bosons have also been considered in which light-matter interactions are studied within the framework of quantum field theory. In quantum optics, light is described with a continuum of bosonic fields, while the description of matter is written in terms of anharmonic oscillators with only a few populated levels. In this context, spin-boson Hamiltonians involving both single and several spins have been proposed, including semiclassical Rabi [52], Jaynes-Cummings [53], Dicke [54] and Tavis-Cummings [55] Hamiltonians, quantum Rabi model [56] and spin-boson model [57]

Advances in several quantum platforms have allowed us to perform spin and spin-boson interactions in the laboratory. Indeed, in cavity QED, one can demonstrate such interactions, since the light within the cavity is quantized and this bosonic mode is coupled to a few internal states of the atom. However, the same physics can be produced in several quantum platforms. For instance, in circuit QED, superconducting qubits and transmission line resonators substitute atoms and cavities respectively, while in trapped ions, instead of electromagnetic fields, motional degrees of freedom are employed as quantized bosonic modes. In this way, many proposals and experiments have been realized in the last years for the study of spin models, involving relevant features from spin-spin correlations to quantum phase diagrams [11, 58–61].

1.4 Genetic Algorithms

In computer science, there exist many algorithms that look for solutions to optimization problems. Genetic algorithms [62] belong to the branch of evolutionary

algorithms in the field of machine learning. Inspired by biological systems, these type of algorithms simulate the natural selection of individual, in which the solutions to optimization problems have been encoded. Letting the system evolve, the most adapted individuals to the condition defined by the optimization problem survive, achieving good results in much less time that conventional optimization algorithms.

Most genetic algorithms work via the following steps. First, the genetic code of the individuals and the fitness function are defined according to the optimization problem, in such a way that the genetic code of individuals saves the information of candidate solutions. Then, two kind of operations are executed: mutation and crossover. The first introduces modifications in the properties of each individual while the crossover exchanges information of two or more individuals. Hence, a new generation of individuals is created, which is finally evaluated according to the fitness function. In the case that one set of individuals from a given generation is more highly adapted, these are the ones that will be saved in order to repeat the cycle, otherwise one simply keeps the last generation. By choosing a high enough number of repetitions, or introducing a convergence condition to be satisfied, a set of improved solutions to the optimization problem is obtained.

As a result of the manner in which genetic algorithms are constructed, several solutions are obtained relatively fast, in comparison with generic optimization algorithms, which need to evaluate every possible solution to obtain the optimal one. On the other hand, genetic algorithms produce a set of solutions which might not be the optimal but are robust against small variations. This means that the genetic code of the best individual can be modified slightly without affecting the convergence of the solution, which makes genetic algorithms a flexible optimization method. For the same reason, the solutions are robust against errors. For instance, designing an electric circuit for a concrete purpose might be an easy task to perform manually. At the same time, if one of the components of the circuit breaks the circuit will probably not work. However, genetic algorithms provide more complex solutions in which these unexpected problems do not affect the system as much as in simple and optimal solutions.

These kind of machine learning protocols have been used for solving optimization problems with many applications, such as mirrors that funnel sunlight into

a solar collector [63], antennas measuring the magnetosphere of Earth from satellites [64], walking methods for computer figures [65] and efficient electrical circuit topology [66, 67], among others. Moreover, the implementation of classical genetic-algorithm-based protocols in quantum information has already begun for tasks like characterizing linear optical networks [68] and finding unitary transformations for quantum computations [69]. These previous results illustrate the potential of genetic algorithms within the quantum context.

1.5 Contents of this Thesis

We propose a variety of digital quantum simulations of spin models with superconducting circuits. For this purpose, we consider some of the newest experimental setups involving transmission line resonators and transmon qubits, to simulate bosonic fields and spins respectively. By employing the Suzuki-Lie-Trotter formula and combining the natural interactions from circuit QED architectures, we detail the steps necessary to reproduce the behavior of several spin models. Furthermore, we analyze experimental and digital errors in the process. The field of digital quantum simulations in superconducting circuits has only recently begun. However, thanks to rapid advances in superconducting technologies, this platform competes with alternative technologies such as trapped ions. Accordingly, we think that this work is timely and provides the first proposals in this field. In addition, we review key experimental articles in which we are coauthors, reproducing our theoretical proposals.

This Thesis is composed of four chapters with the following contents:

In Chapter 2, we propose the implementation of a digital quantum simulator for prototypical spin models in a circuit QED architecture. We consider the feasibility of the quantum simulation of Heisenberg and frustrated Ising models in transmon qubits coupled to coplanar waveguide microwave resonators, by using the exchange gate and single qubit rotations. We study the time evolution of these models and compare the ideal spin dynamics with a realistic version of the proposed quantum simulator. Furthermore, we analyze the experimental results produced with a superconducting chip in the lab of Prof. Andreas Wallraff at ETH Zurich, where dynamics of XY Heisenberg and Ising models are digitally implemented. Finally, we discuss the key

steps for developing a toolbox of digital quantum simulators in superconducting circuits.

We propose, in Chapter 3, the digital-analog quantum simulation of the quantum Rabi and Dicke models using circuit QED. We find that all physical regimes, in particular those which are impossible to realize in typical cavity QED setups, can be simulated via unitary decomposition into digital steps. Moreover, when the bosonic-mode frequency vanishes, we show the emergence of Dirac equation dynamics from the quantum Rabi model when the mode frequency vanishes. We analyze the feasibility of this proposal with realistic superconducting technology. To finish, we briefly review the recent experiment by the group of Prof. Leonardo DiCarlo at Delft University of Technology.

In Chapter 4, we consider the implementation of digitized adiabatic quantum simulation of spin chains with superconducting circuits. First, we study the implementation of digital quantum simulations of spins coupled to bosonic field modes. Gates with high fidelities allow one to simulate a variety of Ising magnetic pairing interactions with a transverse field, Tavis-Cummings interactions between spins and a bosonic mode, and a spin model with three-body terms. We analyze the feasibility of the implementation in realistic circuit QED setups, where the interactions are either realized via capacitive couplings or mediated by microwave resonators. Additionally, we propose a digitized adiabatic quantum computing protocol which combines the generality of the adiabatic algorithm with the universality of the digital approach. This protocol is implemented in an experiment performed by the group of John M. Martinis at Google/University of California, Santa Barbara, using a superconducting circuit with nine qubits. We probe the adiabatic evolutions, and quantify the success of the algorithm for random spin problems. We find that the superconducting chip can approximate the solutions to both frustrated Ising problems and problems with more complex interactions, with a performance that is comparable.

Finally, in Chapter 5, we propose genetic algorithms, which are robust optimization techniques inspired by natural selection, to enhance the versatility of digital quantum simulations. In this sense, we show that genetic algorithms can be employed to increase the fidelity and optimize the resource requirements of digital

quantum simulation protocols, while adapting naturally to the experimental constraints. Furthermore, this method allows us to reduce not only digital errors, but also experimental errors in quantum gates. Indeed, by adding ancillary qubits, we design a modular gate made out of imperfect gates, whose fidelity is larger than the fidelity of any of the constituent gates. Finally, we prove that the proposed modular gates are resilient against different gate errors.

To conclude, the overall conclusions of this Thesis are detailed in the last Chapter, where we also discuss the future of the field of digital quantum simulations with superconducting circuits.

Chapter 2

Digital Quantum Simulation of Spin Systems

Divide et impera.

Julius Caesar

2.1 Introduction

The quantum coherent control of superconducting qubits has dramatically improved during the last years [30]. Indeed, circuit quantum electrodynamics (cQED) [39] is considered as a potential scalable platform for quantum computing. Basic quantum algorithms [70] and tests of fundamentals in quantum mechanics [71] have already been realized. Additionally, single and two-qubit gates [72], preparation of complex entangled states [73], and basic protocols for quantum error correction [74] are some of the quantum information tasks achievable with high fidelities. Consequently, superconducting circuits have reached sufficient complexity and potential scalability to be considered as quantum simulators.

A quantum simulator is a technology that allows us to reproduce the behavior of another quantum system. The original idea of quantum simulation can be traced back to Feynman [1], while the first mathematical formulation using local interactions was proposed by Lloyd some years later [19]. So far, several analog quantum simulations in circuit QED have been proposed [60, 61, 75–80]. On the other hand, an experiment of discrete-time gate sequences to reproduce the dynamics of a given spin Hamiltonian has been recently realized in ion-trap [23] and photonic [81] systems, together with proposals for the emulation of interacting fermionic-bosonic models [82, 83]. The digital decomposition of Hamiltonians and their implementation using short-time gates has been demonstrated to be efficient [21, 84]. Accordingly, it is timely to address the topic of digital quantum simulators with superconducting circuits. The quantum simulation of spin models can shed light onto a variety of open problems, such as quantum phase transitions [85], correlated one-dimensional systems [86], and high-T_c superconductivity [87].

In this Chapter, we investigate the implementation of digital quantum simulations of spin Hamiltonians in a superconducting setup consisting of several superconducting qubits coupled to a coplanar waveguide resonator. Although our proposal is valid for every superconductor-based qubit with a sufficiently long coherence time, we focus on a transmon qubit setup. Superconducting transmon qubits are commonly used because of their low sensitivity to offset charge fluctuations [45]. However, depending on the targeted physical properties, other superconducting qubits may be considered. First, we show that a variety of spin dynamics can be retrieved by a digital decomposition in a generic quantum simulator. Then, we consider prototypical spin models, simulation times, and fidelities with current circuit QED technology, showing the computational power of superconducting qubits in terms of digital quantum simulations. In this way, we analyze the required resources in a realistic setup for a multipurpose quantum simulator of spin dynamics capable of emulating a general multiqubit spin Hamiltonian. Finally, we analyze the experimental results obtained in the lab of Prof. Andreas Wallraff at ETH Zurich.

2.2 Heisenberg Model

Most physical Hamiltonians can be written as a sum of local terms, $H = \sum_{k=1}^{N} H_k$, where each H_k acts on a local Hilbert space. The dynamics of a generic Hamiltonian H can be approximated by discrete stepwise unitaries, up to arbitrary small errors, according to the formula ($\hbar = 1$ here and in the following) [19],

$$e^{-iHt} = \left(e^{-iH_1 t/l} \cdots e^{-iH_N t/l}\right)^l + \sum_{i<j} \frac{[H_i, H_j]t^2}{2l} + \sum_{k=3}^{\infty} E(k), \tag{2.1}$$

with $l||Ht/l||_{\text{sup}}^k/k! \geq ||E(k)||_{\text{sup}}$ being an upper bound on the higher order error terms. In the trivial case, when $[H_i, H_j] = 0$ for every $\{i, j\}$, the error made in the digital approximation is zero. To approximate e^{-iHt} to arbitrary precision, one can divide the simulated time t into l intervals of size t/l, and apply sequentially the evolution operator of each local term for every interval. Repeating the sequence l times, the error can be made as small as desired just by increasing l. However, in a realistic quantum simulator, there will be a limit to the number of local $e^{-iH_k t/l}$ gates feasible to apply, due to accumulated gate errors. Accordingly, one has to optimize the number of steps l to get the best possible result.

Digital methods can be used to simulate the Heisenberg spin model with available resources in superconducting circuits. We consider a setup made of several transmon qubits coupled to a single coplanar microwave resonator [45],

$$\begin{aligned} H^T = \quad & \omega_r a^\dagger a + \sum_{i=1}^{N} \Big[4E_{C,i}(n_i - n_{g,i})^2 - E_{J,i}\cos\phi_i \\ & + 2\beta_i e V_{\text{rms}} n_i (a + a^\dagger)\Big]. \end{aligned} \tag{2.2}$$

Here, n_i, $n_{g,i}$ and ϕ_i stand respectively for the quantized charge on the superconducting island, the offset charge and the quantized flux of the i-th transmon qubit. The operators $a(a^\dagger)$ act on the resonator field, whose first mode has frequency ω_r. $E_{C,i}$ is the charging energy of the superconducting island, while $E_{J,i} = E_{J,i}^{\max}|\cos(\pi\Phi_i/\Phi_0)|$ is the Josephson energy of the dc-SQUID loop embedded in the i-th qubit. The latter can be tuned from small values up to $E_{J,i}^{\max}$ by changing the ratio between the external magnetic flux Φ_i, that threads the loop, and the elementary flux quantum

Φ_0. Here, β_i are renormalization coefficients of the couplings due to circuit capacitances, $V_{\rm rms}$ is the root mean square voltage of the resonator, and e is the electron charge. Typical transmon regimes consider ratios of Josephson to charging energy $E_J/E_C \gtrsim 20$.

Notice that cavity and circuit QED platforms do not feature the Heisenberg interaction from first principles. Nevertheless, one can consider a digital simulation of the model. We show that the coupled transmon-resonator system, governed by the Hamiltonian in Eq. (2.2), can simulate Heisenberg interactions of N qubits, which in the case of homogeneous couplings reads

$$H^{\rm H} = \sum_{i=1}^{N-1} J\left(\sigma_i^x\sigma_{i+1}^x + \sigma_i^y\sigma_{i+1}^y + \sigma_i^z\sigma_{i+1}^z\right). \tag{2.3}$$

Here, the Pauli matrices σ_i^j, $j \in \{x, y, z\}$ refer to the subspace spanned by the first two levels of the i-th transmon qubit. We begin by considering the simplest case, in which two qubits are involved. The XY exchange interaction can be directly reproduced by dispersively coupling two transmon qubits to the same resonator [37, 88, 89], $H_{12}^{xy} = J\left(\sigma_1^+\sigma_2^- + \sigma_1^-\sigma_2^+\right) = J/2\left(\sigma_1^x\sigma_2^x + \sigma_1^y\sigma_2^y\right)$. The XY exchange interaction can be transformed via local rotations of the single qubits to get the effective Hamiltonians $H_{12}^{xz} = R_{12}^x(\pi/4)H_{12}^{xy}R_{12}^{x\dagger}(\pi/4) = J/2\left(\sigma_1^x\sigma_2^x + \sigma_1^z\sigma_2^z\right)$ and $H_{12}^{yz} = R_{12}^y(\pi/4)H_{12}^{xy}R_{12}^{y\dagger}(\pi/4) = J/2\left(\sigma_1^y\sigma_2^y + \sigma_1^z\sigma_2^z\right)$. Here, $R_{12}^{x(y)}(\pi/4) = \exp[-i\pi/4(\sigma_1^{x(y)} + \sigma_2^{x(y)})]$ represents a local rotation of the first and second transmon qubits along the $x(y)$ axis. The XYZ exchange Hamiltonian H_{12}^{xyz} can therefore be implemented according to the protocol shown in Fig. 2.1a with the following steps. *Step 1.*– The qubits interact for a time t according to the XY Hamiltonian H_{12}^{xy}. *Step 2.*– Application of single qubit rotations $R_{12}^x(\pi/4)$ to both qubits. *Step 3.*– The qubits interact for a time t with H_{12}^{xy} Hamiltonian. *Step 4.*– Application of single qubit rotation $R_{12}^{x\dagger}(\pi/4)$ to both qubits. *Step 5.*– Application of single qubit rotation $R_{12}^y(\pi/4)$ to both qubits. *Step 6.*– The qubits interact for a time t according to the H_{12}^{xy} Hamiltonian. *Step 7.*– Application of single qubit rotation $R_{12}^{y\dagger}(\pi/4)$ to both qubits. Consequently, the total unitary evolution reads

$$U_{12}^{\rm H}(t) \;=\; e^{-iH_{12}^{xy}t}e^{-iH_{12}^{xz}t}e^{-iH_{12}^{yz}t} = e^{-iH_{12}^{\rm H}t}. \tag{2.4}$$

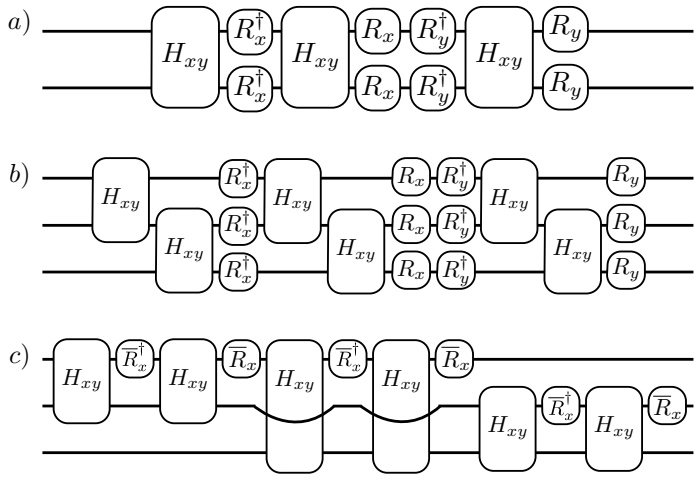

FIGURE 2.1: Protocols for digital quantum simulations with transmon qubits. a) Heisenberg model of two qubits. b) Heisenberg model of three qubits. c) Frustrated Ising model of three qubits. Here $R_{x(y)} \equiv R^{x(y)}(\pi/4)$ and $\overline{R}_x \equiv R^x(\pi/2)$.

This evolution operator simulates the dynamics of Eq. (2.3) for two qubits. Arbitrary inhomogeneites of the couplings can be achieved by implementing different simulated phases for different digital steps. Notice that, in this case, just one Trotter step is needed to achieve a simulation without digital errors, due to the commutativity of H_{12}^{xy}, H_{12}^{xz}, and H_{12}^{yz}. Thus, from a practical point of view, the only source of errors will come from accumulated gate errors. One can assume two-qubit gates with an error of about 5% and eight $\pi/4$ single qubit rotations with errors of 1%. This will give a total fidelity of the protocol around 77%. Moreover, the total execution time for a $\pi/4$ simulated XYZ phase will be of about 0.10 μs. Throughout the paper, we compute the execution times by summing the corresponding times of all the employed gates, where we consider typical circuit QED values.

Now, we consider a digital protocol for the simulation of the Heisenberg interaction for a chain of three spins. When considering more than two spins, one has to take into account noncommuting Hamiltonian steps, involving digital errors. This three-spin case is directly extendable to arbitrary numbers of spins. We follow a digital approach for its implementation, as shown in Fig. 2.1b. *Step 1.*– Qubits 1 and 2 interact for a time t/l with XY Hamiltonian. *Step 2.*– Qubits 2 and 3 interact for

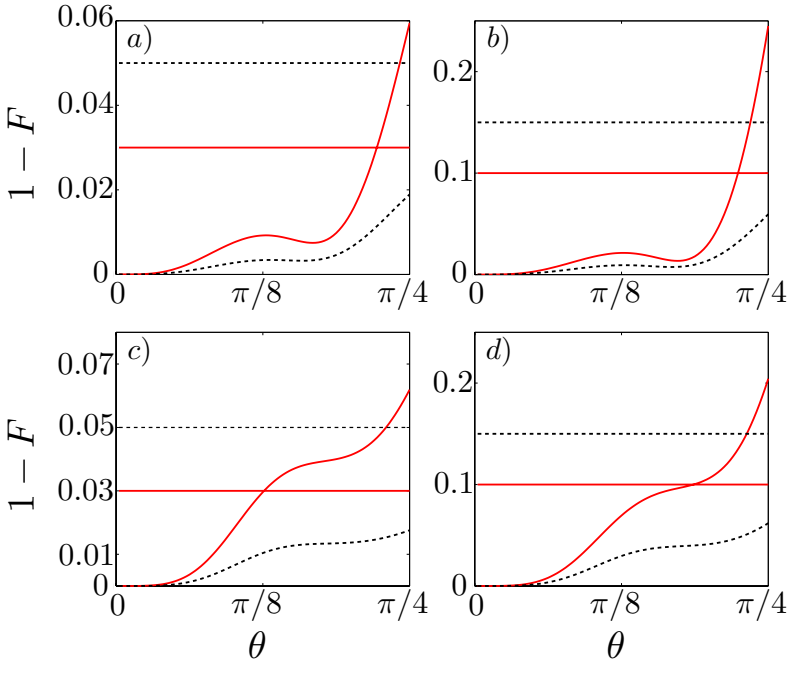

FIGURE 2.2: Fidelity loss for simulated Hamiltonians for three qubits, in the interval $\theta = [0, \pi/4]$, $\theta \equiv Jt$. Curved lines show digital errors, while horizontal lines show the accumulated error due to a single step error of ϵ. Red solid (black dotted) lines stand for higher (lower) digital approximations l. a) Heisenberg model, with $\epsilon = 10^{-2}$, $l = 3, 5$, and b) $\epsilon = 5 \times 10^{-2}$, $l = 2, 3$. c) Transverse field Ising model, with $\epsilon = 10^{-2}$, $l = 3, 5$ and d) $\epsilon = 5 \times 10^{-2}$, $l = 2, 3$.

a time t/l with XY Hamiltonian. *Step 3.*– Application of $R^{x}_{12}(\pi/4)$ to each qubit. *Step 4.*– Qubits 1 and 2 interact for a time t/l with XY Hamiltonian. *Step 5.*– Qubits 2 and 3 interact for a time t/l with XY Hamiltonian. *Step 6.*– Application of $R^{x\dagger}_{12}(\pi/4)$ to each qubit. *Step 7.*– Application of $R^{y}_{12}(\pi/4)$ to each qubit. *Step 8.*– Qubits 1 and 2 interact for a time t/l with XY Hamiltonian. *Step 9.*– Qubits 2 and 3 interact for a time t/l with XY Hamiltonian. *Step 10.*– Application of $R^{y\dagger}_{12}(\pi/4)$ to each qubit. Thus, the total unitary evolution per step reads

$$U^{\mathrm{H}}_{123}(t/l) = \quad e^{-iH^{xy}_{12}t/l}e^{-iH^{xy}_{23}t/l}e^{-iH^{xz}_{12}t/l}e^{-iH^{xz}_{23}t/l}e^{-iH^{yz}_{12}t/l}e^{-iH^{yz}_{23}t/l}. \qquad (2.5)$$

In this case, the protocol has to be repeated l times according to Eq. (2.1), to approximate the dynamics of Eq. (2.3) for three qubits. Each Trotter step involves

four single qubit gates at different times and six two qubit gates, producing a step-time of about 0.16 μs, which is well below standard coherence times for transmon qubits [90]. In Fig. 2.2a and 2b, we plot the digital error of the simulated Heisenberg model for three qubits, along with horizontal lines, that show the error of the imperfect gates multiplied by the number of Trotter steps, i.e., the total accumulated gate error. In this way, one can distinguish time domains dominated by the digital error and time domains in which the largest part of the error in the quantum simulation is due to experimental gate errors. One can consider interactions with open and closed boundary conditions, adding an extra term coupling the first and last spin. Extending this protocol to N qubits with open or periodic boundary conditions, we compute an upper bound on the second-order Trotter error $E_{\text{open}} = 24(N-2)(Jt)^2/l$ and $E_{\text{periodic}} = 24N(Jt)^2/l$.

2.3 Ising Model

Here, we consider a generic N qubit Ising interaction $J\sum_i \sigma_i^x\sigma_{i+1}^x$, with periodic boundary conditions. Considering a three site model is sufficient to show the effect of frustration in the system. The antiferromagnetic interaction is inefficiently solvable in a classical computer, while it is efficient for a quantum simulator [10]. We consider the isotropic antiferromagnetic case between three sites , $H_{123}^{\text{I}} = J\sum_{i<j}\sigma_i^x\sigma_j^x$, with $i,j = 1,2,3$ and $J > 0$. In order to simulate this Hamiltonian, one can apply a $\pi/2$ rotation to one of the qubits. This will result in an effective stepwise elimination of the YY component of interaction,

$$H_{12}^{x-y} = R_1^x(\pi/2)H_{12}^{xy}R_1^{x\dagger}(\pi/2) = J\left(\sigma_1^x\sigma_2^x - \sigma_1^y\sigma_2^y\right). \tag{2.6}$$

The protocol for the simulation is shown in Fig. 2.1c. As the terms of the Ising Hamiltonian commute, there is no error from the Trotter expansion. We obtain a fidelity of the protocol of about 64%. The time for the execution of all gates is 0.18 μs.

One can also add a transverse magnetic field, that leads to the Hamiltonian $H_{123}^{\text{IT}} = J\sum_{i<j}\sigma_i^x\sigma_j^x + B\sum_i\sigma_i^y$. In this case, the terms of the Hamiltonian do not commute, so we need to apply more than one Trotter step to achieve adequate

TABLE 2.1: Execution times and error bounds for the Heisenberg(H) and Ising(I) models with open(o) and periodic(p) boundary conditions for N qubits. Here $\theta \equiv Jt$, $J/2$ and g_ϕ are respectively the coupling strenght of the XY and single-qubit gates, and τ_s is the pulse time required for a single qubit rotation.

	Execution time	Error bound
H_o	$4l\tau_s + 6(N-1)\theta/J$	$24(N-2)(Jt)^2/l$
H_p	$4l\tau_s + 6N\theta/J$	$24N(Jt)^2/l$
I_o	$2(N-1)l\tau_s + \theta/g_\phi + 4(N-1)\theta/J$	$2(N-1)(Jt)^2/l$
I_p	$2Nl\tau_s + \theta/g_\phi + 4N\theta/J$	$2N(Jt)^2/l$

fidelities. The unitary evolution per Trotter step in this case is given by

$$\begin{aligned} U(t/l) = \quad & e^{-iH_{12}^{xy}t/l}e^{-iH_{12}^{x-y}t/l}e^{-iH_{13}^{xy}t/l}e^{-iH_{13}^{x-y}t/l} \\ & \times e^{-iH_{23}^{xy}t/l}e^{-iH_{23}^{x-y}t/l}e^{-iBt/l(\sigma_1^y+\sigma_2^y+\sigma_3^y)} \\ & = e^{-i2Jt/l(\sigma_1^x\sigma_2^x+\sigma_1^x\sigma_3^x+\sigma_2^x\sigma_3^x)}e^{-iBt/l(\sigma_1^y+\sigma_2^y+\sigma_3^y)}. \end{aligned} \tag{2.7}$$

In Fig. 2.2c and 2.2d, we plot the fidelity loss for different number of Trotter steps, in the 3-qubit frustrated Ising model with transverse magnetic field, considering an error for each step due to the imperfect gates. The time for simulating the transverse field Ising model for the considered dynamics is about 190 ns per Trotter step. The protocol can also be extended to N qubits with open and periodic boundary conditions, where we compute an upper bound to the second-order error in Jt/l of $E_{\text{open}} = 2(N-1)(Jt)^2/l$ and $E_{\text{periodic}} = 2N(Jt)^2/l$. We report in Table 2.1 execution times and error bounds for the models proposed, for N qubits. In general, given the nonlocal character of the microwave resonator acting as a quantum bus, one can emulate 2D and 3D interaction topologies.

2.4 Feasibility in Current Circuit QED Architectures

In order to estimate the feasibility of the protocols in a superconducting circuit setup, we perform a numerical simulation for the Heisenberg interaction between two transmon qubits coupled to a coplanar waveguide resonator. We compute the

effect on the protocol of a realistic XY interaction, given as an effective second-order Hamiltonian, obtained from the first order Hamiltonian

$$H_{\rm t} = \sum_{i=0}^{2}\sum_{j=1}^{2}\left(\omega_i^j |i,j\rangle\langle i,j|\right) + \omega_r a^\dagger a + \sum_{i=0}^{2}\sum_{j=1}^{2} g_{i,i+1}(|i,j\rangle\langle i+1,j| + \text{H.c.})(a+a^\dagger). \tag{2.8}$$

Here, ω_i^j is the transition energy of the i-th level, with respect to the ground state, of the j-th qubit, and ω_r is the transition frequency of the resonator. We consider the first three levels for each transmon qubit, and a relative anharmonicity factor of $\alpha_r = (\omega_2^j - 2\omega_1^j)/\omega_1^j = -0.1$, typical for the transmon regime [45]. We assume identical transmon devices, with transition frequencies $\omega_1^{1,2} \equiv \omega_1 = 2\pi \times 5$ GHz. The resonator frequency is set to $\omega_r = 2\pi \times 7.5$ GHz. We consider the coupling between different levels of a single transmon qubit [45] $g_{i,i+1} = \sqrt{i+1}g_0$, where $g_0 = 2\beta e V_{\rm rms} = 2\pi \times 200$ MHz. The chosen experimental parameters are typical for superconducting circuit setups and they can be optimized for each platform. The resonator-transmon coupling Hamiltonian, in the interaction picture with the free energy $\sum_{i,j}\omega_i^j|i,j\rangle\langle i,j| + \omega_r a^\dagger a$, results in an effective coupling between the first two levels of the two transmon qubits $H_{\rm eff} = [g_{01}^2\omega_1/(\omega_1^2 - \omega_r^2)] \times (\sigma_1^x\sigma_2^x + \sigma_1^y\sigma_2^y)$, where we have considered negligible cavity population $\langle a^\dagger a\rangle \approx 0$ and renormalization of the qubit frequencies to cancel Lamb shifts. Here we have defined a set of Pauli matrices for the subspace spanned by the first two levels of each transmon, e.g. $\sigma_{1(2)}^x \equiv |0,1(2)\rangle\langle 1,1(2)| + \text{H.c.}$ In order to estimate the effect of decoherence in a realistic setup, we consider the master equation dynamics,

$$\dot\rho = -i[H_{\rm t},\rho] + \kappa L(a)\rho + \sum_{i=1}^{2}\left(\Gamma_\phi L(\sigma_i^z)\rho + \Gamma_- L(\sigma_i^-)\rho\right), \tag{2.9}$$

where we have defined the Lindblad superoperators $L(\hat A)\rho = (2\hat A\rho\hat A^\dagger - \hat A^\dagger\hat A\rho - \rho\hat A^\dagger\hat A)/2$. We have set a decay rate of $\kappa = 2\pi \times 10$ kHz for the resonator, and a dephasing and decay rate of $\Gamma_\phi = \Gamma_- = 2\pi \times 20$ kHz for the single transmon qubit. We perform a numerical simulation for the Heisenberg protocol for two transmon qubits, following the steps as in Fig. 2.1a, using for the XY interaction steps the

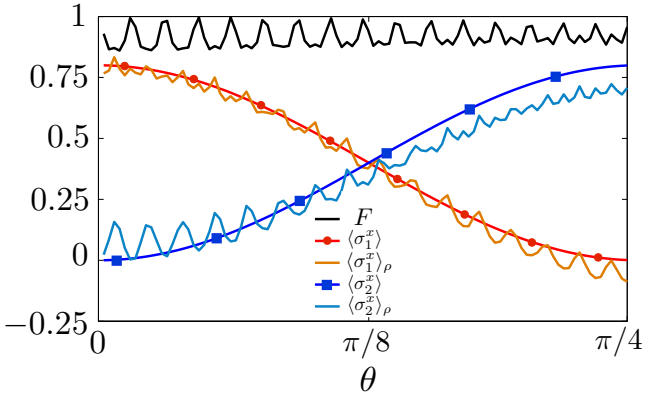

FIGURE 2.3: Dynamics for the simulated Heisenberg model for two transmon qubits, which are initialized in the state $1/\sqrt{5}(|\uparrow\rangle + 2|\downarrow\rangle) \otimes |\downarrow\rangle$. Fidelity $F = \mathrm{Tr}(\rho|\Psi_I\rangle\langle\Psi_I|)$ shows the behavior of the protocol for a given simulated phase θ. The ideal spin dynamics $\langle\sigma_i^x\rangle$ for both qubits is plotted versus mean values $\langle\sigma_i^x\rangle_\rho$ obtained with the qubit Hamiltonian H_t.

result of the dynamics obtained by solving Eq. (2.9), and ideal single-qubit rotations. The result is plotted in Fig. 2.3. The evolution for the density matrix ρ, that encodes the dynamics of the two transmon qubits, is compared to the exact quantum evolution $|\Psi\rangle_I$, that evolves according to the Hamiltonian in Eq. (2.3), with $J = g_{01}^2\omega_1/(\omega_1^2 - \omega_r^2) \approx 2\pi \times 6$ MHz. One can observe that good simulation fidelities $F = \mathrm{Tr}(\rho|\Psi_I\rangle\langle\Psi_I|)$ are achieved for nontrivial dynamics. Note that the action of the Heisenberg Hamiltonian on an initial state, which is also an eigenstate of the $\sigma_1^z\sigma_2^z$ operator, would be equivalent to the one of the XY exchange interaction. To show signatures of the Heisenberg interaction, we choose in our simulation an initial state which does not have this property. One can also notice the typical small time-scale fidelity oscillations due to the first order part of the dispersive exchange interaction. By further detuning the qubits from the resonator, one can reduce the contribution of the non-dispersive part of the interaction, and increase the global fidelity of the protocol.

2.5 Experimental Realization

In this section, we analyze the experimental results obtained in the lab of Prof. Andreas Wallraff from the ETH Zurich. The experiments are carried out with two superconducting transmon qubits [45] coupled dispersively to a common mode of a coplanar waveguide resonator, see Appendix A for the device layout and setup diagram. We operate the circuit at 30 mK in a dilution refrigerator. The qubits Q1 and Q2 interact with a coplanar waveguide resonator with a fundamental resonance frequency at 7.14 GHz which serves both as a quantum bus [88] and for readout [91].

The natural two-qubit interaction is the XY exchange coupling [88] $H^{xy}_{1,2} = \frac{J}{2}(\sigma^x_1\sigma^x_2+\sigma^y_1\sigma^y_2)$ mediated by virtual photons in a common cavity mode, which we also refer to as the XY interaction, where J is the effective qubit-qubit coupling strength [89]. The XY interaction is activated by tuning the transition frequency of qubit Q1 (5.44 GHz) into resonance with qubit Q2 (5.24 GHz) for a time τ using nanosecond time scale magnetic flux bias pulses [31], see Appendix A for further details. When the qubit transition frequencies are degenerate, the resonator-mediated coupling strength is spectroscopically determined to be $J = -40.4$ MHz. To make the presentation of the simulation results independent of the actual J, we express the interaction time τ for a given J in terms of the acquired quantum phase angle $2|J|\tau$. In our setup, the action of the XY gate (Fig. 2.4a) is characterized by full process tomography for a complete set of 16 initial two-qubit states and a series of 25 different interaction times τ finding process fidelities no lower than 89 %, see Appendix A.

In Fig. 2.5a and 2.5b, we present non-stationary spin dynamics under the XY exchange interaction for a characteristic initial two-qubit state $|\uparrow\rangle(|\uparrow\rangle+|\downarrow\rangle)/\sqrt{2}$ with spins pointing in perpendicular directions along $+\mathbf{z}$ and $+\mathbf{x}$, respectively. During the XY interaction, the state of one spin is gradually swapped to the other spin and vice versa with a phase angle of $\pi/2$. This corresponds to the iSWAP gate [92]. As a consequence, the measured Bloch vectors move along the YZ and XZ planes. For a quantum phase angle of $2|J|\tau = \pi$ they point along the $+\mathbf{y}$ and $+\mathbf{z}$ directions respectively in good agreement with the ideal unitary time evolution indicated by dashed lines in Fig. 2.5a,b. We also find that the two-qubit entanglement characterized by the measured negativity [93] of 0.246 is close to the maximum expected value of 0.25 for this initial state at a quantum phase angle of $\pi/2$. As a consequence the Bloch

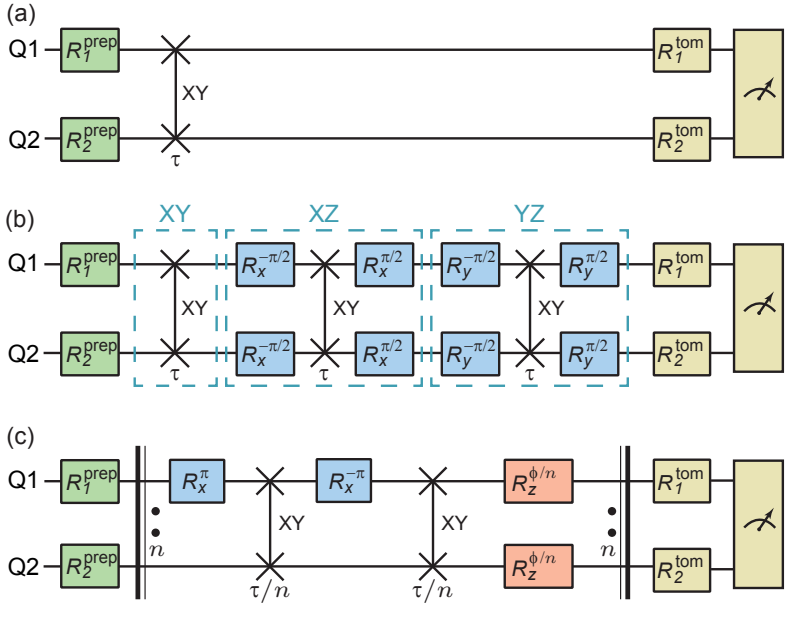

FIGURE 2.4: (a) Circuit diagram to characterize the XY exchange interaction on the qubits Q1 and Q2 symbolized by the vertical line (×) which is activated for a time τ. To perform standard process tomography of this interaction, separable initial states are prepared using single-qubit rotations $R_{1,2}^{\text{prep}}$ (green) in the beginning and the final state is characterized using single-qubit basis rotations $R_{1,2}^{\text{tom}}$ and joint two-qubit readout (yellow). (b) Digital quantum simulation of the two-spin Heisenberg (XYZ) interaction for time τ. The first step after state-preparation is to apply the XY gate for a time τ (dashed box labeled as XY). In the second and third steps (dashed boxes with labels XZ and YZ), XZ and YZ gates are realized using single-qubit rotations $R_{x,y}^{\pm\pi/2}$ (blue) by an angle $\pm\pi/2$ about the x or y axis transforming the basis in which the XY gate acts. (c) Protocol to decompose and simulate Ising spin dynamics in a homogeneous transverse magnetic field. The circuit between the bold vertical bars with two dots is repeated n times, invoking each XY and phase gates for a time τ/n. See text for details. The actual pulse scheme is provided in Appendix A.

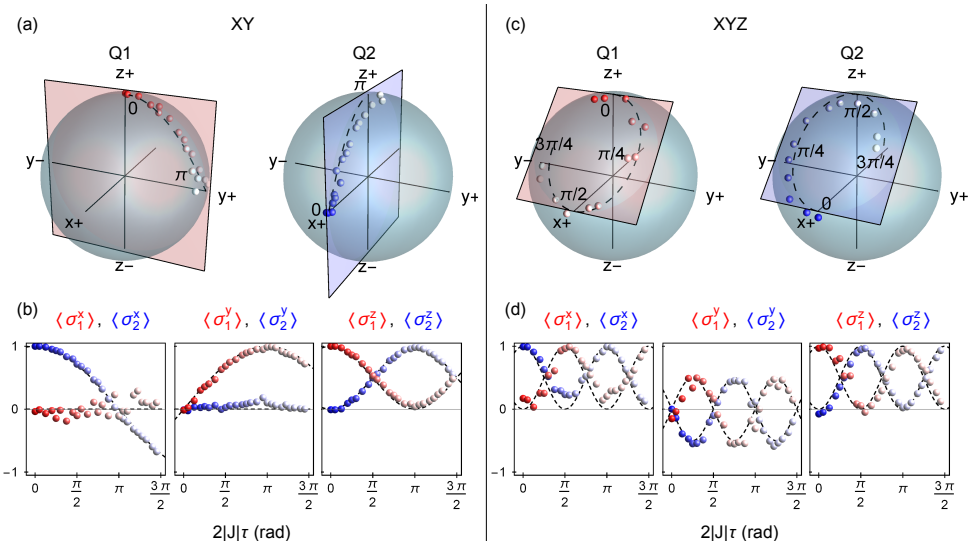

FIGURE 2.5: (a) Experimentally determined coordinates of the Bloch vectors during exchange (XY) interaction represented by small red (Q1) and blue (Q2) points are compared to the ideal paths shown as dashed lines in the XY model. The ideal paths are in the YZ and XZ planes shown as blue and red planes intersecting the Bloch sphere. The time evolution is indicated by the saturation of the colors as the quantum phase angle $2|J|\tau$ advances from 0 (saturated) to π (unsaturated). (b) Measured expectation values of the Pauli operators $\sigma_{1,2}^{x,y,z}$ for the qubits Q1 (red points) and Q2 (blue points), respectively, for the XY interaction as a function of the quantum phase angle $2|J|\tau$ along with the ideal evolution (dashed line). (c) Evolution of the Bloch vector for the quantum simulation of the isotropic Heisenberg interaction vs. quantum phase angles from 0 to $3\pi/4$. The path of the Bloch vectors of the qubits Q1 and Q2 spans the plane indicated by the rectangular sheets intersecting the Bloch spheres. (d), As in panel **b** for the Heisenberg interaction.

vectors do not remain on the surface of the Bloch sphere but rather lie within the sphere.

The anisotropic Heisenberg model describes spins interacting in three spatial dimensions

$$H_{xyz} = \sum_{(i,j)} (J_x \sigma_i^x \sigma_j^x + J_y \sigma_i^y \sigma_j^y + J_z \sigma_i^z \sigma_j^z), \tag{2.10}$$

where the sum is taken over pairs of neighbouring spins i and j. J_x, J_y and J_z are the couplings of the spins along the x, y and z coordinates, respectively. Since it does not occur naturally in circuit QED we decompose the Heisenberg interaction

into a sequence of XY and single-qubit gates, as shown in Fig. 2.4b. We combine three successive effective XY, XZ and YZ gates derived from the XY gate by basis transformations [94] to realize the isotropic Heisenberg model with $J_x = J_y = J_z = J$ versus interaction time τ. Since the XY, XZ and YZ operators commute for two spins the Trotter formula is exact after a single step.

To compare the Heisenberg (XYZ) interaction with the XY exchange interaction we have prepared the same initial state as presented in Fig. 2.5a,b. The isotropic Heisenberg interaction described by the scalar product between two vectorial spin 1/2 operators preserves the angle between the two spins. As a result, the initially perpendicular Bloch vectors of qubits Q1 and Q2 remain perpendicular during the interaction (Fig. 2.5c) and rotate clockwise along an elliptical path that spans a plane perpendicular to the diagonal at half angle between the two Bloch vectors (Fig. 2.5c).

In accordance with theory, the XYZ interaction leads to a full SWAP operation for a quantum phase angle of $2|J|\tau = \pi/2$ where the Bloch vectors point along the $+\mathbf{x}$ and $+\mathbf{z}$ directions. For the given initial state, we observed a maximum negativity of 0.210 close to the expected value of 0.25 for the Heisenberg interaction at a quantum phase angle of $2|J|\tau = \pi/4$. As for the XY interaction we have characterized the Heisenberg interaction with standard process tomography finding fidelities above 82 % for all quantum phase angles $2|J|\tau$.

Next, we consider the quantum simulation of the Ising model with a transverse homogeneous magnetic field

$$H_I = J \sum_{(i,j)} \sigma_i^x \sigma_j^x + \frac{B}{2} \sum_i \sigma_i^z, \tag{2.11}$$

where the magnetic field B pointing along the z axis is perpendicular to the interaction given by $J\sigma_i^x\sigma_j^x$. Since the two-spin evolution (Fig. 2.4c) is decomposed into two-qubit XY and single-qubit Z gates which do not commute, the transverse field Ising dynamics is only recovered using the Trotter expansion in the limit of a large number of steps n for an interaction time of τ/n in each step. To realize the Ising interaction term using the exchange interaction, the XY gate is applied twice for a time τ/n, once enclosed by a pair of π pulses on qubit Q1. This leads to a change of sign of the $\sigma_1^y\sigma_2^y$ term which thus gets canceled when added to the bare XY gate.

The external magnetic field part of the Hamiltonian is realized as single-qubit phase gates R_z^ϕ which rotate the Bloch vector about the z axis by an angle $\phi = B\tau/n$ per Trotter step. These gates are realized by detuning the respective qubit by an amount δ from its idle frequency corresponding to an effective B-field strength of $B = 2\pi\delta$.

We experimentally simulate the non-stationary dynamics of two spins in this model for the initial state $|\uparrow\rangle(|\uparrow\rangle - i|\downarrow\rangle)/\sqrt{2}$ which is well-suited to assess the simulation performance. In Fig. 2.6a expectation values for the digital simulation of the $\sigma_{1,2}^z$-components of the two spins are shown, as well as the two-point correlation function $\langle\sigma_1^x\sigma_2^x\rangle$. The $\sigma_{1,2}^z$-components of the spins represented by the red and blue datasets in Fig. 2.6a, respectively, oscillate with a dominant frequency component of $2J$ due to the presence of the interaction term $\propto \sigma_1^x\sigma_2^x$. Likewise, the XX correlation $\langle\sigma_1^x\sigma_2^x\rangle$ represented by the yellow dataset in Fig. 2.6a is non-stationary and oscillates at rate $2\sqrt{B^2+J^2} = 2\sqrt{10}J \approx 6.3J$ due to the presence of a magnetic field of strength $B = 3J$. The evolution of the measured final state shows agreement with a theoretical model (solid lines in Fig. 2.6a) which takes into account dissipation and decoherence with deviations being dominated by systematic gate errors, see Appendix A.

In Fig. 2.6b, the fidelity of the simulated state is compared to the expected state at characteristic quantum phase angles both for the experimental realization (colored bars) and the ideal Trotter approximation (wire frames) after the nth step. In an ideal digital quantum simulator the theoretical fidelity (wire frame) converges for an increasing number of steps n (Fig. 2.6b). The experimental fidelity, however, reaches a maximum for a finite number of steps (Fig. 2.6b) after which it starts to decrease due to gate errors and decoherence [94]. As expected, the Trotter approximation converges faster for smaller quantum phase angles $2|J|\tau$. For $2|J|\tau = \pi/4$ the peak experimental fidelity (Fig. 2.6b) of 98.3 % is already observed for $n = 1$, whereas for $2|J|\tau = 3\pi/2$ the optimum of 80.7 % is observed for $n = 5$.

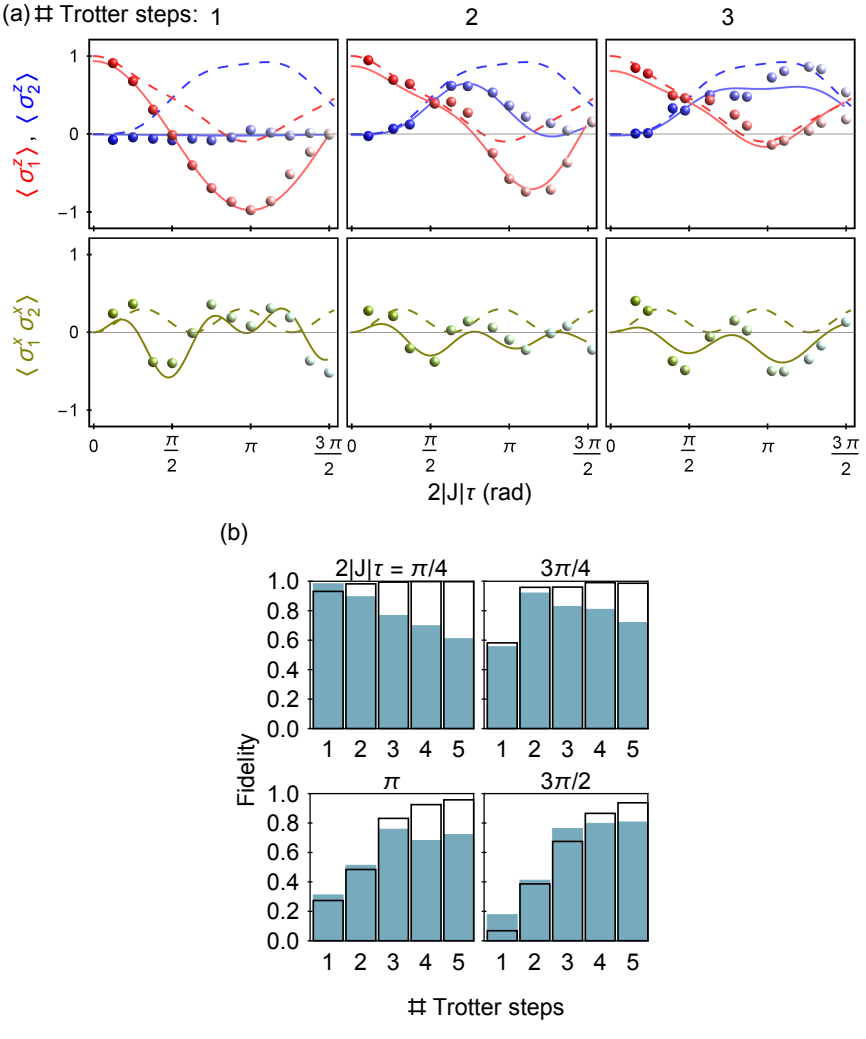

FIGURE 2.6: (a) Digital quantum simulation of the Ising model with transverse homogeneous magnetic field using 1 to 3 Trotter steps. Shown are the z-components $\langle\sigma_1^z\rangle$ of qubit Q1 (red) and $\langle\sigma_2^z\rangle$ of qubit Q2 (blue) and the two-point correlation function in the x-direction $\langle\sigma_1^x\sigma_2^x\rangle$ (yellow points) of the spins as a function of the quantum phase angle $2|J|\tau$ for the initial state $|\uparrow\rangle(|\uparrow\rangle - i|\downarrow\rangle)/\sqrt{2}$ and a magnetic field strength $B = 3J$. Theoretically expected results take systematic phase offsets and finite coherence of the qubits into account (solid curves). The ideal dynamics are obtained from the time-dependent Schrödinger equation for the Ising Hamiltonian (dashed lines). (b) Fidelity with respect to the exactly solved Ising model for displayed quantum phase angles of the final state after ideal unitary evolution in the simulation protocol for n Trotter steps (wire frames) and experimentally obtained final state (colored bars).

2.6 Conclusions

In this Chapter, we have proposed a digital quantum simulation of spin models in superconducting circuits. We have considered prototypical models such as the Heisenberg and frustrated Ising interactions. Furthermore, we have shown the feasibility of the simulation with state-of-the-art technology of transmon qubits coupled to microwave resonators. Finally, we have experimentally analyzed the digitized physical implementation of effective spin interactions by using a superconducting architecture involving two transmon qubits coupled by a transmission line resonator.

In future experiments, transmission line resonators may provide a method to design multi-qubit devices with non-local qubit-qubit couplings that directly reflect the lattice topology of spin systems such as frustrated magnets. Moreover, the incorporation of cavity modes as explicit degrees of freedom in the simulated models [27], following a digital-analog approach, and the integration of optimal control concepts, will be instrumental to scale the system to larger Hilbert-space dimensions. With this, the circuit QED architecture offers considerable potential for surpassing the limitations of classical simulations, which can be facilitated by using efficient digital decompositions of spin Hamiltonians, paving the way towards universal quantum simulation of spin dynamics in circuit QED setups.

Chapter 3

Digital-Analog Quantum Rabi and Dicke Models

Fools ignore complexity. Pragmatists suffer it. Some can avoid it. Geniuses remove it.

Alan Perlis

3.1 Introduction

The simplest, most fundamental model describing the interaction between quantum light and quantum matter is the quantum Rabi model, consisting of the dipolar coupling of a two-level system with a single radiation mode [52]. The Dicke model [54] was introduced afterwards to generalize this interaction to an ensemble of N two-level systems. Typically, the coupling strength is small compared to the transition frequencies of the two-level system and the radiation mode, which leads to effective Jaynes-Cummings and Tavis-Cummings interactions, respectively, after performing a rotating-wave approximation (RWA). This introduces a $U(1)$ symmetry into the model, which makes it integrable for any N [53, 55]. Recently, analytical solutions for the generic quantum Rabi and Dicke models for $N = 3$ were found [56, 95].

However, the general case for arbitrary N is still unsolved, while its direct implementation in a physical system remains as an outstanding challenge.

A variety of quantum platforms, such as cavity QED, trapped ions, and circuit QED, provides a natural implementation of the Jaynes-Cummings and Tavis-Cummings models, due to the strong qubit-mode coupling strength. When the latter is a fraction or comparable to the mode frequency, the model is said to be in the ultrastrong coupling (USC) regime. Experimental evidence of this regime has been observed in the optical [96] and microwave domains [33, 34]. A coupling strength larger than the mode frequency marks the transition towards the recently introduced deep-strong coupling (DSC) regime [35]. Signatures of this regime may be effectively retrieved in different quantum systems [78, 97], but an experimental observation of the full quantum Rabi and Dicke models in all parameter regimes has not yet been realized. In particular, the quantum simulation of the Dicke Hamiltonian could outperform analytical and numerical methods, while enabling the simulation of engineered superradiant phase transitions [98–100]. Recently, technological improvements of controlled quantum platforms have increased the interest in quantum simulations [5, 12, 101, 102]. A digital approach to quantum simulations was put forward by Lloyd [19]. In this sense, it has been analyzed how suitable versions of digital quantum simulators can be implemented with available quantum platforms [23, 82, 83, 94]. Standard digital quantum simulations focus on the efficient decomposition of the quantum system dynamics in terms of elementary gates. In order to maximize the efficiency of the simulation, one may analyze which is the decomposition of the dynamics in its largest realizable parts, and reduce the number of elementary interactions in the simulation. This approach can be denoted as digital-analog quantum simulation and corresponds to finding some terms in the simulated system that can be implemented in an analog way, e.g., to employ a harmonic oscillator to simulate a bosonic field, while others will be carried out with a digital decomposition.

In this Chapter, we propose the digital-analog quantum simulation of the quantum Rabi and Dicke models in a circuit QED setup, having access only to Jaynes-Cummings and Tavis-Cummings interactions, respectively. We show how the rotating and counter-rotating contributions can be effectively realized employing digital techniques. By interleaved implementation of rotating and counter-rotating steps, the

dynamics of the quantum Rabi and Dicke models can be simulated for all parameter regimes with bounded error. Lastly, we show how a relativistic Dirac dynamics can be retrieved in the limit in which the mode frequency cancels. To finish, we review the experiment realized by the group of Prof. Leonardo DiCarlo at Delft University of Technology.

3.2 Digital-Analog Decomposition of the Quantum Rabi Model

We start by considering a generic circuit QED setup consisting of a charge-like qubit, e.g. a transmon qubit [45], coupled to a microwave resonator. The setup is well described by the Hamiltonian ($\hbar = 1$) [37]

$$H = \omega_r a^\dagger a + \frac{\omega_q}{2}\sigma^z + g(a^\dagger \sigma^- + a\sigma^+), \tag{3.1}$$

where ω_r and ω_q are the resonator and qubit transition frequencies, g is the resonator-qubit coupling strength, $a^\dagger(a)$ is the creation(annihilation) operator for the resonator mode, and $\sigma^\pm$ raise and lower excitations on the qubit. The capacitive interaction in Eq. (3.1) excludes excitations of the higher levels of the qubit device, because typically the coupling g is much smaller than other transition frequencies of the system. By trying to design setups with larger capacitive couplings, pushing them above dispersive regimes, one starts to populate the higher levels of the transmons, producing unwanted leakage. On the other hand, methods based on orthogonal drivings of the qubits [78, 79] may increase the resonator population. Here, we show that the dynamics of the quantum Rabi Hamiltonian

$$H_R = \omega_r^R a^\dagger a + \frac{\omega_q^R}{2}\sigma^z + g^R \sigma^x (a^\dagger + a) \tag{3.2}$$

can be encoded in a superconducting setup provided with a Jaynes-Cummings interaction, as in Eq. (3.1), using a digital expansion. The quantum Rabi Hamiltonian in

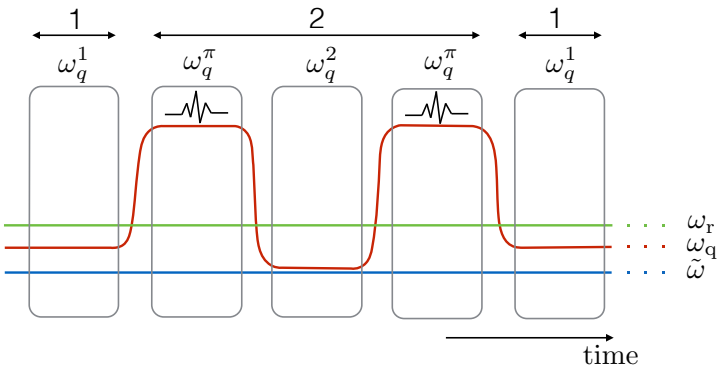

FIGURE 3.1: Frequency scheme of the stepwise implementation for the quantum Rabi Hamiltonian. A transmon qubit of frequency ω_q is interacting with a microwave resonator, whose transition frequency is ω_r. The interactions $H_{1,2}$ in Eq. (3.3) are simulated respectively with a Jaynes-Cummings interaction (step 1), and another one with different detuning, anticipated and followed by π pulses (step 2).

Eq. (3.2) can be decomposed into two parts, $H_R = H_1 + H_2$, where

$$\begin{aligned} H_1 &= \frac{\omega_r^R}{2} a^\dagger a + \frac{\omega_q^1}{2}\sigma^z + g(a^\dagger\sigma^- + a\sigma^+), \\ H_2 &= \frac{\omega_r^R}{2} a^\dagger a - \frac{\omega_q^2}{2}\sigma^z + g(a^\dagger\sigma^+ + a\sigma^-), \end{aligned} \tag{3.3}$$

and we have defined the qubit transition frequency in the two steps such that $\omega_q^1 - \omega_q^2 = \omega_q^R$. These two interactions can be simulated in a typical circuit QED device with fast control of the qubit transition frequency. Starting from the qubit-resonator Hamiltonian in Eq. (3.1), one can define a frame rotating at frequency $\tilde{\omega}$, in which the effective interaction Hamiltonian becomes

$$\tilde{H} = \tilde{\Delta}_r a^\dagger a + \tilde{\Delta}_q \sigma^z + g(a^\dagger\sigma^- + a\sigma^+), \tag{3.4}$$

with $\tilde{\Delta}_r = (\omega_r - \tilde{\omega})$ and $\tilde{\Delta}_q = (\omega_q - \tilde{\omega})/2$. Therefore, Eq. (3.4) is equivalent to H_1, following a proper redefinition of the coefficients. The counter-rotating term H_2 can be simulated by applying a local qubit rotation to $\tilde{H}$ and a different detuning for the qubit transition frequency,

$$e^{-i\pi\sigma^x/2}\tilde{H}e^{i\pi\sigma^x/2} = \tilde{\Delta}_r a^\dagger a - \tilde{\Delta}_q\sigma^z + g(a^\dagger\sigma^+ + a\sigma^-). \tag{3.5}$$

By choosing different qubit-resonator detuning for the two steps, $\tilde{\Delta}_q^1$ for the first one and $\tilde{\Delta}_q^2$ for the rotated step, one is able to simulate the quantum Rabi Hamiltonian, Eq. (3.2), via digital decomposition [19], by interleaving the simulated interactions. The frequency scheme of the protocol is shown in Fig. 3.1. Standard resonant Jaynes-Cummings interaction parts with different qubit transition frequencies are interrupted by microwave pulses, in order to perform customary qubit flips [103]. This sequence can be repeated according to the digital simulation scheme to obtain a better approximation of the quantum Rabi dynamics.

3.3 Implementation in Superconducting Circuits

The simulated Rabi parameters can be obtained as a function of the physical parameters of the setup by inverting the derivation presented above. In this way, one has that the simulated bosonic frequency is related to the resonator detuning $\omega_r^R = 2\tilde{\Delta}_r$, the two-level transition frequency is related to the transmon frequency in the two steps, $\omega_q^R = \tilde{\Delta}_q^1 - \tilde{\Delta}_q^2$, and the coupling to the resonator remains the same, $g^R = g$. Notice that even if the simulated two-level frequency ω_q^R depends only on the frequency difference, large detunings $\tilde{\Delta}_q^{1(2)}$ will affect the total fidelity of the simulation. In fact, since the digital error depends on the magnitude of individual commutators between the different interaction steps, using larger detunings linearly increases the latter, which results in fidelity loss of the simulation. To minimize this loss, one can choose, for example, the transmon frequency in the second step to be tuned to the rotating frame, such that $\tilde{\Delta}_q^2 = 0$. Nevertheless, to avoid sweeping the qubit frequency across the resonator frequency, one may choose larger detunings. To estimate the loss of fidelity due to the digital approximation of the simulated dynamics, we consider a protocol performed with typical transmon qubit parameters [45]. We estimate a resonator frequency of $\omega_r/2\pi = 7.5$ GHz, and a transmon-resonator coupling of $g/2\pi = 100$ MHz. The qubit frequency ω_q and the frequency of the rotating frame $\tilde{\omega}$ are varied to reach different parameter regimes.

To perform the simulation for the quantum Rabi model with $g^R/2\pi = \omega_q^R/2\pi = \omega_r^R/2\pi = 100$ MHz, for example, one can set $\omega_q^1/2\pi = 7.55$ GHz, $\omega_q^2/2\pi = 7.45$ GHz.

TABLE 3.1: Simulated quantum Rabi dynamics parameters versus frequencies of the system. For all entries in the right column, the resonator frequency is fixed to $\omega_r/2\pi = 7.5$ GHz, and the coupling $g^R/2\pi = 100$ MHz. Frequencies are shown up to a 2π factor.

$g^R = \omega_q^R/2 = \omega_r^R/2$	$\tilde{\omega} = 7.4$ GHz, $\omega_q^1 - \omega_q^2 = 200$ MHz
$g^R = \omega_q^R = \omega_r^R$	$\tilde{\omega} = 7.45$ GHz, $\omega_q^1 - \omega_q^2 = 100$ MHz
$g^R = 2\omega_q^R = \omega_r^R$	$\tilde{\omega} = 7.475$ GHz, $\omega_q^1 - \omega_q^2 = 100$ MHz

In this way, one can define an interaction picture rotating at $\tilde{\omega}/2\pi = 7.45$ GHz to encode the dynamics of the quantum Rabi model with minimal fidelity loss. Considering that single-qubit rotations take approximately ~ 10 ns, tens of Trotter steps could be comfortably performed within the coherence time. Notice that, in performing the protocol, one has to avoid populating the third level of the transmon qubit. Taking into account transmon anharmonicities of about $\alpha = -0.1$, for example, in this case one has third level transition frequencies of 6.795 GHz and 6.705 GHz. Therefore, given the large detuning with the resonator, it will not be populated. Similarly, by choosing different qubit detunings and rotating frames, one can simulate a variety of parameter regimes, e.g. see Table 3.1.

In order to capture the physical realization of the simulation, we plot in Fig. 3.2 the behavior of the transmon-resonator system during the simulation protocol. We numerically integrate a master equation, alternating steps of Jaynes-Cummings interaction with single-qubit flip pulses. We consider $\dot{\rho} = -i[H,\rho] + \kappa L(a)\rho + \Gamma_\phi L(\sigma^z)\rho + \Gamma_- L(\sigma^-)\rho$, with Jaynes-Cummings terms $\tilde{H} = \tilde{\Delta}_r a^\dagger a + \tilde{\Delta}_q \sigma^z + g(a^\dagger\sigma^- + a\sigma^+)$, alternated with qubit-flip operations $H_f = f(t)\sigma^x$, where $f(t)$ is a smooth function such that $\int_0^{T_f} f(t)dt = \pi/2$, T_f being the qubit bit-flip time. The quantum dynamics is affected by Lindblad superoperators $\Gamma_\phi L(\sigma^z)\rho$, $\Gamma_- L(\sigma^-)\rho$, and $\kappa L(a)\rho$ modelling qubit dephasing, qubit relaxation and resonator losses. We have defined $L(A)\rho = (2A\rho A^\dagger - A^\dagger A\rho - \rho A^\dagger A)/2$. We set a resonator-qubit coupling of $g/2\pi = 80$ MHz, and a frame rotating at the qubit frequency, $\tilde{\Delta}_q = 0$, $\tilde{\Delta}_r/2\pi = 40$ MHz. We consider $\Gamma_-/2\pi = 30$ kHz, $\Gamma_\phi/2\pi = 60$ kHz, and $\kappa/2\pi = 100$ kHz. The inset of Fig. 3.2 shows collapses and revivals of both the photon and spin dynamics, which are typical signatures of the regimes of the quantum Rabi dynamics dominated by the coupling strength. We consider prototypical DSC dynamics, with $\omega_q^R = 0$, and $g^R = \omega_r^R$. Notice that to encode the dynamics corresponding to a certain simulated time t, one

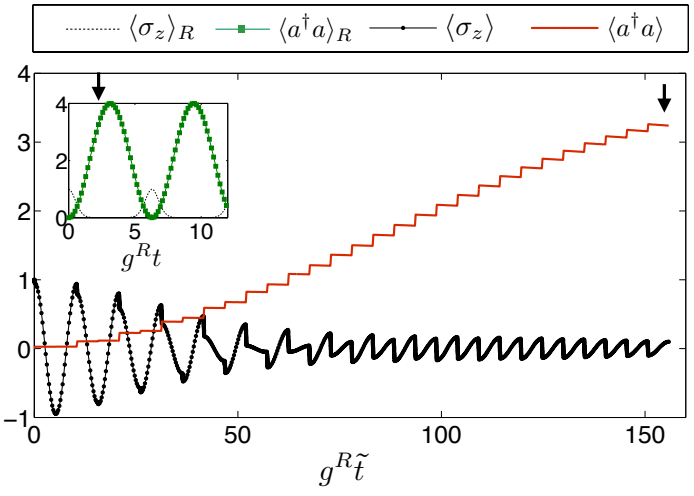

FIGURE 3.2: A transmon qubit and microwave resonator simulating the quantum Rabi Hamiltonian in the regime $g^R = \omega_r^R$, $\omega_q^R = 0$. The ideal dynamics, plotted in the inset, shows collapses and revivals of the photon and qubit population. The latter are recovered via sequential qubit-resonator interactions and qubit flips. The photon population is pumped to the expected value at the time marked by the arrow. Note that the simulating time $\tilde{t}$ is different from the simulated time t.

needs the quantum simulator to run for a simulating time $\tilde{t}$, that depends on the specific gate times of the experiment. We choose to set the simulation at the time marked by the black arrow, close to the photon population peak in the inset. A simulation with 15 digital steps is then performed. The time for a single qubit flip pulse is set to $T_f = 10$ ns. Periodic collapses and revivals of the bosonic population of the quantum Rabi model $\langle a^\dagger a\rangle_R$ are shown as a function of time, in the inset. The ideal spin and bosonic populations $\langle\sigma_z\rangle_R$ and $\langle a^\dagger a\rangle_R$, evolving according to the quantum Rabi Hamiltonian, are shown to be in good agreement with the simulated ones, $\langle\sigma_z\rangle$ and $\langle a^\dagger a\rangle$, at the final simulated time. In fact, during the Jaynes-Cummings interaction parts, photons are pumped into the resonator. Afterwards, before the photon population starts to decrease due to excitation exchanges with the transmon qubit, a qubit flip further enhances the photon production.

The simulation protocol can be performed for every time of the dynamics, with the number of digital steps tuned to reach a satisfactory simulation fidelity. We plot in Fig. 3.3 the fidelity $F = |\langle\Psi_S\Psi_R\rangle|^2$ as a function of time of the simulated

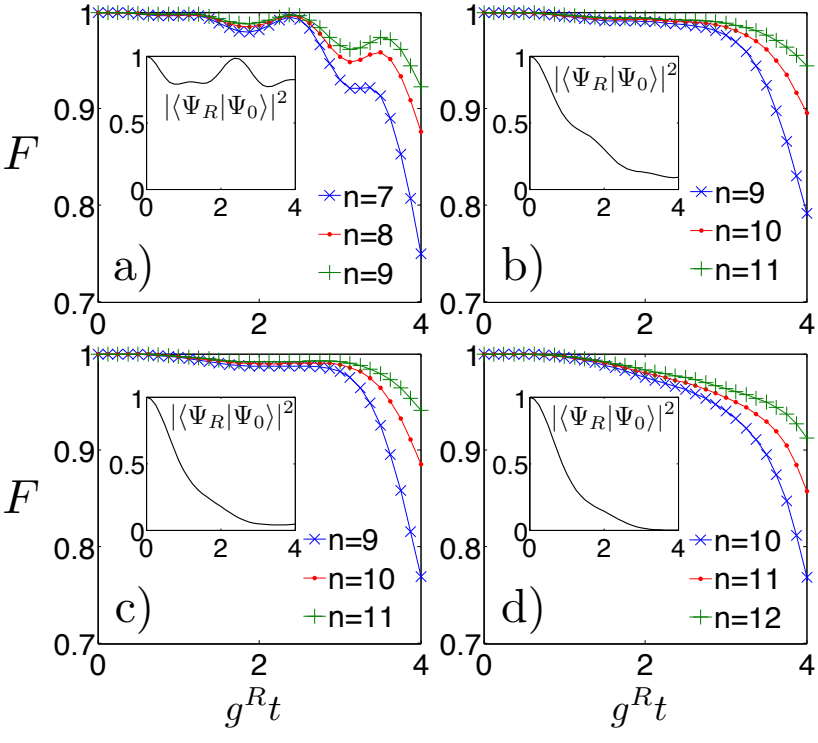

FIGURE 3.3: Time evolution of the fidelity $F = |\langle\Psi_S|\Psi_R\rangle|^2$ of state $|\Psi_S\rangle$ evolving according to the digitized protocol, to the ideal state $|\Psi_R\rangle$ evolving according to the quantum Rabi dynamics, with a) $g^R = \omega_r^R/2 = \omega_q^R/2$, b) $g^R = \omega_r^R = \omega_q^R$, c) $g^R = 2\omega_r^R = \omega_q^R$, and d) $g^R = 2\omega_r^R = 1.5\omega_q^R$. The simulation is performed for different number n of Trotter steps. Black curves in the insets show the overlap of the ideal evolved state with the one at time $t = 0$, $|\langle\Psi_R|\Psi_0\rangle|^2$, initialized with a fully excited qubit and the resonator in the vacuum state.

wavefunction Ψ_S, including resonator and spin degrees of freedom, versus the ideal one Ψ_R, evolving according to H_R, as defined in Eq. (3.2). The fidelity is plotted for different parameters and iteration steps. Increasing the number of steps, the fidelity grows as expected from standard Suzuki-Lie-Trotter expansions [21]. In principle, the whole protocol can accurately access non-analytical regimes of these models, including USC and DSC regimes.

3.4 Extension to Dicke Model and Dirac Equation

By adding several transmon qubits to the architecture, the presented method can be extended to simulate the Dicke Hamiltonian

$$H_D = \omega_r^R a^\dagger a + \sum_{j=1}^{N} \frac{\omega_q^R}{2} \sigma_j^z + \sum_{j=1}^{N} g^R \sigma_j^x (a^\dagger + a). \tag{3.6}$$

This simulation can be efficiently implemented by means of collective qubit rotations. In fact, only collective Tavis-Cummings interactions and global qubit rotations are involved. In this way, the total time for the simulation does not scale with the size of the system N. The Dicke model can be investigated provided enough coherence and low-enough gate errors. Notice that this kind of quantum simulation is well suited for superconducting circuits, since simultaneous single-qubit addressing is possible. Making use of the results in Refs. [84, 104], we demonstrate that the quantum resources needed to approximate the Dicke Hamiltonian with an error less than ϵ scale efficiently with the number of spins N and of excitations allowed in the bosonic mode M. In a Dicke model simulation, one can bound the number of gates N_ϵ necessary to achieve a certain error ϵ in a time t by

$$N_\epsilon \leq \frac{2 \cdot 5^{2k} \left\{ 2t[\omega_r^R M + N(\omega_q^R + 2|g^R|\sqrt{M+1})] \right\}^{1+1/2k}}{\epsilon^{1/2k}}. \tag{3.7}$$

Here, we have used an upper bound for the norm of the Dicke Hamiltonian, $||H_R|| \leq \omega_r^R M + N(\omega_q^R + 2|g^R|\sqrt{M+1})$, where M is a truncation on the number of bosonic excitations involved in the dynamics. The fractal depth is set to $k = 1$ in the standard Trotter approximations. Using higher orders of fractal decompositions would be a more involved task for implementation of digital approximations in realistic devices, due to the sign inversion that appears [21]. Nevertheless, unitary approximants with arbitrarily high fidelity can be obtained even when $k = 1$. The formula in Eq. (3.7) gives an upper bound to the scaling of quantum resources and experimental errors in a simulation involving several qubits. In fact, if one considers a small error for each gate, the accumulated gate error grows linearly with the number of gates.

Notice that the quantum dynamics of the Dirac Hamiltonian emerges as a specific case of the quantum Rabi dynamics. For the 1+1 dimensional case the algebra of

the Dirac spinors $|\Psi\rangle$ corresponds to that of Pauli matrices, and the Dirac equation in the standard representation can be written

$$i\frac{d}{dt}|\Psi\rangle = (mc^2\sigma_z + cp\sigma_x)|\Psi\rangle, \tag{3.8}$$

where m is the mass of the particle, c is the speed of light and $p \propto (a - a^\dagger)/i$ is the one-dimensional momentum operator. The Dirac Hamiltonian in Eq. (3.8), $H_\mathrm{D} = mc^2\sigma_z + cp\sigma_x$, shows the same mathematical structure as the quantum Rabi Hamiltonian, Eq. (3.2), when $\omega_r^R = 0$. This condition can be achieved by choosing $\tilde{\omega} = \omega_r$. The analogy is complete by relating mc^2 to $\omega_q^R/2$, c to g^R, and the momentum to the quadrature of the microwave field, which can be measured with current microwave technology [105]. Choosing an initial state with components in both positive and negative parts of the Dirac spectrum will allow the measurement of the *Zitterbewegung* [9, 106]. By retrieving different quadratures of the microwave field, one can detect this oscillatory motion of the simulated particle in the absence of forces, and the Klein paradox, where a relativistic particle can tunnel through high-energy barriers. To detect such effects, one will be interested in measuring either the position or the momentum of the particle, standing for different quadratures of the microwave field.

3.5 Experimental Realization

Recently, this proposal has been experimentally realized in the lab of Prof. Leonardo DiCarlo at Delft University of Technology, demonstrating the feasibility of digital-analog methods to simulate the quantum Rabi model. Here, regimes of ultrastrong and deep-strong coupling have been achieved by the stepwise implementation of Jaynes-Cummings and anti-Jaynes-Cummings dynamics as described above in this Chapter.

Fidelities expected in the original proposal as well as the number of implemented Trotter steps have been overcome in this experiment, in which Wigner function of the system has been measured. Here, the symmetric approach of Trotter expansion has been followed, which cancels the first-order term in the Trotter error. As a result of the combination of this technique with the capability to introduce more than 90

Trotter steps, accurate simulations of Rabi model have been achieved. Furthermore, physical properties of USC and DSC regimes have been reproduced, such as creation of Schrödinger cat states of large photon numbers among others.

3.6 Conclusions

In this Chapter, we have shown that the dynamics of the quantum Rabi and Dicke models can be encoded in a circuit QED setup using a digital-analog approach. The use of these techniques provides both the flexibility to implement unnatural dynamics in a quantum system and the complexity of analog simulations involving, for instance, bosonic modes. Digital-analog quantum simulations will contribute to the observation of quantum dynamics in regimes not accessible in current experiments of purely analog quantum simulations, including USC, DSC and unexplored zones of the quantum Rabi model, due to the accessibility to an arbitrary set of parameters. Finally, we have mentioned the experimental realization of this proposal, made in the lab of Prof. Leonardo DiCarlo at Delft University of Technology, where physical properties of quantum Rabi model in USC and DSC regimes have been reproduced with high fidelities.

Chapter 4

Digitized Adiabatic Quantum Simulation of Spin Chains

Change always involves a dark night when everything falls apart. Yet if this period of dissolution is used to create new meaning, then chaos ends and new order emerges.

Margaret Wheatley

4.1 Introduction

As already explained in the previous Chapter, a two-level system coupled with a single radiation mode is modeled by the ubiquitous and paradigmatic quantum Rabi model [52]. There have been many efforts, in both theory and experiments, to capture the features of this model in different quantum technologies [5, 107]. These analyses will expectively have an impact in understanding of different quantum phenomena [33, 35, 108–111].

The concept of a quantum simulator can be attributed to Feynman [1], and it refers to a controllable quantum platform that mimics the behaviour of another

quantum system. Some analog quantum simulators have already been implemented in different quantum technologies, such as trapped ions [82, 83], ultracold atoms [12], or superconducting circuits [78–80, 112]. Similarly, quantum simulators based on digital methods [19] in order to simulate dynamics of quantum systems have been realized in trapped ions [23], photonic systems [81], spin-photon hybrid systems [113] and superconducting circuits [24, 25, 27, 94, 114, 115]. Additionally, this methods can be combined with adiabatic quantum computing protocols [116–118], in which the state of a quantum system is slowly evolved from the ground state of a simple initial Hamiltonian to a final Hamiltonian that encodes a computational problem. The appeal lies in the combination of simplicity and generality; in principle, any problem can be encoded. In practice, applications are restricted by limited connectivity, available interactions, and noise.

A key challenge in adiabatic quantum computing is to construct a device that is capable of encoding problem Hamiltonians that are non-stoquastic [119]. Such Hamiltonians would allow for universal adiabatic quantum computing [120, 121] as well as improving the performance for difficult instances of classical optimization problems [122]. Additionally, simulating interacting fermions for physics and chemistry requires non-stoquastic Hamiltonians [1, 123]. In general, non-stoquastic Hamiltonians are more difficult to study classically, as Monte Carlo simulations fail to converge due to the sign problem [124]. A hallmark of non-stoquastic Hamiltonians is the need for several distinct types of coupling, for example containing both $\sigma_z\sigma_z$ and $\sigma_x\sigma_x$ couplings with different signs. With a digitized approach, different couplings can be constructed without change of hardware. Long-range many-body interactions can be assembled to aid in quantum tunneling [125] or to encode the non-local terms for fermionic simulations [7, 126]. And finally, noise in analog systems can thwart the evolution, whereas digital systems can be fully fault-tolerant. Crucially, this ability makes the approach scalable, as any non-corrected implementation is ultimately limited by the accumulation of error.

In this Chapter, we analyze the quantum simulation of arbitrary spin models, where spin chains alone or coupled to bosonic modes are emulated with superconducting circuits [30]. We use digital techniques in order to imitate systems whose dynamics may in principle differ from the ones of the experimental setups. We study the feasibility and efficiency of the implementation of three generic models in

a realistic circuit quantum electrodynamics setup. In addition, we employ digitized adiabatic quantum computing algorithms to simulate time-dependent couplings in an Ising-like spin chain, and we analyze the experimental results obtained in the lab of Prof. John Martinis at Google/University of California, Santa Barbara.

4.2 Digitized Adiabatic Quantum Simulations

The goal of simulating diverse and generic models involving spin interactions and bosonic modes leads us to consider digital techniques, due to their suitability and flexibility for mimicking different dynamical structures. Hamiltonian dynamics can be approximated by the digital decomposition of the exact unitary evolution into discrete stepwise unitary operations, implemented by using quantum gates in an efficient way [19, 21]. Digital methods are based on the Trotter formula, which allows us to expand the evolution operator of Hamiltonians that are written as a sum of terms, $H = \sum_{j=1}^{N} H_j$, into a product of evolution operators for the interactions given by the summands of the Hamiltonian, H_j. The Trotter expansion can be written as

$$e^{-iHt} = \left(e^{-iH_1 t/s} \cdots e^{-iH_N t/s}\right)^s + \sum_{i<j} \frac{[H_i, H_j]\, t^2}{2s} + \sum_{k=3}^{\infty} E(k), \tag{4.1}$$

where the total time of the simulated dynamics is divided into s intervals in which the evolution associated to each summand of the complete Hamiltonian are applied. The error scales with t^2/s for short times, as can be observed in the second term, and the upper bound for higher order error contributions is $s\|Ht/s\|_{\sup}^k/k! \geq \|E(k)\|_{\sup}$.

As a complementary approach, in adiabatic quantum computing, the solution of a problem is encoded in the ground state of a Hamiltonian [116, 127]. In order obtain it, a system is initialized in the ground state of a simple Hamiltonian, and it is evolved adiabatically to the desired complex Hamiltonian following the expression

$$H(r) = f_1(r)H_I + f_2(r)H_P, \tag{4.2}$$

where H_I is the initial Hamiltonian, H_P is the problem Hamiltonian, and f_1 (f_2) is an increasing (decreasing) time-dependent function that fulfills $f_1(r_{initial}) = f_2(r_{final}) =$

1 and $f_2(r_{initial}) = f_1(r_{final}) = 0$. According to the adiabatic theorem [128], the evolution time Δr must be long enough to avoid excitations, so the smaller the energy-gap is between ground and first-excited state, the larger the evolution time must be, $\Delta r = O(1/\min(E_{gap}))$ with $E_{gap}(r) = E_1(r) - E_0(r)$. This method has been shown to be polynomially equivalent to conventional quantum computing in the circuit model [129].

Our goal is to propose a systematic procedure using digital methods for simulating efficiently different models, namely spin-spin interaction and spins coupled to bosonic modes. First, we employ gates that commute with each other and do not produce digital error. For those that do not commute, we apply several Trotter steps because the more Trotter steps one applies, the smaller the digital error produced is. In realistic experiments, one has to take into account decoherence times and gate errors. Therefore, we have to regulate the number of steps in order to be able to perform the simulation before decoherence effects take place, and in order to reduce the accumulated gate error. Consequently, once the digital error is small enough applying a certain number of Trotter steps, the error coming from the experimental setup always must be smaller than the digital one.

Similarly, protocols combining adiabatic quantum computing and digitization of gates can realized. Here, instead of implementing a Hamiltonian that changes continuously in time as in standard adiabatic evolutions, a discretized set of unitary gates are performed in such a way the variation in time of the Hamiltonian is simulated. The simplest form to do it is to discretize linearly the variation in time of the Hamiltonian in p steps, and implement the unitary evolution of the corresponding p constant Hamiltonians.

$$U_{\text{adiabatic}} = \prod_{k=1}^{p} e^{-iH_k \frac{\Delta r}{p}}, \tag{4.3}$$

where each of the discretized Hamiltonians $H_k = H_I - (H_I - H_P)\frac{k-1/2}{p}$ are applied for a time $\frac{\Delta r}{p}$. Moreover, if the system does not provide the required unitary evolutions, they can be performed using the digital approach as in Eq. (4.1). In these simulations, besides experimental errors, adiabatic and Trotter errors must be taken into account.

4.3 Simulation of Spin Chains Coupled to Bosonic Modes

In this section, we present a method to implement the dynamics of several spin models, coupled with bosonic modes, in circuit quantum electrodynamics setups. For this purpose, we take under consideration two different architectures of superconducting circuits. We show how to use linear arrays of superconducting qubits with capacitive coupling between nearest neighbors [17] to simulate the Ising model with transverse field. Then we simulate the behavior of a spin-chain coupled to a bosonic mode via a Tavis-Cummings interaction [55]. Moreover, we show how to implement many-body spin dynamics with highly nonlinear terms in superconducting qubits coupled to transmission line resonators acting as a quantum bus [39].

In the following, we propose digital quantum simulations based on quantum gates implemented in superconducting architectures. Capacitive coupling setups allow one to implement ZZ gates, $\exp(-i\theta\sigma_j^z\sigma_k^z)$, for nearest-neighbor superconducting qubits by the sequence of two single qubit rotations along the z axis, $Z(\phi)$, and a c-phase gate, $CZ(\phi)$, as shown in Fig. 4.1, where

$$Z(\phi) = \begin{pmatrix} 1 & 0 \\ 0 & e^{i\phi} \end{pmatrix}, \; CZ(\phi) = \begin{pmatrix} 1 & 0 & 0 & 0 \\ 0 & 1 & 0 & 0 \\ 0 & 0 & 1 & 0 \\ 0 & 0 & 0 & e^{-i2\phi} \end{pmatrix}. \tag{4.4}$$

The current achievable fidelities in superconducting circuits [17] are of 99.9% and 99.4% for the single and two-qubit (CZ) gates, respectively. They enable circuit QED setups to be great candidates for digital quantum simulators where the stroboscopic application of gates is necessary. Notice that $ZZ_{12}(\theta) = (Z_1(\phi) \otimes Z_2(\phi))CZ_{12}(\phi)$ for $\theta = \phi/2$.

The use of quantum buses allows for the implementation of multi-qubit gates and spin-boson interactions, coupling the electromagnetic field in the resonator with superconducting circuits [59, 77, 130, 131].

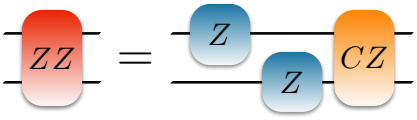

FIGURE 4.1: Protocol for decomposing a ZZ interaction between two qubits using single-qubit rotations, Z, and a c-phase gate, CZ.

4.3.1 Ising Model with Transverse Field via Capacitive Nearest-Neighbour Gates

One of the most studied spin models in condensed matter is the Ising model with a transverse field, which is used for describing the behavior of interacting nearest-neighbor dipoles in the presence of a transverse magnetic field. The Hamiltonian of N spins can be written as

$$H_{ITF} = J \sum_{\langle jk \rangle} \sigma_j^z \sigma_k^z + B \sum_j \sigma_j^x, \tag{4.5}$$

where σ_j^α is the Pauli operator acting over the j-th spin with $j = 1, ..., N$, in the direction $\alpha = x, y, z$. J stands for the coupling between nearest-neighbor spins and B is the coupling between a spin and the transverse field. Depending on the sign of J the model is ferromagnetic ($J < 0$) or antiferromagnetic ($J > 0$). In order to reproduce this interaction in superconducting circuits, we make use of a high-fidelity set of gates, as introduced in Eq. (4.4): single-qubit rotations along the x direction, $X_j(\phi) = \exp(-i\phi\sigma_j^x)$, and two-qubit ZZ gates, $ZZ_{jk}(\theta) = \exp(-i\theta\sigma_j^z\sigma_k^z)$.

As shown in Section 4.2, it is possible to decompose a complex interaction into discrete series of gates through a Trotter expansion. In order to implement the spin-spin interaction, we need to execute $(N-1)$ two-qubit gates. In this case, there is no digital error because all the gates in this decomposition commute,

$$\exp\left(-i\ \theta \sum_{\langle jk \rangle} \sigma_j^z \sigma_k^z\right) = e^{-i\theta\sigma_1^z\sigma_2^z}\ e^{-i\theta\sigma_2^z\sigma_3^z}\ \cdots\ e^{-i\theta\sigma_{N-1}^z\sigma_N^z}, \tag{4.6}$$

with $\theta = Jt$, t being the simulation time of the experiment.The coupling among the spins and the transverse field can be simulated in a similar way using N single qubit

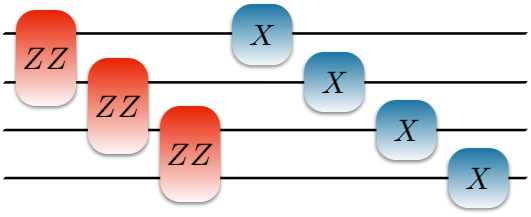

FIGURE 4.2: Protocol for digital quantum simulation of the Ising model with transverse magnetic field in terms of ZZ two-qubit gates and single qubit rotations along x axis.

rotations,

$$\exp\left(-i\ \phi \sum_j \sigma_j^x\right) = e^{-i\phi\sigma_1^x}\ e^{-i\phi\sigma_2^x}\ \cdots\ e^{-i\phi\sigma_N^x}, \tag{4.7}$$

with $\phi = Bt$. Given that the two interactions in Eqs. (4.6) and (4.7) do not commute, one has to implement them in sequential short-time Trotter steps to minimize the digital error. In Fig. 4.2, we show a scheme of the protocol for the quantum simulation of the transverse field Ising model for four spins. The recent achievement of high-fidelity single and two-qubit (CZ) gates with superconducting circuits will allow one to perform many Trotter steps for several qubits, using hundreds of gates.

In order to reduce the digital error, it is necessary to increase the number of Trotter steps. In Fig. 4.3, we plot a numerical simulation of the Ising model with transverse field for different digital steps. The simulated dynamics with digital decomposition is more accurate when compared with the exact dynamics when the number of Trotter steps is increased.

4.3.2 Spin Chain Coupled to a Bosonic Field Mode via Tavis-Cummings Model

We now analyze a model consisting of a spin-chain with nearest-neighbour couplings interacting with a bosonic mode. In this sense, both free energies of the bosonic mode and spins are taken into account, as well as spin-spin and spin-boson interactions. The spin-spin evolution is modelled with the Ising dynamics, while the Tavis-Cummings model describes the interactions between spins and bosons. The

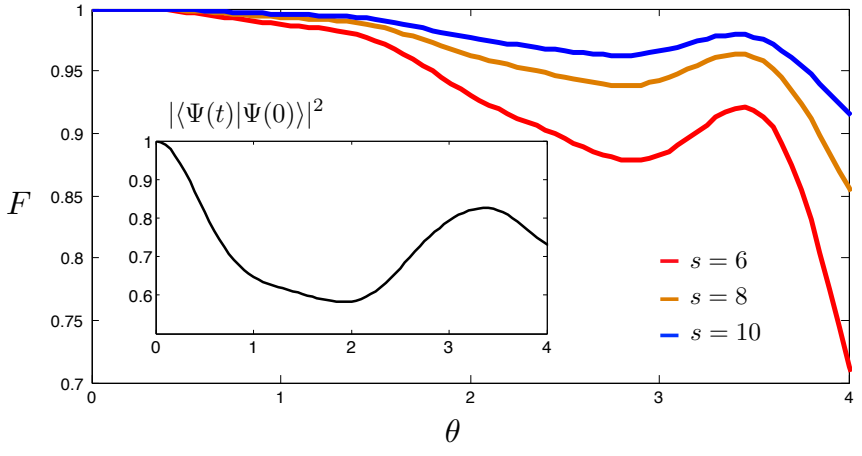

FIGURE 4.3: Digital simulation of the ferromagnetic Ising model with a transverse field for four spins in superconducting circuits, up to a phase of $\theta = 4$, with $J/B = 2$. The plot shows the fidelity of the digitally evolved state versus the ideally evolved one for different number of Trotter steps, $s = 6, 8, 10$. The inset shows the overlap between the ideally evolved state with the initial state, that is, all qubits in $|0\rangle_z$.

resulting Hamiltonian is

$$H_{ITC} = \omega\ a^\dagger a + \sum_j \frac{\Omega}{2}\sigma_j^z - J\sum_{\langle jk\rangle}\sigma_j^z\sigma_k^z + g\sum_j (a\sigma_j^+ + a^\dagger\sigma_j^-). \tag{4.8}$$

Following the notation presented above, σ_j^z is the Pauli operator along z direction, $\sigma_j^+(\sigma_j^-)$ is the creation(annihilation) spin excitation operator acting on the i-th spin and $a(a^\dagger)$ is the annihilation(creation) operator of the bosonic mode. ω and Ω are the free energies of each boson and spin, respectively. Moreover, J is the coupling constant between nearest spins and g stands for the coupling among spins and bosonic field.

The implementation in circuit QED requires the simulation not only of the spin dynamics, as in the previous example, but also of the bosonic mode. To achieve this, the superconducting qubits play the role of spins while the photons in a transmission line resonator emulate the bosonic excitations in the simulation. In order to perform the interactions of the model, it is necessary to couple the resonator to all the superconducting qubits. The Tavis-Cummings interaction appears straightforwardly in

circuit QED setups once the rotating wave approximation is performed,

$$H_1 = \omega_1 \; a^\dagger a + \sum_j \frac{\Omega_1}{2}\sigma_j^z + g\sum_j (a\sigma_j^+ + a^\dagger \sigma_j^-), \tag{4.9}$$

being ω_1 the frequency of the photons in the resonator, Ω_1 the frequency associated with the excitation energy of the superconducting qubits, and g the qubit-resonator coupling constant. The spin-spin interaction for qubits j and k is achieved by means of the ZZ gate presented in Eq. (4.4). Detuning to high frequencies the qubit-resonator interaction, we are able to reproduce the model

$$H(j,k) = \omega' \; a^\dagger a + \sum_j \frac{\Omega'}{2}\sigma_j^z - J\sigma_j^z\sigma_k^z. \tag{4.10}$$

Since $[H(j,k), H(j',k')] = 0 \; \forall \; j, j', k, k'$, we can define and implement sequentially the interaction

$$H_2 = \sum_{\langle jk \rangle} H(j,k) = \omega_2 \; a^\dagger a + \sum_j \frac{\Omega_2}{2}\sigma_j^z - J\sum_{\langle jk \rangle} \sigma_j^z\sigma_k^z, \tag{4.11}$$

where $\omega_2 = (N-1)\omega'$, $\Omega_2 = (N-1)\Omega'$ and N the number of simulated spins, and it fulfills the condition $\exp(-itH_2) = \prod_{\langle jk \rangle} \exp(-itH(j,k))$, being t the execution time.

Summing the interactions H_1 and H_2, we recover the model we wanted to reproduce, H_{ITC}. Nevertheless, $[H_1, H_2] \neq 0$, so we need to employ the Trotter method in order to make the digital error decrease, as shown in Fig. 4.4. Moreover, for considering the resonator photonic leakage, we have calculated the evolution of the system making use of the master equation,

$$\dot{\rho} = -i[H_t, \rho] + \kappa L(a)\rho. \tag{4.12}$$

Here, $L(a)\rho = (2a\rho a^\dagger - a^\dagger a\rho - \rho a^\dagger a)/2$ is the Lindblad superoperator acting on a, κ is the decay rate of the resonator, and $H_t = \{H_1, H_2\}$ is the Hamiltonian that governs the evolution. Notice that we have considered a coherence time much longer for the qubits than for the resonator. In Fig. 4.5, we plot the steps for implementing the protocol for four spins interacting with a bosonic mode.

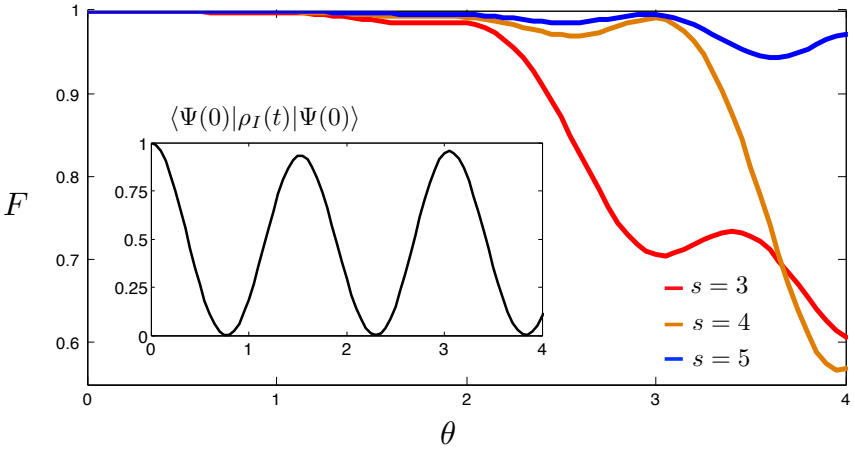

FIGURE 4.4: Fidelity F of the simulation of a four-spin chain coupled to a bosonic mode with circuit QED for different Trotter steps, $s = 3, 4, 5$. The upper curves correspond to larger number of Trotter steps. Here, the parameters of Hamiltonians H_1 and H_2 are $\omega_1 = 2\pi \times 200$ MHz, $\Omega_1 = 2\pi \times 180$ MHz, $g = 2\pi \times 80$ MHz, $\omega_2 = 2\pi \times 600$ MHz, $\Omega_2 = 2\pi \times 18$ MHz, $J = 2\pi \times 200$ MHz and the decay rate of the resonator is given by $\kappa = 2\pi \times 10$ kHz. F is defined as the overlap between the ideally evolved density matrix and the digitally evolved one, $F(t) = \mathrm{Tr}(\rho_I(t)\rho_T(t))$. The inset shows the overlap between the ideally evolved density matrix and the state of the system at $t = 0$, $1/\sqrt{2}(a^\dagger + (a^\dagger)^2/\sqrt{2})|0\rangle_p \otimes |1_1 0_2 0_3 0_4\rangle_z$, i.e., the same probability for having 1 and 2 photons in the resonator and all the superconducting qubits in the ground state of σ_i^z except the first, which is excited.

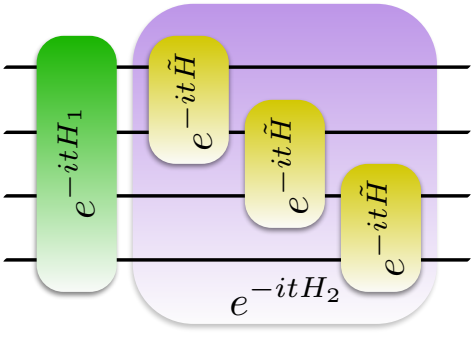

FIGURE 4.5: Protocol for the digital quantum simulation of a spin-chain coupled to a bosonic mode with superconducting circuits, in terms of unitary evolutions of Hamiltonians H_1, H_2 and $\tilde{H}$, being the interaction defined in Eq. (4.10).

4.3.3 Collective Spin Coupling Mediated by Resonators

In this subsection, we extend the Ising model presented in Eq. (4.5) by adding three-body interactions. The method can be generalized to arbitrary interaction orders. This extension allows us to simulate problems such as quantum chemistry [81, 123, 132, 133], as well as fermionic lattice models [82, 134], by using the Jordan-Wigner mapping to map fermionic interactions into spin interactions. The Hamiltonian for N spins including three-body interactions can be written as

$$H = J\sum_{\langle jk\rangle}\sigma_j^z\sigma_k^z + G\sum_{\langle jkl\rangle}\sigma_j^z\sigma_k^z\sigma_l^z + B\sum_j\sigma_j^x, \tag{4.13}$$

Here, we have added one collective interaction term with coupling constant G, which is the coupling among three nearest neighbour spins. This model can be simulated by enriching with additional gates the protocol for the Ising model in section 4.3.1. That is, together with single-qubit rotations along the x direction, $X_j(\phi) = \exp(-i\phi\sigma_j^x)$, and two-qubit zz gates, $ZZ_{jk}(\theta) = \exp(-i\theta\sigma_j^z\sigma_k^z)$, we also consider the combination of collective gates shown in Fig. 4.6. This will allow us to couple three qubits, $ZZZ_{jkl}(\beta) = \exp(-i\beta\sigma_j^z\sigma_k^z\sigma_k^z)$.

The collective spin interaction of this model can be decomposed into $(N-1)$ two-qubit gates and $2(N-2)$ three-qubit gates, and the transverse field is mimicked by N single qubit rotations. Moreover, we notice that the digital error of the Trotter expansion in Eq. (4.1) is reduced due to the fact that the interaction summands of the Hamiltonian commute with each other. The Trotter expansion for this model reads

$$e^{-iHt} \simeq \left(e^{-i\ t/s\ J\sum_{\langle jk\rangle}\sigma_j^z\sigma_k^z}e^{-i\ t/s\ G\sum_{\langle jkl\rangle}\sigma_j^z\sigma_k^z\sigma_l^z}e^{-i\ t/s\ B\sum_j\sigma_j^x}\right)^s, \tag{4.14}$$

where

$$\exp\left(-i\theta\sum_{\langle jk\rangle}\sigma_j^z\sigma_k^z\right) = e^{-i\theta\sigma_1^z\sigma_2^z}\ e^{-i\theta\sigma_2^z\sigma_3^z}\ \cdots\ e^{-i\theta\sigma_{N-1}^z\sigma_N^z},$$
$$\exp\left(-i\beta\sum_{\langle jkl\rangle}\sigma_j^z\sigma_k^z\sigma_l^z\right) = e^{-i\beta\sigma_1^z\sigma_2^z\sigma_3^z}\ e^{-i\beta\sigma_2^z\sigma_3^z\sigma_4^z}\ \cdots\ e^{-i\beta\sigma_{N-2}^z\sigma_{N-1}^z\sigma_N^z},$$
$$\exp\left(-i\phi\sum_{j}\sigma_j^x\right) = e^{-i\phi\sigma_1^x}\ e^{-i\phi\sigma_2^x}\ \cdots\ e^{-i\phi\sigma_N^x}, \tag{4.15}$$

with $\theta = -Jt$, $\beta = Gt$ and $\phi = Bt$, t being the simulated execution time. The collective gate for three qubits can be decomposed into two-qubit gates, as in Fig. 4.6. Recently, the implementation of collective gates with a quantum bus has been proposed in superconducting circuits [130].

In Fig. 4.7, we plot a numerical simulation of the extended Ising model with higher-order terms and transverse field for several Trotter steps. The figure shows as in the previous examples how the simulated dynamics with digital methods becomes more accurate when compared with the exact one when the number of Trotter steps is increased.

4.4 Experimental Realization of Digitized Adiabatic Quantum Simulations

In this section, we combine the advantages of digitization and adiabatic evolutions by implementing digitized adiabatic quantum computing in a superconducting system. We study the experimental results obtained in the lab of Prof. John M. Martinis at Google/University of California, Santa Barbara, which tomographically probes the system during the digitized evolution and explore the scaling of errors with system size. We conclude by having the full system find the solution to random one-dimensional Ising problem instances with frustration as well as non-stoquastic problem Hamiltonians that involve more complex interactions. This digital quantum simulation [23–25, 135] of the adiabatic algorithm consists of up to nine qubits and

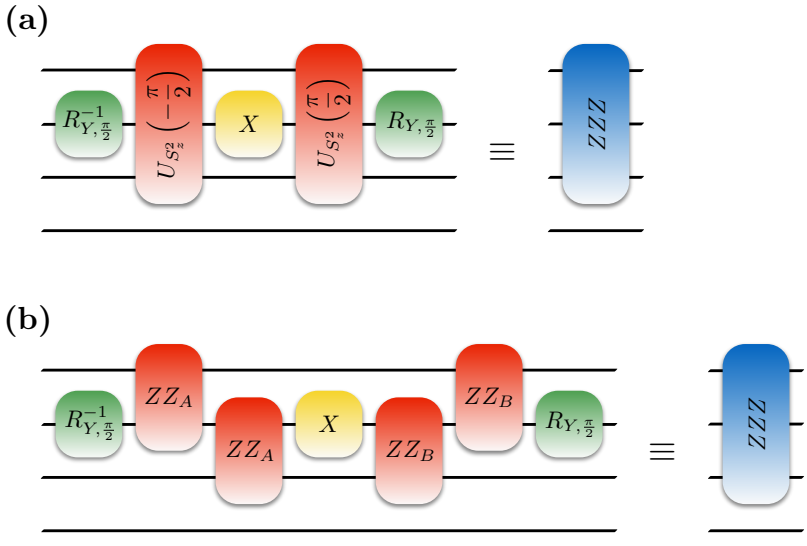

FIGURE 4.6: (a) Protocol for performing one of the three-qubit interactions appearing in Eq. (4.13) with collective gates. Here $ZZZ_{123}(\alpha) = \exp(-i\alpha\sigma^z_1\sigma^z_2\sigma^z_3)$, $R_{Y,\theta} = \exp(-i\theta\sigma^y/2)$ is the rotation along the Y-axis of a qubit, $X = \exp(i\alpha\sigma^x)$, and $U_{S^2_z}(\theta) = \exp(-i\theta/2\sum_{i<j}\sigma^z_i\sigma^z_j)$. (b) The same interaction ZZZ can be realized with two-qubit gates where $ZZ_A = \exp(i\pi\sigma^z \otimes \sigma^z/4)$, and $ZZ_B = \exp(-i\pi\sigma^z \otimes \sigma^z/4)$.

up to 10^3 quantum logic gates. The demonstration of digitized adiabatic quantum computing in the solid state opens a path to synthesizing long-range correlations and solving complex computational problems. When combined with fault-tolerance, this approach becomes a general-purpose algorithm that is scalable.

We explore the adiabatic quantum evolutions of one-dimensional spin chains with nearest-neighbour coupling. We start with a simple ferromagnetic problem to visualize the adiabatic evolution process. We identify specific error contributions, and follow up by exploring the scaling of errors with system size. We finish by testing the device on random stoquastic and non-stoquastic problems. The initial and problem

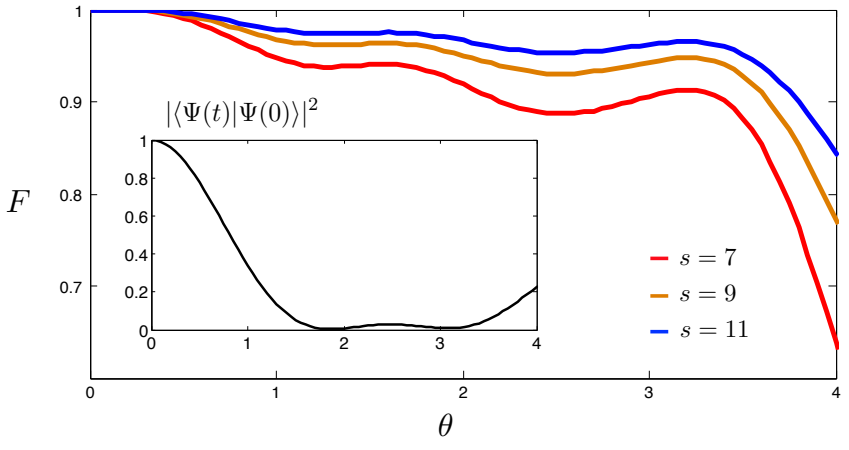

FIGURE 4.7: Digital simulation of the extended Ising model with a transverse field and three-body terms for four spins in superconducting circuits, where $J = G = 2\pi \times 400$ MHz and $B = 2\pi \times 200$ MHz, for a phase of $\theta \equiv -Jt = 4$. The plot shows the fidelity of the digitally evolved state with the ideally evolved one for different Trotter steps, $s = 7, 9, 11$. The inset shows the overlap between the ideally evolved state with the initial state, that is, all qubits in $|0\rangle_z$ state.

Hamiltonians are

$$H_I = -B_I^x \sum_i \sigma_i^x, \tag{4.16}$$

$$H_P = -\sum_i (B_i^z \sigma_i^z + B_i^x \sigma_i^x) - \sum_i \left(J_i^{zz} \sigma_i^z \sigma_{i+1}^z + J_i^{xx} \sigma_i^x \sigma_{i+1}^x\right), \tag{4.17}$$

where B^z and B^x denote local field strengths, and J^{zz} and J^{xx} the $\sigma^z\sigma^z$ and $\sigma^x\sigma^x$ coupling strengths. The Ising model is recovered when $B^x = J^{xx} = 0$. We initialize the system with H_I and vary the system Hamiltonian to the final problem: $H(r) = rH_P + (1-r)H_I$, with r going from 0 to 1. An example problem is shown in Fig. 4.8a.

The spin system is formed by a superconducting circuit with nine qubits. The qubits are the cross-shaped structures [136], patterned out of an Al layer on top of a sapphire substrate, and arranged in a linear chain, see Fig. 4.8b. Each qubit is capacitively coupled to its nearest neighbours, and can be individually controlled and measured; for details see Ref. [137]. Crucially, by tuning the frequencies of the qubits we can implement a tunable controlled-phase entangling gate. We use the

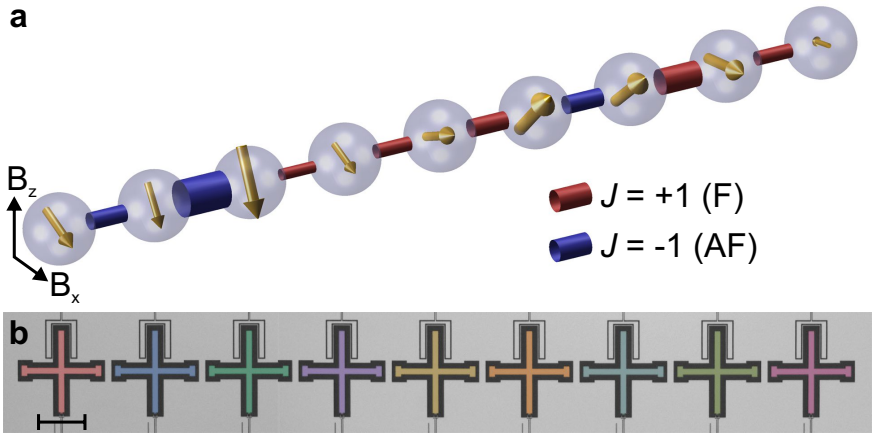

FIGURE 4.8: Spin chain problem and device. (a) We implement one-dimensional spin problems with variable local fields and couplings between adjacent spins. Shown is an example of a stoquastic problem Hamiltonian with local X and Z fields, indicated by the gold arrows in the spheres, and $\sigma^z\sigma^z$ couplings, whose strength is indicated by the radius of the links. Red denotes a ferromagnetic and blue an antiferromagnetic link. The problem Hamiltonian is for the instance in Fig. 4.11c. (b) Optical picture of the superconducting quantum device with nine Xmon qubits Q_0 - Q_8 (false-coloured cross-shaped structures), made from Al (light) on a sapphire substrate (dark). Connections to readout resonators are at the top, and control wiring is at the bottom. Scale bar is 200 μm.

first-order Trotter expansion to digitize [21]. The evolution is divided into many steps, see Appendix B.

For quantifying digitized adiabatic evolutions there are four sets of data: I) The ideal continuous time evolution, for infinite time, which is free of error and provides the perfect solution; we refer to this as "target state". II) The ideal continuous time evolution for a finite time T, which is sensitive to non-adiabatic errors. We call these results: "ideal continuous evolution". III) The "ideal digital evolution", where the finite ideal continuous evolution is digitized, and therefore includes digital error as well as non-adiabatic errors. And IV) the experimental results, which include a contribution from gate errors as well.

4.4.1 Ferromagnetic Chain

We start with a ferromagnetic chain problem with $N = 4$ spins, and equal coupling strength $J^{zz} = 2$. The qubits are initialized in the $|+\rangle^{\otimes N}$ state, and we use five steps to evolve the system to the problem Hamiltonian, performing quantum state tomography after each step. We linearly decrease the B^x term to zero, starting at $B^x = 2$, and simultaneously increase the coupling strength from 0 to 2, ending the evolution at a scaled time of $|J|T = 6$. The density matrices are shown in Fig. 4.9a. With each step the quantum state evolves and matrix elements in the middle vanish while the elements at the four corners grow to form the density matrix ρ of the Greenberger-Horne-Zeilinger (GHZ) state, the solution to the ferromagnetic problem, with a fidelity $\mathrm{Tr}(\rho_{\mathrm{target-state}}\rho)$ of 0.55. The density matrix is constrained to be physical [17]. The ideal digital evolution is plotted in Fig. 4.9b, reaching a fidelity of 0.85. The Hamiltonian during evolution, construction of the algorithm, and pulse sequence are shown in Figs. 4.9c-e. In each Trotter step, we perform a $\sigma_z\sigma_z$ operation on each pair, to implement the ferromagnetic $\sigma_z\sigma_z$ coupling, followed by single qubit rotations around the X axis to simulate the transversal magnetic field. In the pulse sequence, the rectangular-like frequency detuning pulses indicate where $\sigma_z\sigma_z$ interaction is implemented by bringing qubits near resonance (highlighted for $s = 0.2$). The wave-like pulses are microwave gates. The decrease in B_x is reflected by the reduction in amplitudes of the corresponding pulses (highlighted for $s = 0.4$ and $s = 1.0$). Additional microwave echo pulses decrease coupling to other qubits and the environment. We find mean phase errors from neighbouring parasitic interactions to be around 0.05 rad, equivalent to an error contribution below 10^{-3}, see Appendix B.

The experiment in Fig. 4.9 shows that digital synthesis of adiabatic evolutions can successfully be implemented in a solid state quantum platform. Using five Trotter steps, 15 entangling gates and 144 single-qubit microwave gates, the system produces a GHZ state with a fidelity that indicates genuine entanglement. It shows that complex pulse sequences are possible, and that the errors make sense: The fidelity of the experimental data with respect to the ideal digital evolution is 0.64. The overlap between the ideal digital evolution and ideal continuous time evolution for finite time is 0.93, and the overlap of this continuous evolution with the GHZ state (see Appendix B) is 0.88. The product of the above three values (0.52) is close to the experimental fidelity of 0.55, and shows the experimental error is a combination

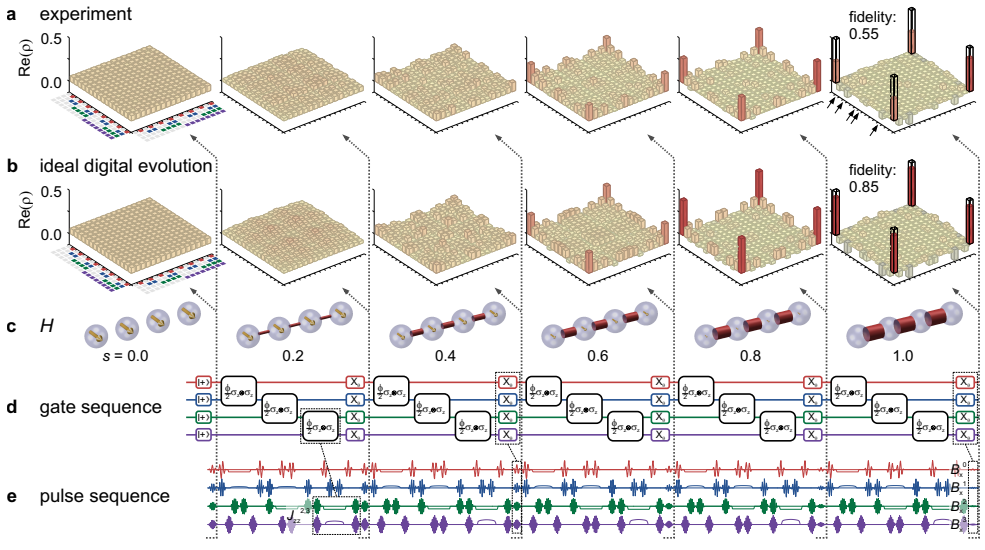

FIGURE 4.9: Quantum state tomography of the digital evolution into a Greenberger-Horne-Zeilinger state. A four-qubit system is adiabatically evolved from an initial Hamiltonian where all spins are aligned along the X axis to a problem Hamiltonian with equal ferromagnetic couplings between adjacent qubits ($J_{zz} = 2$). (a) Experimental density matrix ρ at the start and after each Trotter step, showing the growth of the major elements on the four corners, measured using quantum state tomography. The target state is shown in black. Coloured squares indicate qubit indices: For example, Q_0 being excited is indicated by a red square. Black arrows indicate significant elements for states which differ from the target state by a single kink. (b) Ideal digitized evolution, showing major elements on the four corners as well as other populations and correlations. Real parts shown. (c) Hamiltonian at different r, showing the vanishing transversal field and increasing coupling strength. (d) Gate sequence, showing initialization and the five Trotter steps. (e) Pulse sequence, showing the single-qubit microwave gates (wave-like pulses) and frequency detuning pulses (rectangular-like). Corresponding interactions and local field terms are highlighted. The displayed five step algorithm is 2.1 μs long. Colours correspond to the physical qubits in Fig. 4.8b. Implementations of $\sigma^z\sigma^z$ coupling and local X-fields are highlighted. See Appendix B for imaginary parts and the ideal continuous evolution.

of non-adiabatic, digitization and gate errors. Adopting the entangling gate error of $7.4 \cdot 10^{-3}$ and $8 \cdot 10^{-4}$ as measured in Ref. [17], we expect an accumulated gate error of 0.23 whereas we find an infidelity of 0.36; we attribute the difference to errors in maintaining the phases of the four-qubit system for a duration of 2.1 μs.

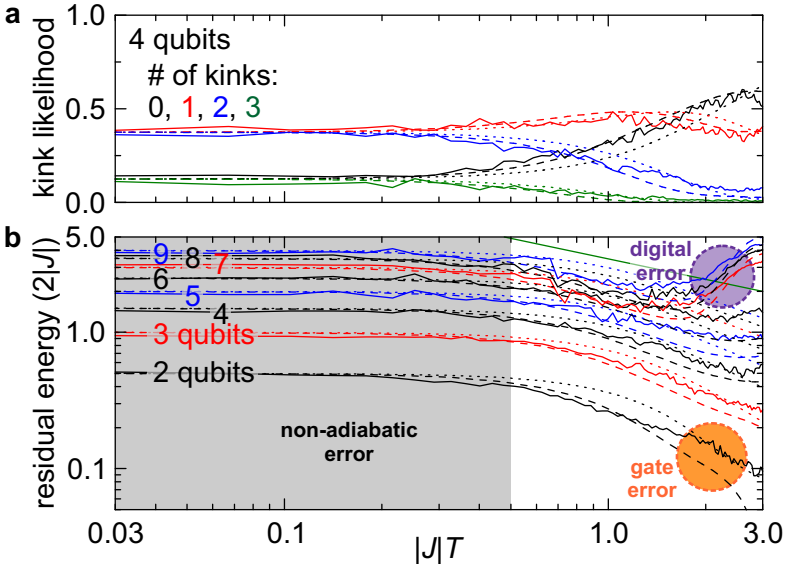

FIGURE 4.10: Kink errors, residual energy, and scaling with system size. (a) Kink likelihood for the four-qubit configuration. Solid lines: experiment. Dashed lines: ideal digital evolution. Dotted lines: ideal continuous time evolution. (b) Residual energy in the adiabatic evolutions of ferromagnetic chains ($J_{zz} = 2$) in configurations with two to nine qubits. The green solid line shows the ideal square-root trend for the large-scale limit (see Appendix B). Distinct contributions to error are highlighted.

An important feature of the errors is the prevalence of populations and correlations of the $|\downarrow\downarrow\downarrow\uparrow\rangle$, $|\downarrow\downarrow\uparrow\rangle$, and $|\downarrow\uparrow\uparrow\uparrow\rangle$-states and their bitwise inverse, see arrows in Fig. 4.9a. Their elements are also present in the ideal digital results as well as the ideal continuous evolutions (see Appendix B). These are states that deviate by a single kink from the target state, having a residual energy of $2|J|$, indicating the presence of non-adiabatic errors. These kink errors are connected to the formation of defects during a phase transition, as described by the Kibble-Zurek mechanism [138].

To explore the scaling of errors we vary the system size from two to nine qubits and measure the likelihood of kinks and residual energy. We keep the ferromagnetic problem Hamiltonian, $J_{zz} = 2$, but vary the scaled time such that $|J|T$ goes from 0 to 3. For the two to six qubit system we use five Trotter steps and for seven to nine qubits we use two steps, to limit the total number of gates. The kink likelihood for

the four-qubit system is shown in Fig. 4.10a. Here, the likelihood of one kink is given by the sum of the probabilities of all states with one kink. When increasing $|J|T$ from 0 to 3 the kink likelihood decreases, and the likelihood of no kinks increases (black line). The experimental data closely follow the ideal digital evolution (dashed). This picture is repeated for all systems, see Appendix B.

The kink likelihood signals that the final state has residual energy, as a state with a single kink has energy $2|J|$ above the target state. The residual energies for all systems are plotted in Fig. 4.10b. Initially, the residual energy is constant at $|J|T \sim 0$, and starts to decrease around $|J|T \sim 0.5$, following both the ideal digital (dashed) and ideal continuous time evolutions (dotted). For two to six qubits, this decrease continues until the traces start to settle around $|J|T = 3$. For the seven to nine qubit system, the residual energy starts to increase again around $|J|T = 2$, following the ideal digital evolution. See Appendix B for the pulse sequence for the nine qubit experiment, all kink likelihoods, and for the differences between the residual energies.

The main result is that Fig. 4.10 distinctly shows the different contributions to error (highlighted): For $|J|T \ll 1$, the residual energy is dominated by non-adiabatic errors as the evolution moves too fast. For $|J|T > 2$, the flattening out of the residual energy for the configurations with two to six qubits indicates that gate errors dominate, as the predictions from the ideal digital evolutions are significantly lower. And for the larger qubit configurations with seven to nine qubits, the residual energy follows the digital predictions upwards, indicating that digitization errors dominate. In addition, the residual energy visibly decreases at $|J|T = 1$ for all configurations, implying that the digitized evolutions are able to approach the target state even for nine qubits.

We also applied local fields to explore the lifting of degeneracy and generation of long-range correlations, see Appendix B.

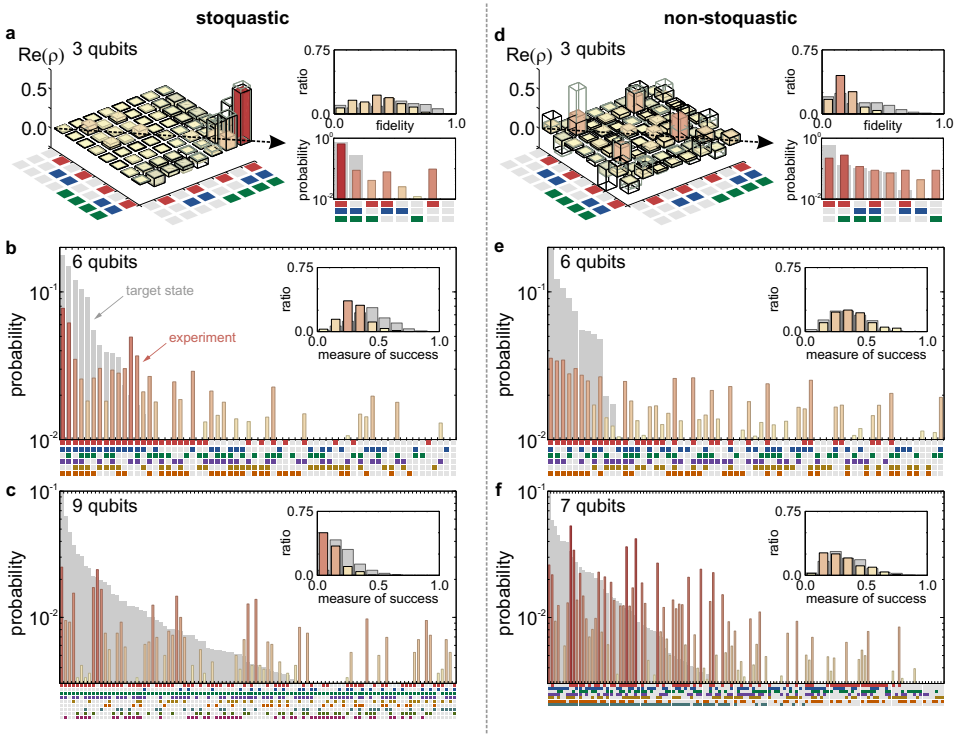

FIGURE 4.11: Digital evolutions of random stoquastic and non-stoquastic problems. As stoquastic problems we use frustrated Ising Hamiltonians, having random local X and Z fields, and random $\sigma_z\sigma_z$ couplings. (a, b, c) Stoquastic results are shown for three, six and nine qubits. For three qubits we have done tomography. An example instance is on the left in (a), where we show the real part of the density matrix. Coloured bars denote the experimental data, black the ideal digital evolution, and gray the target state. The diagonals of the experiment (colour) and the target state (gray) are on the right, rank ordered by ideal target state results. The fidelity results for all 100 instances are summarized in the histogram where ratio denotes the normalized occurrence, top right. Coloured bars: fidelities of experimental results with respect to the target state. Gray: fidelities of the ideal digital evolution with respect to the target state. The correlated probabilities for six (b) and nine (c) qubits are plotted in the main figure, sorted by target state results. Experimental data is in colour, the target state is in gray. The results for all 250 instances are summarized in the insets. For the nine qubit instance the first 100 elements are shown. (d, e, f) Non-stoquastic problems have additional random $\sigma_x\sigma_x$ couplings, here we plot the data for three, six, and seven qubits, for which the average measure of success is above the random baseline. The results show that the system can find the ground states of both stoquastic and non-stoquastic Hamiltonians with a similar performance.

4.4.2 Simulation of Stoquastic and Non-Stoquastic Hamiltonians

We next discuss how the digitized approach can solve both stoquastic and non-stoquastic problems with comparable performance, by testing random problems on three, six, seven, eight and nine qubits. Problems have local fields and couplings with random strength and sign. We independently choose B_z and B_x from [-2, 2] for each spin, and J_{zz} from [-2, -0.5] or [0.5, 2] for each link. This creates a random Ising problem with frustration. For non-stoquastic problems we also add J_{xx} coupling for each link, with values from [-2, -0.5] or [0.5, 2]; effectively doubling the amount of entangling gates. We avoid small couplings to reduce the number of gates. For the three qubit systems we have used quantum state tomography on 100 separate instances, to include off-diagonal elements in the fidelity metrics. For six or more qubits, tomography is not practical and we have measured the correlated probabilities on 250 separate instances, and use a measure of success that is equal to $|\langle\Psi_{\text{ideal}}|\Psi\rangle|^2$ to first order and sets an upper bound on the fidelity: $(\sum_k \sqrt{P_{k,\text{ideal}} P_k})^2$, where $P_{k,\text{ideal}}$ and P_k are probabilities and k runs over the computational basis. In Fig. 4.11 we show the results for stoquastic problems with three, six and nine spins, and non-stoquastic problems with three, six and seven spins. Per case, we highlight a single instance and show histograms of the fidelities.

For the three-spin stoquastic problems, the real part of the density matrix of one instance and a histogram of its diagonal elements are shown in Fig. 4.11a. In the tomography plot we overlay the experimental results (colour) with the ideal digital (black), and ideal continuous results (gray). For this example, we find fidelities $\text{Tr}(\rho_{\text{ideal}-\text{digital}}\rho) = 0.70$ and $\text{Tr}(\rho_{\text{target}-\text{state}}\rho) = 0.63$. In the top right, we show in colour the histograms for all instances of the fidelities $\text{Tr}(\rho_{\text{target}-\text{state}}\rho)$. Shown in gray is the fidelity of the ideal digital evolution with respect to the target state. Stoquastic problems with six and nine qubits are displayed in Figs. 4.11b-c. The main figures show the measured probabilities (colour) sorted by the target state results (gray), and the insets display the histograms. Non-stoquastic problem results are displayed on the right in Figs. 4.11d-f.

The key result from Figs. 4.11 is that the physical system can find solutions to non-stoquastic problems with a performance similar to that of stoquastic problems.

The three qubit examples show major diagonal as well as off-diagonal elements close to the expected positions. And visibly, for six and more qubit systems the coloured bars in the example instances are mostly on the left, indicating that the system has a clear preference for returning the probabilities associated with the ideal solutions.

The physical system produces results which are comparable to the expectations, as the histograms show a significant overlap between experiment and theory. Moreover, the numbers are consistent, as we now discuss the six qubit stoquastic example. The mean success rate between the ideal adiabatic evolution and target state is 0.59 ± 0.01, indicating that the scaled time is large enough for capturing the evolution dynamics. The mean success rate of the ideal digitized evolution with respect to the ideal adiabatic evolution is 0.73 ± 0.01, indicating a proper Trotterization of the evolution. Finally, the value for the experimental evolution with respect to the ideal digitized evolution is 0.714 ± 0.006, indicating that the experiment follows the ideal digital evolution reasonably well. Interestingly the product of the above three numbers, 0.31, is very close to the mean value between the experimental data and the target state, 0.296 ± 0.007. This shows that the experimental errors arise from comparable contributions of non-adiabatic, digital, and gate errors. For the six qubit non-stoquastic case, experimental-to-target state values are higher than this product, suggesting that errors partially cancel. A further reason may be that the presence of $\sigma_x\sigma_x$ terms is helpful for difficult problems in general [122]. This experiment took up to nine qubits and up to 10^3 gates. See Appendix B for pulse sequences, gate counts, problem parameters, and additional metrics.

To further quantify the performance of the system we compare experimental as well as random probabilities with the theoretical results. In essence, we take a uniform random distribution over the 2^N possible measurement outputs as a baseline sanity check. We find that for the stoquastic problems, the measures of success of all six to nine qubit configurations are significantly above this baseline: for six qubits, the success measure of the experimental data with respect to the target state is 0.296 ± 0.007, while using uniform random probabilities produces a value of 0.168 ± 0.005. For the nine qubit case the numbers are: 0.122 ± 0.006 for the experimental data and 0.074 ± 0.004 for random. For the non-stoquastic problems the numbers are: 0.380 ± 0.009 and 0.335 ± 0.008 for the six qubit configuration, and

for the seven qubit case: 0.311 ± 0.009 and 0.277 ± 0.008. A complete listing for all configurations can be found in the Appendix B.

This experiment shows that digital synthesis of the adiabatic evolutions can be used to find signatures of the ground states of random stoquastic as well as non-stoquastic problems. Errors arise from a comparable contribution of non-adiabatic, digital, and gate errors; and success rates are significantly above a uniform random baseline. We note that for larger qubit systems the number of Trotter steps needs to be limited to reduce the accumulation of gate error; in turn limiting the evolution we can simulate. The experimental error is therefore larger, from a combination of gate, digitization, and non-adiabatic error. However, in an error-corrected system the number of gates is in principle unconstrained, digitization can be made arbitrarily accurate, and one can move slower through critical parts of the evolution. While we have used Trotterization [22], with recent methods based on the truncation of Taylor series [139] the scaling of the digitization becomes appealing. See Appendix B for further motivations and discussions.

4.5 Conclusions

In this Chapter, we have introduced digitized adiabatic quantum simulations. We have proposed the digital quantum simulation of several spin-chain models coupled to bosonic modes with circuit quantum electrodynamics architectures. We have presented a method for decomposing spin interactions and implementing them stepwisely with available single and two-qubit gates. Furthermore, we have considered both circuit QED setups employing capacitively coupled superconducting qubits and transmission line resonators acting as quantum buses. We have exemplified our method with the quantum simulation of the Ising model with transverse field, a spin chain coupled to a bosonic field mode, and a many-body spin model with three-body interactions, which are realized through a bosonic quantum bus. These results show that spin chains and bosonic field modes can be efficiently implemented with superconducting qubits.

Additionally, we have analyzed the theory and the experiment realized in Google/University of California, Santa Barbara, where the proposed digitized adiabatic quantum evolutions have been demonstrated in superconducting circuits. We believe that the digitized approach to adiabatic quantum evolutions of complex problems, where local fields, variable coupling strengths and types, as well as multibody interactions can be constructed, becomes viable on the small scale with lower gate errors, and that large scale applications can be done in conjunction with error correction. We hope our work accelerates the improvement of superconducting quantum systems, and motivates further research into the encoding of and measurement for non-stoquastic computational problems. In addition, we anticipate that these results encourage work on the efficient digitization of algorithms for small and large-scale systems, for which reducing the effects of noise is paramount.

Chapter 5

Genetic Algorithms for Digital Quantum Simulations

I believe that at the end of the century the use of words and general educated opinion will have altered so much that one will be able to speak of machines thinking without expecting to be contradicted.

Alan Turing

5.1 Introduction

Optimization problems, a prominent area in computer science and machine learning [62], are focused on finding, among all feasible solutions, the best one in terms of efficiency and resource requirements. In particular, genetic algorithms (GAs) [140], an especially flexible and robust set of optimization methods, are inspired by ideas of evolution and natural selection. In this sense, GAs optimize among different possibilities, which are codified in the genetic information of an individual. Evolution is therefore based on genetic recombination over a group of

individuals, together with some random mutations. Natural selection is performed according to the optimization criteria, codified in an evaluation or fitting function. This process is repeated until the individuals satisfy a condition of adaptation. As the solutions to the problem are encoded in the genetic information of the individuals, the information of the survival corresponds to the optimal solution.

A variety of applications have been designed utilizing these methods: mirrors that funnel sunlight into a solar collector [63], antennas measuring the magnetosphere of Earth from satellites [64], walking methods for computer figures [65] and efficient electrical circuit topology [66, 67]. The resilience against changes in the initial conditions of the problem is based on the overheads in the resources. For instance, in the case of electric circuits, when one circuit element fails, the circuit continues working and the designed antennas continue measuring signals even under changes in environmental conditions.

One of the most important limitations in the field of quantum computing [141] is the fidelity loss of quantum operations. Quantum error correction protocols [13, 14], which codify logical qubits in several physical qubits, have been proposed and implemented in different quantum technologies, such as linear optics [15], trapped ions [16] and superconducting circuits [17, 18]. It is noteworthy to mention that quantum error correction has been proposed for gate-based quantum computing [1] and, in principle, they are also meant to be adaptable to digital quantum simulations [19]. However, experimental implementations of quantum error correction protocols applied to specific quantum algorithms are still to come in the expected development of quantum technologies.

In this Chapter, we propose a protocol based on genetic algorithms for the suppression of errors ocurring within digital quantum simulations, along the general lines of bioinspired algorithms in quantum biomimetics [142, 143]. First, we prove that GAs are able to decompose any given unitary operation in a discrete sequence of gates inherently associated to the experimental setup. Moreover, we numerically demonstrate that this sequence achieves higher fidelities than previous digital protocols based on Trotter-Suzuki methods [19, 21]. Second, we show that GAs can be used to correct experimental errors of quantum gates. Indeed, architectures combining a sequence of imperfect quantum gates with ancillary qubits generate a modular

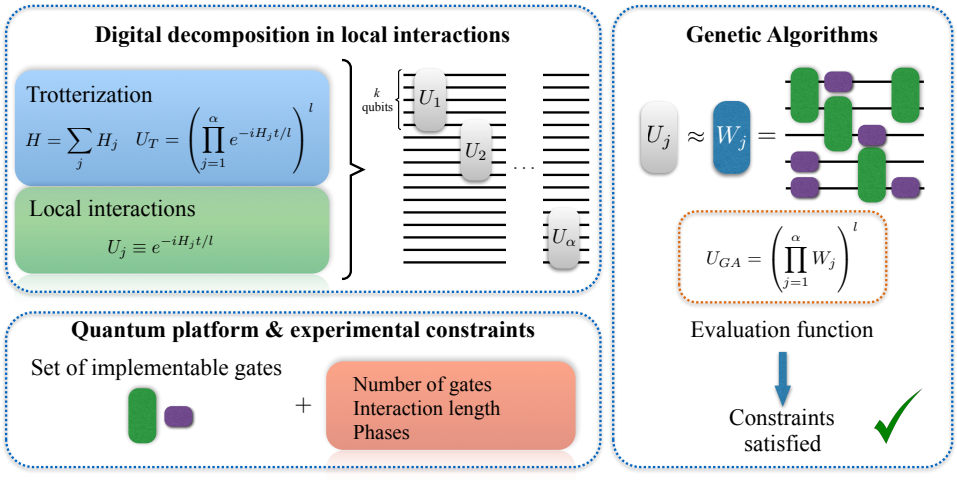

FIGURE 5.1: Scheme of the GA-based protocol for digital quantum simulations. First, the simulated Hamiltonian is decomposed in local interaction blocks, separately implemented in different unitary evolutions U_j which act on a subset of k particles of the system. Second, the set of gates is selected according to the constraints of the simulating quantum technology: total number of gates to avoid experimental gate error, interactions restricted to adjacent physical qubits, and implementable phases of the Hamiltonian, among others. Once the set of gates is determined, GAs provide a constraint-fulfilling sequence of gates, which effectively perform the resulting dynamics U_{GA} similar to U_T.

gate with higher fidelity than any of the components of the sequence. We exemplify this with a possible implementation of a high-fidelity controlled-NOT (CNOT) modular gate, which is made out of several imperfect CNOT gates. Additionally, these architectures show resilience against changes in the gate error. Therefore, by combining the concept of digital quantum simulation with GA, it is possible to design robust and versatile digital quantum protocols.

5.2 Digital Methods with Genetic Algorithms

Here, we explain how GAs can improve the fidelity of digital quantum simulations. Up to now, the standard technique for realizing digital simulations is Trotter-Suzuki expansion [21], which has been proven to be efficient [84, 104, 144]. This method consists in executing a series of discretized interactions, resulting in an effective

dynamics similar to the ideal dynamics of the simulated system. Associated to the unitary evolution of Hamiltonian $H = \sum_j^s H_j$, Trotter formula reads

$$U_I = e^{-iHt} = \lim_{l\to\infty} \left(e^{-iH_1 t/l} \cdots e^{-iH_s t/l} \right)^l , \tag{5.1}$$

where U_I is the ideal unitary evolution, t is the simulated time, l is the number of Trotter steps, and H_i are the Hamiltonians in the simulating system. On one hand, for a fixed total execution time, the larger the number of Trotter steps is, the lower the digital error of the simulation. On the other hand, the execution of multiple gates in a quantum system can introduce experimental errors due to decoherence and imperfect gate implementation. Therefore, there is a compromise between the number of Trotter steps and quantum operations that can be performed by the quantum simulator [94, 145].

GAs can be employed for outperforming current techniques of digital quantum simulations. The first step of a digital quantum simulation is the decomposition of the simulated Hamiltonian into interactions implementable in the quantum platform, which is a tough task in general. However, by using GAs, it is possible to find a series of gates adapted to the constraints imposed by the quantum simulator, whose resulting interaction is similar to the one of Hamiltonian H. For this purpose, we need neither to satisfy the condition $H = \sum_j^s H_j$, nor to use the same execution time for every involved gate. This not only relaxes the conditions for simulating the dynamics, but also allows us to control the number of gates involved, permitting the possibility of minimizing the experimental error.

Let us assume the situation in which is not possible to compute the ideal dynamics of a short-range interacting Hamiltonian, since, for instance the number of particles is too large. By using the Trotter-Suzuki formula, it is possible to decompose the interaction into α local blocks of k-interacting particles each, out of N total particles. Let us denote by U_j the ideal unitary evolution of the Hamiltonian acting on the jth local block of k qubits. Once the total dynamics is decomposed into blocks, each U_j has to be implemented employing the resources available in the experimental platform, as depicted in Fig. 5.1. Here, GAs play an important role,

since they provide an architecture for efficiently approximating each U_j by W_j:

$$U_T = \left(\prod_{j=1}^{\alpha} U_j\right)^l = \left(\prod_{j=1}^{\alpha} e^{-iH_j t/l}\right)^l, \tag{5.2}$$

$$U_{GA} = \left(\prod_{j=1}^{\alpha} W_j\right)^l, \tag{5.3}$$

where $\alpha = \left\lceil \frac{N-1}{k-1} \right\rceil$. We assume that k is sufficiently small to allow the minimization of the error associated with the approximation in a standard computer. Therefore, the evaluation function has access to an approximate version of the complete system dynamics, because this is solvable in terms of the Trotter expansion. In our algorithm, as an evaluation function, we compare Trotter unitary evolution, U_T, for a given number of Trotter steps l with the unitary evolution obtained from GAs, U_{GA}. The evaluation function is then given by $R_j = ||U_j - W_j||$. Notice that a global phase in the unitary W_j does affect the evolution but it affects the value of R_j, so we should consider $\inf_\phi ||U_j - e^{i\phi} W_j||$. As we normally have access to the initial state of the evolution, the evaluation function $R_j = |\langle\Psi|U_j^\dagger W_j|\Psi\rangle|^2$, in which the global phase is irrelevant, can be chosen. In addition, for all analyzed examples, the number of gates involved in the GA protocol is lower than in the Trotter expansion, which gives positive perspectives for experimental realizations of digital quantum simulations based on this approach.

The upper bound for the total error ξ of the protocol, is obtained by combining the Trotter error with the error of the GA optimization $\xi = ||U_I - U_{GA}|| \leq ||U_I - U_T|| + ||U_T - U_{GA}||$. The first term is nothing but the digital error [21], so we analyze the second term. Consider that W_j, the unitary provided by the GA, has a matrix error η_j, $W_j = U_j + \eta_j$. Let us denote by $\tilde{U_j} = \mathbb{1}^{\otimes j-1} \otimes U_j \otimes \mathbb{1}^{\otimes \alpha - j}$, the operations when extending to the whole Hilbert space, where α is the number of blocks. The same relation holds for $\tilde{W_j}$ and $\tilde{\eta_j}$, therefore, $\tilde{W_j} = \tilde{U_j} + \tilde{\eta_j}$. We are now able to compute the error of the GA optimization for a single Trotter step, given by $||U_T - U_{GA}|| = ||\prod \tilde{W_j} - \prod \tilde{U_j}|| = ||\prod(\tilde{U_j} + \tilde{\eta_j}) - \prod \tilde{U_j}||$. We approximate this expression to a first order in $\tilde{\eta_j}$, $||\sum \tilde{W}_1 ... \tilde{W}_{j-1} \tilde{\eta_j} \tilde{W}_{j+1} ... \tilde{W}_\alpha|| \leq$

$\sum ||\tilde{W}_1||...||\tilde{W}_{j-1}||||\tilde{\eta_j}||||\tilde{W}_{j+1}||...||\tilde{W}_\alpha||$. By computing the norm of the unitary matrices $\tilde{W}_j$, we obtain $\sum ||\tilde{\eta_j}||$, which coincides with the error in each of the subspaces, $||U_T - U_{GA}|| = \sum ||\eta_j||$. Therefore, the GA error is bounded by the sum of the errors in each unitary block, which is linear in the number of qubits for the simulation of a short-range interacting Hamiltonian. As a final remark, since both W and U are unitaries, we would like to point out that the error could also be parametrized by a multiplicative unitary matrix. However, both approaches are equivalent for small errors in the sense that $V_\mu = \exp(i\mu H) \approx 1 + i\mu H + O(\mu^2||H||^2)$ for a small μ, so $W \approx U + iUH\mu = U + \eta$.

We now illustrate the protocol for simulating digitally the isotropic Ising and Heisenberg spin models with a magnetic field in a superconducting circuit architecture as in Chapters 2 and 4 [24, 94, 114]. The Hamiltonians of these models are

$$H_{\rm I} = J\sum_{\langle i,j\rangle}^{N} \sigma_i^z\sigma_j^z + B\sum_{i}^{N}\sigma_i^x, \tag{5.4}$$

$$H_{\rm H} = J\sum_{\langle i,j\rangle}^{N} (\sigma_i^x\sigma_j^x + \sigma_i^y\sigma_j^y + \sigma_i^z\sigma_j^z) + B\sum_{i}^{N}\sigma_i^x, \tag{5.5}$$

where J is the coupling between nearest-neighbor spins $\langle i,j\rangle$, B is the strength of the magnetic field, and σ_i^γ are the Pauli operators acting on the ith spin with $\gamma = x, y, z$. We decompose the interactions in terms of single-qubit rotations and controlled-PHASE (CPHASE) gates between nearest-neighbor superconducting qubits [25, 26, 114, 146]. Following the approach in Chapter 4, simulating the Ising Hamiltonian requires $N-1$ CPHASE and $3N-2$ single-qubit gates, while Heisenberg Hamiltonian demands $3(N$-1) CPHASE and $11N-6$ single-qubit gates. In this simulation, we consider a chain of $N = 5$ spins. The GA computes a digitalized unitary evolution for a concrete time t, constituted by the previous gates in a local subspace of $k = 2$ qubits. Then, this unitary evolution W_1 is repeated following Eq. 5.3 with l=1 over all adjacent qubits due to the translation invariance . The resulting unitary process U_{GA} is compared with the ideal dynamics of the model. This protocol employs 4 CPHASE and 8 single-qubit gates for the Ising model, and 4 CPHASE and 16 single-qubit gates for the Heisenberg model. Moreover, fidelities are enhanced when compared with the corresponding to pure digital methods for a single Trotter step, even using less

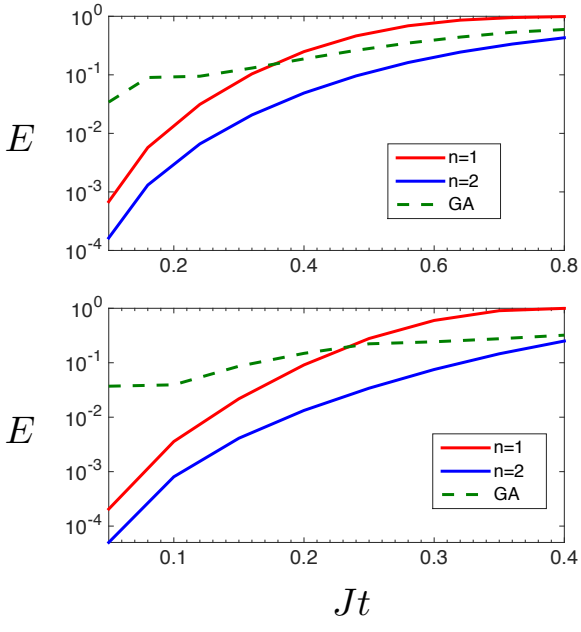

FIGURE 5.2: Logarithmic plot of the error $E = 1 - |\langle\Psi|U_I^\dagger \tilde{U}|\Psi\rangle|^2$ in the evolution of (a) Ising and (b) Heisenberg spin models for $N = 5$ qubits, $J = 2$, $B = 1$, and $|\Psi\rangle = |0\rangle^{\otimes 5}$. Here, U_I is the ideal unitary evolution, while $\tilde{U}$ refers to the unitary evolution using either a digital expansion in 1 (blue line) and 2 (red line) Trotter steps, or GAs (dashed green). The GA protocol requires fewer gates than the digital method for a single Trotter step achieving similar fidelities to two Trotter steps.

gates, as shown in Fig. 5.2. This approach can be applied similarly to other quantum technologies such as NV centers, trapped ions, and quantum dots among others, just by adding the constrains of their implementable quantum gates to the genetic algorithm. In this protocol, we have considered gates with perfect fidelity. Let us now focus on how to employ GAs to improve the experimental error of quantum gates.

5.3 Experimental Error in a CNOT Gate

Besides outperforming protocols for digital quantum simulations, GAs are also useful for suppressing experimental errors in gates. We propose a protocol to perform an

effective quantum gate by using ancillary qubits and a set of imperfect gates, and we illustrate for the CNOT gate. A CNOT gate is given by a unitary $U_{CNOT} = \exp(i\frac{\pi}{2}H_{CNOT})$, with $H_{CNOT} = \frac{1}{2}\left[(\mathbb{1}+\sigma^z)\otimes\mathbb{1} + (\mathbb{1}-\sigma^z)\otimes\sigma^x\right]$. Let us consider imperfect gates modeled by $W_{CNOT} = \exp(i\frac{\pi}{2}H_{CNOT} + \delta H_R)$, with $\delta << 1$ and H_R a random matrix, such that $||H||_2 = 1$. These unitaries define unital quantum channels $\mathbb{E}_U = U\otimes\bar{U}$ and $\mathbb{E}_W = W\otimes\bar{W}$ respectively, and we define the error of the gate as the distance $\eta = ||\mathbb{E}_W - \mathbb{E}_U||_2$.

Let us now consider $q-2$ ancillary qubits in the state $|0\rangle$ in addition to the control and target of the integrated CNOT gate. Let us also consider n imperfect CNOT gates $\vec{W} = \{W_1, \ldots, W_n\}$ acting on any possible pair of the q qubits, with errors $\vec{\eta} = \{\eta_1, \ldots, \eta_n\}$ respectively, and denoted by $\eta = \min_i \eta_i$. The integrated circuit is defined by a set of n ordered pairs $IG_{\vec{\eta}} = \{(i_k, j_k) | 1 \leq i_k, j_k \leq q, k = 1, \ldots, n\}$, where the indices indicate the control and target qubits, respectively. In order to calculate the fidelity of the protocol, we compute the Kraus operators of the integrated CNOT gate, by tracing out the $q-2$ ancillary qubits, and compare the resulting channel $\mathbb{E}_{IG_{\vec{\eta}}}$ with the unital channel $\mathbb{E}_U$, $\epsilon_{IG_{\vec{\eta}}} = ||\mathbb{E}_{IG_{\vec{\eta}}} - \mathbb{E}_U||_2$. If $\epsilon_{IG_{\vec{\eta}}} < \eta$, then the CNOT gate is implemented with higher fidelity than any of the original CNOT gates, showing this GA-based architecture resilience against quantum errors.

The set $IG_{\vec{\eta}}$ codifies the genetic information of the individuals which conform the population evolving into successive generations. During the reproduction, the individuals recombine their genetic code, which is also allowed to mutate. The survival probability depends on the fidelity of the effective CNOT encoded in $IG_{\vec{\eta}}$ and, therefore, only individuals associated with a small error succeed.

The number of possible architectures involving n different CNOT gates and q ancillary qubits is $P = (q^2-q)^n n!$, see Appendix C for a description of the genetic algorithm and a detailed calculation of the errors and number of architectures. The factor $(q^2-q)^n$ is due to all possible CNOT configurations in a given order between qubits i and j for n gates, while $n!$ comes from reordering imperfect gates $\{W_1, ..., W_n\}$. When q and n are small, the optimal architecture can be found by analyzing all cases. However, when we increase these parameters, this brute-force optimization method turns out to be inefficient. GAs allow us to optimize the protocol in this unreachable regime, being moreover robust, as analyzed below.

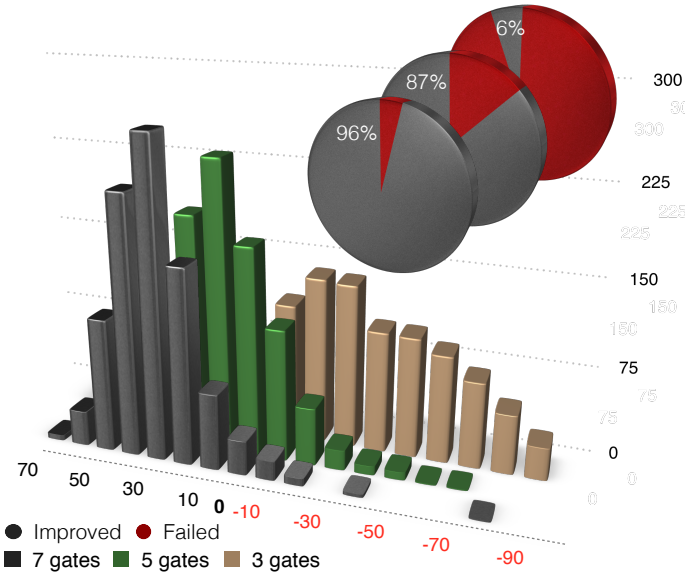

FIGURE 5.3: Error resilience for architectures with $n = 3, 5, 7$ imperfect CNOT gates using 1000 runs. Pie charts show the percentage of cases in which the fidelity of the effective CNOT overmatches the best CNOT employed in the architecture. Bar charts show the distribution of cases according to the relative improvement in the error, again when compared with the best CNOT.

This CNOT case has been analyzed involving three, five and seven gates. Notice that, when one considers $q = 4$ and $n = 7$, the number of possible architectures is larger than $1.8\times, 10^{14}$ for a fixed set of imperfect gates. We have chosen a set of gates and find the optimal architecture by GA. Then, we analyze the resilience or robustness of this architecture by changing the set. In Fig. 5.3, we have depicted the results for a sampling of 1000 sets of random imperfect CNOT gates. The pie charts show the percentage of cases with a lower error than any CNOT performed in the protocol, which are 6% for three qubits, 87% for five, and 96% for seven. Furthermore, the bar charts show the average improvement of the error for the integrated CNOT with respect to the best implementing CNOT, which is -39%, $+18\%$, and $+30\%$, respectively. For completeness, in Fig. 5.4, we show the optimal architecture for $q = 4$ and $n = 5$, obtained from a fixed set of imperfect gates $\vec{W}$, and proven to be robust, see Appendix C.

Additionally, we have studied the behavior of the protocol with respect to the

number of ancillary qubits. The results show no significant improvement when the number of performed gates is small, see Appendix C. For instance, architectures up to $n = 7$ do not overcome fidelities shown above when adding a third ancillary qubit, $q = 5$. However, we expect that architectures with a larger number of gates would actually take advantage of using more ancillary qubits in order to suppress the error.

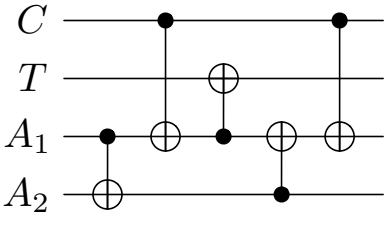

FIGURE 5.4: Scheme of the optimal architecture for constructing a CNOT gate with 5 imperfect gates, by using two ancillary qubits initialized in state $|0\rangle$. Here, C is the control, T is the target, and A_1 and A_2 are the ancillary qubits.

The same protocol can be applied in the realization of more general unitary operations. Additionally, the gates conforming the building blocks can be arbitrary, which facilitates the adaptation of the protocol to any experimental platform.

5.4 Conclusions

In summary, in this Chapter we have proposed a new paradigm based on GAs to enhance digital quantum simulations and face different types of quantum errors. We have shown that they can be used to improve the fidelity of quantum information protocols by effectively reducing digital errors produced in Trotter-Suzuki expansions. Our method has allowed us to correct experimental errors due to imperfect quantum gates, by using ancillary qubits and optimized architectures. We also argued that solutions provided by GAs manifest resilience against digital and experimental quantum errors. From a wide perspective, we expect that GAs will be part of the standard toolbox of quantum technologies, and a complementary approach to analog [147, 148] and digital [149] optimal-control techniques.

Chapter 6

Conclusions

If you're going to be a good and faithful judge, you have to resign yourself to the fact that you're not always going to like the conclusions you reach. If you like them all the time, you're probably doing something wrong.

Antonin Scalia

In this Thesis, we have explored several features of digital quantum simulations applied to spin models with superconducting architectures. We have studied the decomposition into quantum gates of complex spin Hamiltonians involving spin-spin and light-matter interactions. For this, we have considered not only purely digital protocols, but also digital-analog approaches, which allow us to efficiently simulate bosonic fields. Indeed, the simulation of these fields would otherwise require a large number of qubits and gates. Furthermore, we have shown that adiabatic quantum evolutions can be digitized, so that ground states of unnatural Hamiltonians are accessible with digital techniques. In addition, we have considered genetic algorithms for the decomposition of complex Hamiltonians into discretized gates, producing high-fidelity and robust solutions.

Along this work, we have analyzed the digitized implementation of spin interactions into superconducting-circuit-based technology. For this, we have studied different present superconducting architectures for the implementation of digital quantum simulations, such as transmission line resonators dispersively coupled to transmon qubits, which can be additionally capacitively coupled. We have shown that these systems provide the necessary complexity for digitally simulating a variety of spin models, including many-body and spin-boson interactions. Considering the state of the art technology, we have made realistic proposals taking into account gate-errors and decoherence processes, and we have analyzed the corresponding experimental realizations.

In Chapter 2, we have proposed the physical implementation in a circuit QED setup of two prototypical spin models, namely, Heisenberg and Ising models. By considering a set of superconducting qubits coupled via transmission line resonators operating as quantum buses, we have studied the use of implementable XY interactions and single qubit rotations for the simulation of the Heisenberg Hamiltonian. Indeed, our numerical simulations show that present superconducting circuit technology already provides the gate fidelities and coherence times required to successfully perform the quantum simulations. Taking into account realistic parameters, we have estimated the optimal number of Trotter steps to reach a balance between experimental gate errors and digital errors. In addition, we have described the experimental realization of this proposal, realized in the lab of Prof. Andreas Wallraff at ETH Zürich, in which XY, Heisenberg and Ising dynamics are physically implemented via two superconducting transmon qubits.

The digital-analog quantum simulation of the quantum Rabi model has been proposed in Chapter 3. Here, we have provided an approach to digitally simulate bosonic fields by implementing analog interaction blocks, instead of digitally decomposing it into single and two-qubit gates, which is much more efficient in terms of employed resources. Circuit QED systems provide naturally Jaynes-Cummings interactions. We have shown that also anti-Jaynes-Cummings interactions can be generated by introducing rotations before and after the former interaction. Employing the Trotter formula, we have proven that dynamics of the quantum Rabi model is achieved via the stepwise implementation of Jaynes-Cummings and anti-Jaynes-Cummings evolutions. Due to the flexibility of superconducting platforms, all quantum regimes

of the quantum Rabi model, namely, ultrastrong, deep-strong coupling regimes and Dirac equation in the limit, may be achieved by tuning the parameters in the setup. Moreover, this approach can be extended to the Dicke model by considering the Tavis-Cummings interaction as the building block in a setup with multiple qubits within a transmission line resonator. Recently, this proposal has been experimentally implemented in the lab of Prof. Leonardo Di Carlo at Delft University of Technology, where the quantum Rabi model is produced in an elaborate decomposition of more than 90 Trotter steps.

In Chapter 4, we have introduced the concept of digitized adiabatic quantum computing. By combining the approaches of adiabatic evolutions and digital simulations, we have shown that these quantum protocols allows for reaching the ground state of complex Hamiltonians that are not necessarily provided in a natural manner by the controllable quantum system. Here, we have considered capacitive couplings between superconducting qubits, as well as transmission line resonators playing the role of quantum buses. Exploiting the natural interactions provided by these systems, we have proposed the digital quantum simulation of the Ising model with transverse field, in which, differently to what was done in Chapter 2, qubit-qubit interactions come from the capacitive couplings. In addition, we have studied the use of resonators to implement bosonic fields in a Tavis-Cummings-like spin chain. Furthermore, we have exploited the ability of resonators to realize collective qubit interactions, which in general reduce the number of gates required in a purely digital protocol. Then, we have described the experimental realization of digitized adiabatic quantum evolutions of a spin chain in a 9-qubit superconducting chip in the lab of John M. Martinis at Google/University of California, Santa Barbara. Here, both stoquastic and non-stoquastic Hamiltonians, which are computationally hard problems, have been considered. These experiments, where up to 9 qubits and more than 1000 gates have been employed, show that digitized adiabatic protocols are feasible with current technology.

Finally, in Chapter 5, we have considered the problem of digitization of Hamiltonians from the perspective of machine learning. We have shown that genetic algorithms provide robust digital gate decompositions for quantum simulations. In fact, our results show that Ising and Heisenberg models can be reproduced in superconducting circuits using less gates than the required in Chapter 4. Furthermore, we

have considered genetic algorithms as a tool to improve the fidelity of composed gates with arbitrary errors, and we have demonstrated the efficiency of these methods in the construction of a CNOT gate with enhancements of up to 30% in the fidelity.

In summary, we believe that the results presented in this Thesis have contributed to the foundations of the field of digital quantum simulations in superconducting quantum platforms. Here, not only the first proposals to digitally simulate spin models are analyzed, but simulations of quantum field theories, fermionic models and quantum chemistry have also been proposed with a potential experimental impact. Indeed, the remaining experimental challenges are mainly the improvement in the control of circuit-based quantum architectures to provide not only long coherence times and high-fidelity gates, but also a higher flexibility in the implementation of interactions. In the near future, superconducting devices will hold up complex quantum information processes for large scale systems, in which quantum error correction codes will allow us to simulate intricate models like the physics of bio-chemical systems. Nevertheless, there are still relevant theoretical open questions, such as the development of a quantum error correction code in analog blocks, which hopefully will be addressed and solved in the near future to boost the burgeoning field of quantum technologies.

Appendices

Appendix A

Aspects of Experimental Simulation of Ising and Heisenberg Models

In this Appendix, we provide details of the experimental implementation of the digital quantum simulation of spin models with circuit QED, at ETH Zurich, studied in Chapter 2.

A.1 Chip Architecture and Measurement Setup

The present experiment was performed using two superconducting transmon [45] qubits Q1 and Q2 and one coplanar waveguide resonator R1 on a microchip (Fig. A.1). The resonator R1 has a fundamental resonance frequency of $\nu_r = 7.14$ GHz. From spectroscopic measurements we have determined the maximum transition frequencies $\nu_{\max} = \{5.55, 5.53\}$ GHz and charging energies $E_C/h \approx \{260, 260\}$ MHz of the qubits Q1 and Q2, respectively, where h is the Planck constant. The qubits Q1 and Q2 are coupled to resonator R1 with coupling strengths $g/2\pi \approx \{120, 120\}$ MHz. For this experiment the qubit transition frequencies in their idle state were offset

to $\nu = \{5.440, 5.240\}$ GHz by applying a constant magnetic flux threading their SQUID loops with miniature superconducting coils mounted underneath the chip. At these idle frequencies, the measured energy relaxation and coherence times were $T_1 = \{7.1, 6.7\}$ μs and $T_2 = \{5.4, 4.9\}$ μs, respectively. The transition frequencies of the qubits Q3 and Q4 were tuned to 4.5 GHz and 6.1 GHz such that they do not interact with Q1 and Q2 during the experiment.

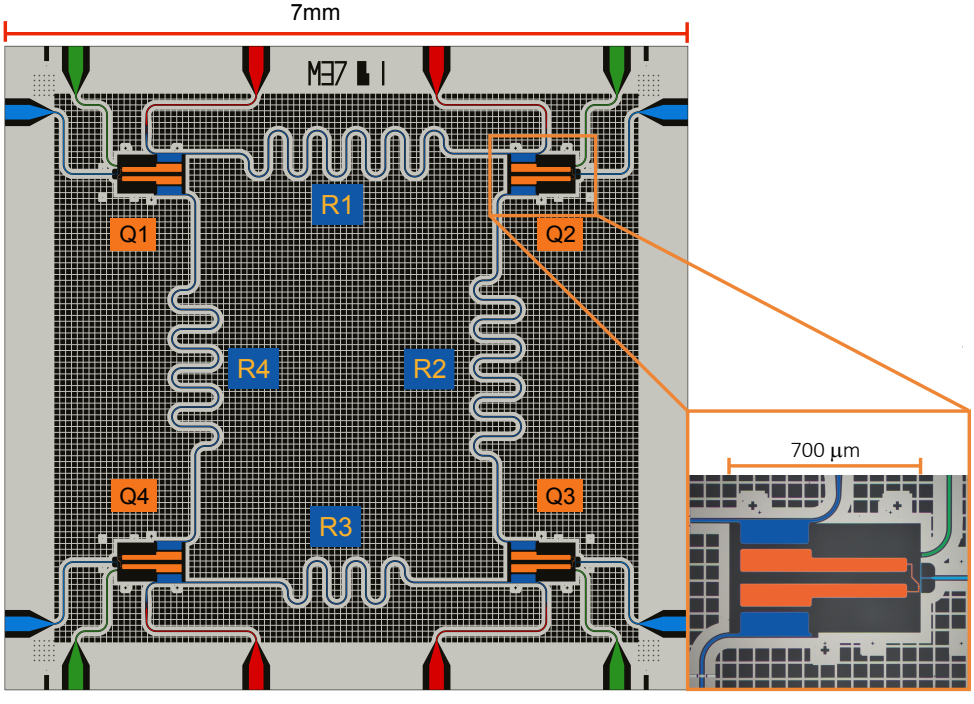

FIGURE A.1: Chip design and false colored optical image of a superconducting qubit (inset). The chip comprises four superconducting qubits Q1-4 (orange) made of aluminium and four niobium coplanar waveguide resonators R1-4 (deep blue) coupled to input and output ports (red). The qubits have individual microwave drive lines (green) and flux bias lines (blue).

A schematic diagram of the measurement setup is shown in Fig. A.2a. To realize two-qubit XY gates and single-qubit phase gates (Z), controlled voltage pulses generated by an arbitrary waveform generator (AWG) are used to tune the flux threading the SQUID loop of each qubit individually using flux bias lines [31]. The single-qubit microwave pulses (X,Y) are generated using sideband modulation of an

up-conversion in-phase quadrature (IQ) mixer (Fig. A.2b) driven by a local oscillator (LO) and modulated by an arbitrary waveform generator (AWG). The same up-conversion LO is used for the microwave pulses on both qubits to minimize the phase error introduced by phase drifts of microwave generators. We have used a quantum-limited parametric amplifier (PA) to amplify readout pulses at the output of R1 (Fig. A.2c). Here the Josephson junction based amplifier in form of a Josephson parametric dimer (JPD) [150] is pumped by a strong pump drive through a directional coupler (D). To cancel the pump leakage, a phase (ϕ) and amplitude (A) controlled microwave cancelation tone is coupled to the other port of the directional coupler (D). Three circulators (C1-3) were used to isolate the sample from the pump tone. A circulator (C4) at base temperature followed by a cavity band-pass filter (BP) and another circulator (C5) at the still stage were used to isolate the sample and JPD from higher-temperature noise. The transmitted signal is further amplified by a high electron mobility transistor (HEMT) at the 4.2 K stage and a chain of ultra-low-noise (ULN) and low-noise (LN) amplifiers at room temperature as shown in Fig. A.2d. The amplified readout pulse is down-converted to an intermediate frequency (IF) of 25 MHz using an IQ mixer (Fig. A.2e) and digitally processed by field-programmable gate array (FPGA) logic for real-time data analysis.

A.2 Implementation of the XY Gate

The interaction between two qubits with degenerate transition frequencies dispersively coupled to the same CPW resonator is described by the exchange coupling [37] $J(\sigma_1^+\sigma_2^- + \sigma_1^-\sigma_2^+)$ which can also be written in terms of Pauli operators as $\frac{J}{2}(\sigma_1^x\sigma_2^x + \sigma_1^y\sigma_2^y)$. We activate this interaction by tuning the transition frequency of qubit Q1 into resonance with qubit Q2 with a flux pulse (Fig. A.3) for an interaction time τ which we varied from 0 to 60 ns. At the frequency of qubit Q2, we obtain a coupling strength $J = -40.4$ MHz from a fit to the spectroscopically measured avoided crossing. To compensate overshoots of the flux pulse due to the limited bandwidth of the flux line channel, we use an inverted linear filter based on room-temperature response measurements of the flux line channel and in-situ Ramsey measurements of the residual detuning of qubit Q1 in the time interval from 0 to 2 μs after the flux pulse.

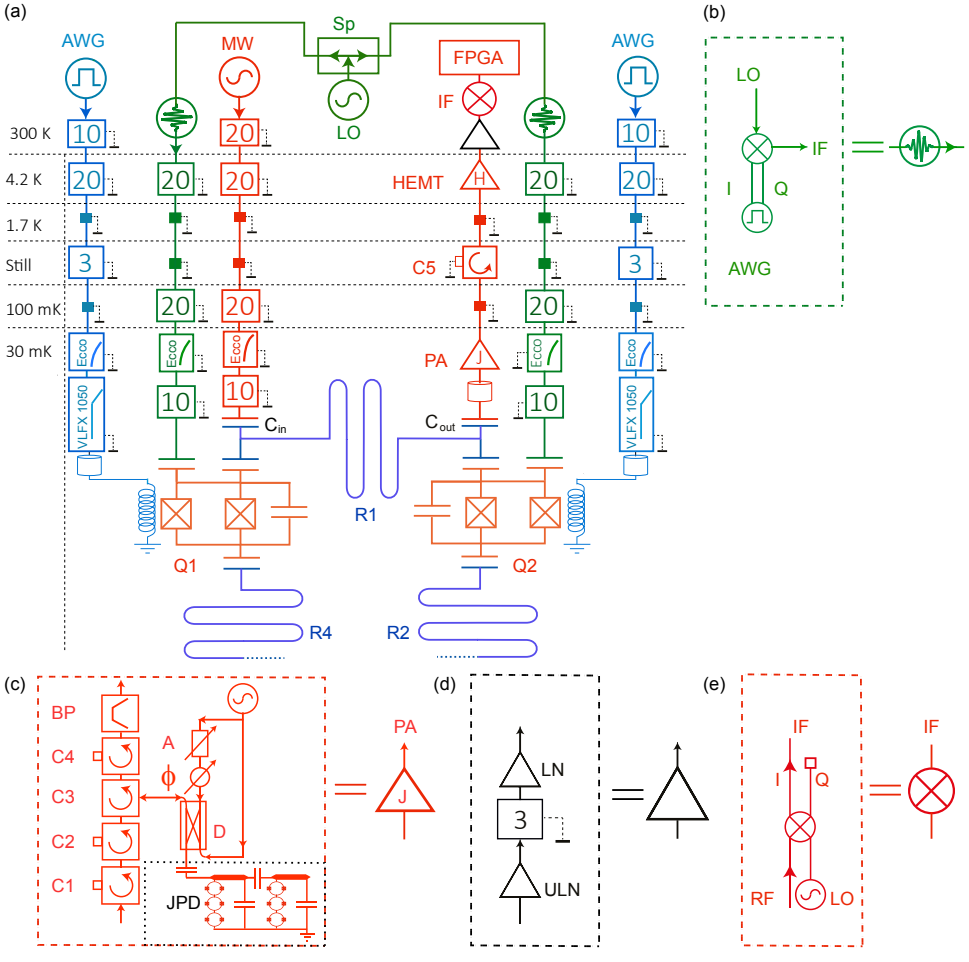

FIGURE A.2: (a) Schematic of the experimental setup with complete wiring of electronic components inside and outside of the dilution refrigerator with the same color code as in Fig. A.1. (b) Up conversion circuit for generating controlled microwave pulses. (c) Quantum limited parametric amplifier circuit to amplify readout pulses at base temperature. (d) Amplifiers used at room temperature just before down conversion of the signal. (e) Down conversion circuit (See text for details).

Since the outcome of the XY gate depends strongly on the relative phase of the two-qubit input state, we have used the same LO signal for the upconversion of the single-qubit pulses acting on both qubits Q1 and Q2 (green lines in Fig. A.2a). Then the initial relative phase between the qubits is defined solely by the pulse sequence

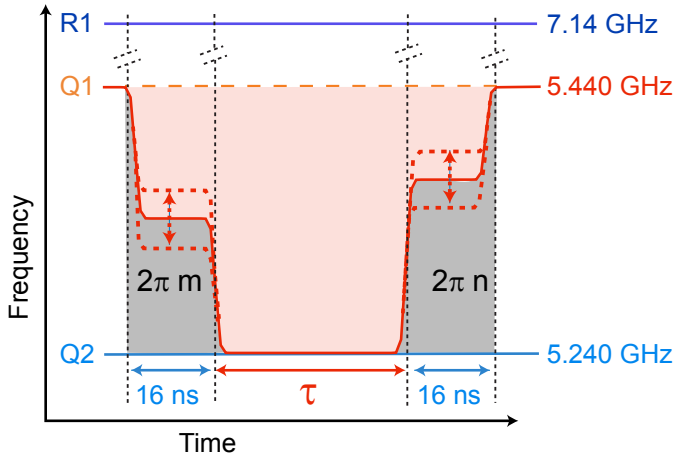

FIGURE A.3: Implementation of the XY gate. The transition frequency of qubit Q1 (red) is tuned into resonance with qubit Q2 (blue) for an interaction time τ using a fast flux pulse. Before and after the flux pulse, a 16 ns long buffer is added at an intermediate level to cancel the dynamic phase accumulated by qubit Q1 relative to Q2 (grey area) during the evolution (see text).

generated by the AWG and the cable lengths. In addition, we choose the shape of the flux pulse that realizes the XY gate such that the dynamic phase acquired by qubit Q1 during the idle time and the rising edge of the flux pulse cancels any unwanted relative phase offset of the initial state. We satisfy this condition by tuning the frequency of Q1 to an intermediate level (buffer) for a fixed time of 16 ns before and after the XY gate (Fig. A.3). A suitable buffer level is found by performing Ramsey-type experiments with a single XY gate while sweeping the buffer amplitudes. This calibration procedure is carried out for each interaction length of the XY gate. The second buffer at the falling edge of the flux pulse is used to ascertain that the relative phase between the qubits after tuning qubit Q1 back to its original position is the same as the initial relative phase.

A.3 Pulse Scheme

The quantum protocols for the digital quantum simulation of Heisenberg (Fig. A.4**a**) and Ising spin (Fig. A.4**b**) models were realized by sequences of microwave and

flux pulses applied on qubit Q1 (red curves in Fig. A.4) and qubit Q2 (blue curves in Fig. A.4). The single-qubit rotations were implemented by 24 ns long Gaussian-shaped resonant DRAG [151, 152] microwave pulses and the XY gates were implemented using fast flux pulses. To avoid the effect of residual transient response of the flux pulse we have added a 40 ns + $\Delta\tau$ waiting time after each flux pulse, with $\Delta\tau$ being an adjustable idle time. We have chosen $\Delta\tau$ such that the time difference between two applications of the XY interaction is commensurate with the relative phase oscillation period of 5 ns, equal to the inverse frequency detuning 1/200 MHz. With these measures we ensure that the gate can be used in a modular fashion, i.e. that a single calibration of the gate suffices for all gate realizations within the algorithm. The single-qubit phase gates were implemented by detuning the idle frequencies of each qubit with a square flux pulse. In the idle state, we observe a state-dependent qubit transition frequency shift of 940 kHz due to the residual $\sigma_1^z\sigma_2^z$ interaction. To decouple this undesired effect we have used a standard refocusing technique [153] implemented by two consecutive π pulses on qubit Q2 (magenta boxes in Fig. A.4). In the end of each pulse sequence we perform dispersive joint two-qubit state-tomography [154] by single-qubit basis transformations followed by a pulsed microwave transmission measurement through resonator R1.

A.4 Process Tomography

We perform standard two-qubit process tomography [155, 156] of the XY gate and of the simulated isotropic Heisenberg (XYZ) model for a varying interaction time τ. Fig. A.5 shows the process χ matrices characterizing the XY gate for a quantum phase angle $\pi/2$ (Fig. A.5a) and π (Fig. A.5b) corresponding to a $\sqrt{i\text{SWAP}}$ gate [92, 157] and an iSWAP gate [73, 158] with process fidelities of 97.8 % and 95.3 %, respectively. Heisenberg interaction with a quantum phase angle $\pi/2$ leads to a SWAP gate (Fig. A.6a) with a process fidelity of 86.1 %. While the SWAP gate belongs to the two-qubit Clifford group, there is no natural interaction in standard circuit QED architecture to directly implement the SWAP gate [159, 160]. For a phase angle π, the Heisenberg interaction is an identity gate (Fig. A.6b) with a process fidelity of 83.6 %.

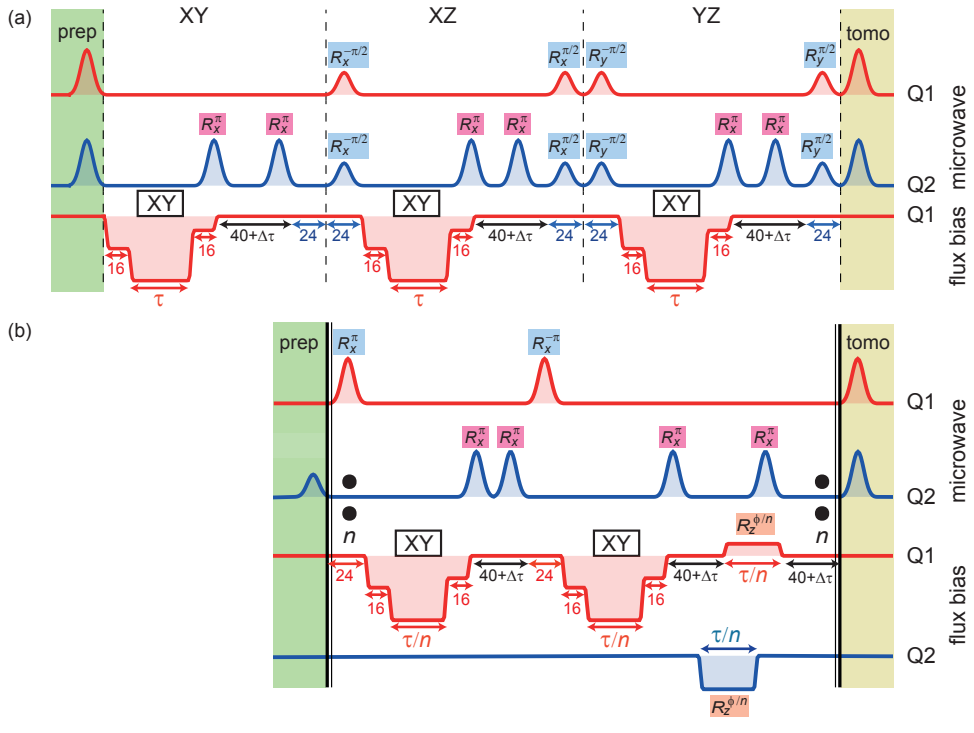

FIGURE A.4: Pulse sequences that are applied on qubit Q1 (red) and qubit Q2 (blue) to implement the Heisenberg (a) and Ising spin (b) models. The Gaussian-shaped DRAG microwave pulses are applied to the charge lines of the respective qubits to implement single-qubit rotations $R^{\phi}_{x,y}$ about the x or y axis of the Bloch vector by an angle ϕ. Each sequence starts with the preparation of an initial state (green boxes) and ends with microwave pulses for basis rotations to perform state-tomography (yellow boxes). The microwave pulses marked with magenta boxes are used for refocussing. The black vertical bars with the two dots in panel (b) indicate that the enclosed pulse sequence is repeated n times. The XY gates are realized by applying flux pulses to the flux line of qubit Q1 for a time τ/n. The phase gates $R_z^{\phi/n}$ are implemented by detuning the transition frequency of each qubit from their idle frequencies applying flux pulses for a time τ/n. The numbers stated below the pulses on qubit Q1 represent timescales in ns.

A.5 Error Contributions

The single-qubit gate fidelities measured by randomized benchmarking [161–163] amount to 99.7 %. The dominant contribution to the loss in fidelity originates from the two-qubit XY gates for which a process fidelity $\mathcal{F}_{\mathrm{p,XY}} = 95.7\,\%$ is obtained

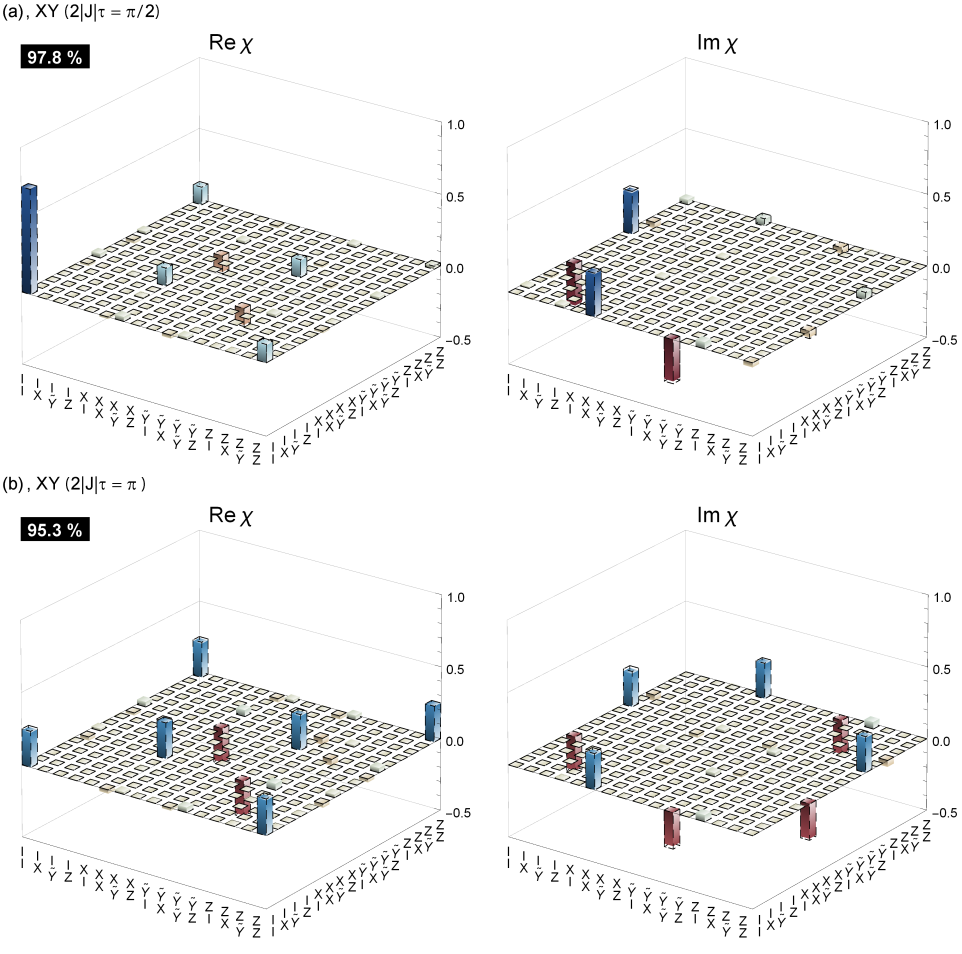

FIGURE A.5: (a) Measured real and imaginary part of the XY process χ matrix (Re χ, Im χ), in the basis $\{I = \textit{identity}, X = \sigma^x, \tilde{Y} = -i\sigma^y, Z = \sigma^z\}$, describing the mapping from any initial state to the final state for a quantum phase angle of $2|J|\tau = \pi/2$. The dashed wire frames represent the theoretically optimal matrix elements and the colored bars represent measured positive (blue) and negative (red) matrix elements. The fidelity of the experimentally observed process with respect to the ideal process is indicated in the black boxes. (b) As in (a) for a phase angle π.

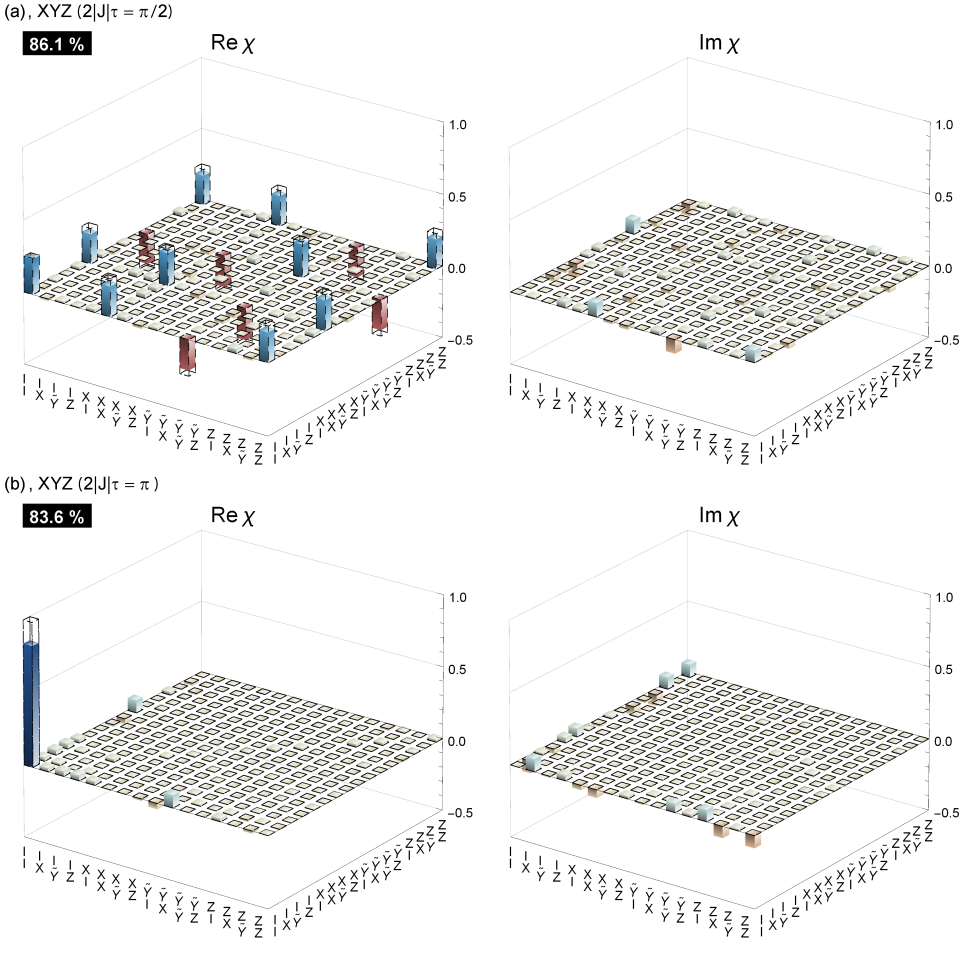

FIGURE A.6: (a) Measured real and imaginary part of the Heisenberg (XYZ) process χ matrix (Re χ, Im χ), in the basis $\{I = \textit{identity}, X = \sigma^x, \tilde{Y} = -i\sigma^y, Z = \sigma^z\}$, describing the mapping from any initial state to the final state for a quantum phase angle of $2|J|\tau = \pi/2$. The dashed wire frames represent the theoretically optimal matrix elements and the colored bars represent measured positive (blue) and negative (red) matrix elements. The fidelity of the experimentally observed process with respect to the ideal process is indicated in the black boxes. (b) As in (a) for a phase angle π.

from process tomography averaging over all quantum phase angles. This indicates that the errors in the implementation of the XY gate limit the fidelity of the final state of the quantum simulation. To confirm this, we calculate the expected process fidelity for the Heisenberg and Ising protocol from the observed XY gate fidelity by assuming independent gate errors in all three steps. For the Heisenberg (XYZ) model simulation neglecting the small single-qubit gate errors, we expect a mean process fidelity $\mathcal{F}_{\mathrm{p,XYZ}} \approx 1 - 3(1 - \mathcal{F}_{\mathrm{p,XY}}) = 87.1\,\%$, which is close to the observed value of 86.3 %. For the Ising model simulation we expect a process fidelity of $\mathcal{F}_{\mathrm{p,Ising}} \approx 1 - 2n(1 - \mathcal{F}_{\mathrm{p,XY}})$. From the relation $\mathcal{F}_{\mathrm{s}} = (d\mathcal{F}_{\mathrm{p}} + 1)/(d + 1)$ between state ($\mathcal{F}_s$) and process fidelity ($\mathcal{F}_p$), we obtain the expected mean state fidelities of $\{93.1, 86.2, 79.4, 72.5, 65.6\}\,\%$ for $n = 1$ to 5 Trotter steps which compare well to the measured state fidelites $\{91.7, 88.3, 82.2, 73.0, 60.7\}\,\%$.

To estimate the dominant source of systematic errors, we consider a model which includes relaxation (T_1) and dephasing (T_2) and state-dependent phase errors described by an effective $\tilde{J}_z\sigma_1^z\sigma_2^z$ term with interaction strength $\tilde{J}_z$. In addition, we include an extra offset in the single-qubit phase gate acting on qubit Q2 from cross talk of the flux pulses acting on qubit Q1 in each Trotter step. By fitting the final state predicted by this model to the observed states, we estimate an unwanted interaction angle $\tilde{J}_z\tau_z$ of approximately 2.3° and a constant phase offset of 4.6°.

Appendix B

Aspects of Digitized Adiabatic Quantum Simulation Experiment

In this Appendix, we provide details of the experimental implementation of the digitized adiabatic quantum computing protocol at Google/University of California, Santa Barbara, studied in Chapter 4.

B.1 Why Digitized Adiabatic Quantum Computing?

Implementing an adiabatic quantum algorithm on a gate-based quantum computer has been discussed in the original works introducing adiabatic quantum computing (AQC) [116, 127]. However, the motivation for those works was to investigate the power of AQC by mapping the adiabatic algorithm to the gate model [129, 164, 165]. In this work, we promote digitized AQC as a viable quantum algorithm for execution on an error corrected digital quantum device.

In contrast to conventional quantum algorithms, such as Shor's algorithm and Grover's algorithm [2], AQC is a general-purpose optimization algorithm. Any optimization problem, in principle, can be mapped and solved via AQC. However, AQC is a heuristic algorithm as there is no guarantee on the computation run time and it strongly depends on the nature of the problem. It is an active area of research to search for computational problems for which AQC yields a speed-up over its classical counterparts [117, 166–170]. AQC is an approach to quantum computing that uses continuous dynamics. Therefore, building an analog processor to implement an adiabatic quantum evolution is a natural choice. Such a processor is commonly known as a quantum annealer. An analog quantum annealer has certain limitations that we propose can be overcome by a gate-model realization of the AQC. Here we list some key features that boosts the algorithmic success of a quantum annealer:

Graph connectivity and k-body interactions- These factors yield a computational landscape with tall and narrow energy barriers that make it easier for AQC to outperform those algorithms that use classical dynamics, such as simulated thermal annealing [171], spin Monte Carlo [172], and cluster finding based algorithms [173].

Arbitrary interactions- AQC becomes a platform for universal quantum computing when it has programmable non-stoquastic Hamiltonian terms [129, 164, 165, 174]. A Hamiltonian is non-stoquastic when there is no representation in a standard basis with all non-positive off-diagonal terms [175, 176]. In the context of many-body physics, fermionic systems [124] or spin systems with Heisenberg XYZ interactions [176] are some examples for non-stoquastic Hamiltonians which suffer from the sign problem. Realizing arbitrary off-diagonal interactions is a significant problem for analog systems as it requires perturbative gadgets with great precision [174, 177, 178].

Precision- Encoding computational problems in a quantum annealer such as the number partitioning problem [166, 179], requires high level of precision in tuning the interaction between qubits. Therefore a higher precision in programming the problem Hamiltonian is an essential feature for a quantum annealer.

Coherence and scalability- Suppression of errors in analog AQC is an active area of research [180, 181]. However, as there is no established error correction formalism for full fault-tolerant AQC, decoherence can be a major limitation for analog quantum computers. Thermal noise may preferentially drive an analog system into low energy

states [125, 182], but also sets a limit to the distinguishability of energy differences and therefore the size of the problem. A non-corrected digital approach is ultimately limited by the accumulation of gate error. A critical advantage of the digital approach is that it allows for the implementation of full fault tolerance, making this approach scalable.

Nonclassical metrics- One of the advantages of digital methods is the possibility to perform arbitrary dynamical evolution and to combine it with full state tomography for a reduced number of qubits, as used in this manuscript, as well as with enhanced quantum protocols like embedding quantum simulators for determining entanglement monotones without full tomography [183].

Each of the above features adds to the hardware complexity of an analog quantum annealer. It would be realistic to say that any design would inevitably compromise some of these elements. A digital approach to AQC, however, has no fundamental limit to achieve the above features since it simulates AQC with single and two-qubit gates. Of course there is a cost in terms of required qubits, which will be discussed next.

B.2 Methods of Digitization and Discussion of Scaling

The experiments in this paper explore the digitization of adiabatic quantum computing using the first-order Lie-Trotter-Suzuki formula [20, 21]. We now discuss the scaling of the number of gates that this scheme requires to prepare the target state to within fixed error. We restrict our focus to adiabatic evolutions under time-dependent Hamiltonians that are decomposable into L different k-local Hamiltonians such that $H(t) = \sum_{\ell=1}^{L} a_\ell(t) H_\ell$ where the $a_\ell(t)$ are time-dependent scalars and the H_ℓ are local Hamiltonians having many-body order of at most k [184]. We approximate a continuous time evolution for time T by discretizing time into steps of equal size, $\delta t = T/M$ where M is the number of time steps. In our experiment the digitization

of the continuous time evolution is simulated as

$$U_{\text{digital}} = \prod_{m=1}^{M} \prod_{\ell=1}^{L} \exp\left[-i\delta t\, a_\ell\left(m\delta t\right) H_\ell\right]. \tag{S1}$$

Assuming the ability to implement arbitrary rotations, evolution under any k-local Hamiltonian can be implemented using a number of gates that is at most $\mathcal{O}(k)$. Thus, the gate complexity of this approach is $\mathcal{O}(MLk)$. We now address how M should be chosen to perform a continuous time evolution $U_{\text{continuous}}$ such that $\|U_{\text{continuous}} - U_{\text{digital}}\| \leq \epsilon$. Here ϵ upper-bounds the largest error that can be induced on any eigenstate of the Hamiltonian. While the strategy is not employed in our experiment, one can derive a significantly tighter bound on the discretization error by making the following substitution to Eq. S1 [185],

$$\delta t\, a_\ell\left(m\delta t\right) \rightarrow \int_{(m-1)\delta t}^{m\delta t} a_\ell\left(s\right) ds. \tag{S2}$$

In [22, 186], it is shown that such an evolution can be simulated with error ϵ by choosing $M = T^2 a_{\max}^2 L^2/\epsilon$ where $a_{\max} = \max_{\ell,t}\{a_\ell(t)\}$. The adiabatic theorem [116] dictates that T should be chosen as,

$$T = \mathcal{O}\left(\frac{\max_t \left|\langle 1;t|\frac{dH(t)}{dt}|0;t\rangle\right|}{\gamma^2}\right) = \mathcal{O}\left(\frac{D}{\gamma^2}\right) \tag{S3}$$

where γ is the minimum spectral gap during the adiabatic evolution, $|0;t\rangle$ and $|1;t\rangle$ denote the ground and first excited state at time t. Putting these bounds together we find that the total number of gates should scale as

$$\mathcal{O}\left(MLk\right) = \mathcal{O}\left(\frac{T^2 a_{\max}^2 L^3 k}{\epsilon}\right) = \mathcal{O}\left(\frac{a_{\max}^2 D^2 L^3 k}{\gamma^4 \epsilon}\right). \tag{S4}$$

We chose simple first order Trotterization for this experiment only because of experimental limitations. Since, due to substantial overhead in L, k and γ^{-1}, it is unlikely that an approach based on the first order Trotter decomposition will be of practical use. With a future device of larger size and better coherence, we would be able to significantly improve the method of digitization. For instance, a digital simulation scheme based on the truncation of the Taylor series of the time-evolution operator

[139] has been shown to exponentially outperform Trotterization in terms of ϵ, scale linearly with T (up to logarithmic factors), which implies a quadratic reduction in γ^{-1}, and scale much better with the number of terms for real world applications such as the simulation of chemistry [123, 146, 187]. As quantum hardware improves, the implementation of near-optimal schemes such as this becomes increasingly viable.

B.3 Residual Energy Scaling

Here, we motivate the residual energy and its scaling with simulated time and number of spins. We find that for large Ising spin chains the residual energy follows a power law, $T^{-\eta}$ with $\eta \geq 0.5$.

The standard picture of AQC describes that the ground state of a Hamiltonian (problem Hamiltonian) encodes the solution of a computational problem. Quantum adiabatic theorem tells us how slowly we should drive the system to reach to this target state with high probability. Therefore a measure of success for computation is the overlap between the system state at the end of the evolution and the ground state of the problem Hamiltonian. Such a measure might be unnecessary for optimization problems as most of the time reaching a good local minimum could be satisfactory instead of the global minimum of the ground state. Therefore a relevant measure would be the residual energy above the ground state, the smaller the better.

The Kibble-Zurek mechanism and the Landau-Zener theorem are consistent approaches to estimate the residual energy for a many-body system that slowly passes through a phase transition [188–191]. In the experiment, Fig. 10 in Chapter 4, a transverse field drives a chain of spins with Ising interaction through phase transition at different speeds. The KZ mechanism explains that as a system goes faster through the critical point, there would be less time for spins to communicate in order to find the ground states. That translates into an incomplete formation of the ground state and the emergence of kinks after the phase transition. The density of kinks is monotonically related to the energy of the final exited state. Here we follow the line of argument in Ref. [189] to find the scaling of residual energy at fast and

intermediate speeds. Note that the scaling theory describes dynamics in thermodynamical limit of a large number of spins. However, we see a correspondence between our few-qubit experiment and the scaling analysis presented below.

For fast quench, a system that starts in the superposition of all energy levels (ground state of uniform transverse Hamiltonian) has insufficient time to adjust to lower energy states. Therefore the system stays close to its initial energy distribution with little dependence on the time T. This appears as a plateau in the residual energy plot. For longer evolution times T, we consider a two-level system approximation and apply the Landau-Zener formula that gives the probability of excitement into the first exited state as $P = e^{-\alpha\Delta^2 T}$. For an $N-$spin system of the experiment, with a uniform Ising Hamiltonian, Δ, the minimum gap, scales as $\frac{1}{N}$. For a fixed time T and likelihood p^*, we find the longest defect-free chain as $N^* = |\frac{\alpha}{\ln p^*}|^{\frac{1}{2}} T^{1/2}$. Therefore, to first order the kink density and residual energy scale as $\frac{1}{N^*} \propto T^{-1/2}$. Although our residual energy experiment is small-scale, the two phases of plateau for short times, and a transition to a power law $T^{-\eta}$ with $\eta > 0.5$ are visible.

B.4 Pairwise Interaction in a Nine-Qubit System

The nine qubit chain is placed in a configuration with alternating frequencies for idling. This detuning, together with design and decoupling pulses minimize parasitic interactions from nearby qubits. The coupling strength between nearest neighbours is $g/2\pi = 15$ MHz. The strength between next-nearest neighbours is 0.7 MHz. As $\sigma^z\sigma^z$ interaction scales with g^2, the ratio between unintended and intended coupling is about $2 \cdot 10^{-3}$. Adjacent qubits are detuned by typically 1 GHz, and next-nearest qubits are detuned by 0.1 GHz. The idling configuration is shown in Fig. S1a. Figure S1b shows the implementation of entangling, for example between qubits Q_1 and Q_0, we move Q_0 to a higher frequency, and let Q_1 undergo an adiabatic trajectory which is tuned to bring about a conditional phase shift while minimizing state leakage [17, 192]. We apply decoupling pulses to Q_2 during this interaction. Other qubits undergo entangling gates at the same time. After this interaction, the qubit frequencies are returned to the idling positions.

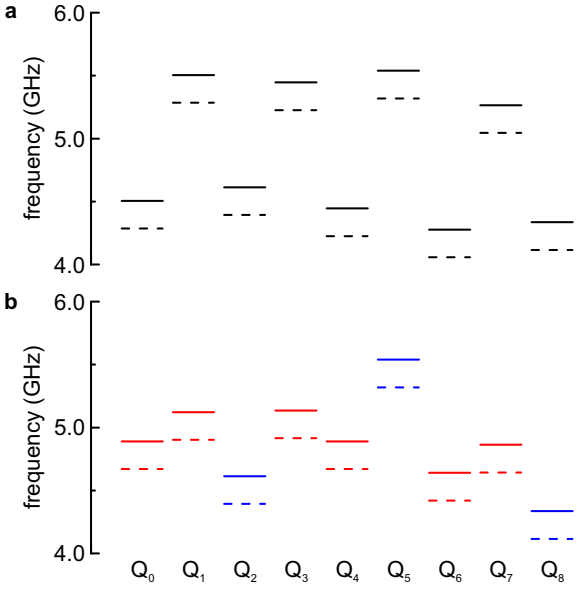

FIGURE S1: **Frequency configuration for idling and interacting.** (a) Idling configuration, showing an alternating frequency pattern designed to minimize interaction. (b) Configuration where qubits interact. Black: idling qubits. Red: adjacent pairs of qubits are performing a CZ_ϕ entangling gate. Blue: qubits which are decoupled using π pulses. This configuration corresponds to the dashed line in Fig. S3a.

B.5 Constructing Interaction

At the core of the multibody interactions is the CZ_ϕ entangling gate. One qubit is held at a steady frequency while the other undergoes an adiabatic trajectory which sweeps $|02\rangle$ close to $|11\rangle$ [192]. By varying the amplitude of this trajectory we can tune the conditional phase [25]. After this interaction we null the single qubit phases, arising from the single qubit frequency detunings. We find that by careful calibrations, we can achieve the desired conditional phase, and null the single qubit phases to within 0.05 rads, see Fig. S2a-b. Other qubits are decoupled from this interaction with π rotations, see below.

The tunable phase is limited between $\phi \sim 0.5$ to ~ 4.5. Below this range interactions with other qubits complicate implementation, and above this range population leakage into higher-energy levels becomes significant. In order to construct a tunable

gate over the full range, we choose one of three implementations based on the desired phase for $\sigma^z \otimes \sigma^z$:

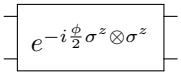

For $\phi > 0.25$:

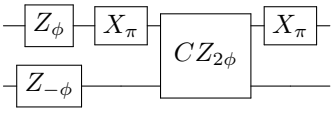

For $-0.25 < \phi < 0.25$:

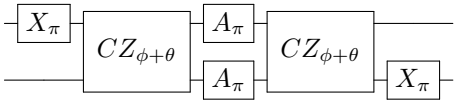

with $A = Y$ and $\theta = \pi$.

And for $\phi < -0.25$:

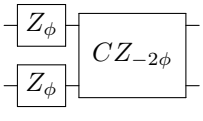

And for $|\phi| > 2.25$ we either apply the quantum circuit with two entangling gates with $A = X$ and $\theta = 0$, or add or subtract 2π until it is in range. Implementing the unitary $U = \exp(-iJ_{zz}\Delta t)$ is then done by setting $\phi = 2J_{zz}\Delta t$. The above identities ensure we can implement any strength of $\sigma^z \otimes \sigma^z$.

B.6 Decoupling from the Environment and Parasitic Interactions

Our qubits have dephasing, dominated by correlated processes, and are susceptible to parasitic interactions with other qubits [193]. To reduce these effects, we include decoupling π pulses in three locations in the algorithm: I) Around the $\sigma^z\sigma^z$ and $\sigma^x\sigma^x$ interaction. At the start of a $\sigma^z\sigma^z$ or $\sigma^x\sigma^x$ interaction we apply an X_π rotation on both qubits; at the end we apply an $\mathrm{X}_{-\pi}$ rotation. This maintains the unitary

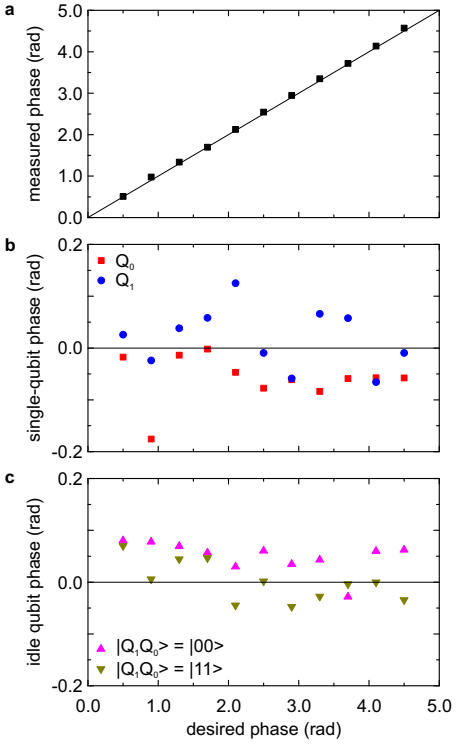

FIGURE S2: **Phases for the CZ$_\phi$ gate.** (a) Measured vs. desired controllable phase ϕ. (b) Residual single-qubit phases. (c) Residual phase on the idling qubit Q_2 for $|Q_1 Q_0\rangle = |00\rangle$ and $|Q_1 Q_0\rangle = |11\rangle$.

but decreases the effects of qubit dephasing. II) Idling qubits are decoupled from the environment by applying two X_π pulses, centered at $\tau/4$ and at $3\tau/4$, with τ being the idling time. III) Qubits which are adjacent to a qubit undergoing a controlled-phase frequency trajectory need to be decoupled from this interaction; in contrast to the idling case, we now apply closely spaced sequential X_π and $X_{-\pi}$ rotations during the frequency trajectory of the other qubit, to null the parasitic interaction. We find mean phase errors from residual parasitic interaction to be around 0.05 rad, which is equivalent to a gate error of $1 - \cos^2(\frac{\delta\phi}{2}) = 6 \cdot 10^{-4}$, see Fig. S2c. With decoupling pulses the errors are dominated by intrinsic gate errors.

B.7 Pulse Sequences

The evolution is digitized using the Trotter expansion [20, 21]. In essence the evolution is divided into many small steps in time, $U = \mathcal{T}\exp(-i\int H(t)dt) \simeq \exp(-iH(t_1)\Delta t)\exp(-iH(t_2)\Delta t)...$, where each $H(t_n)$ is comprised of terms which sum up to $H(t_n) = \sum_\ell H_\ell(t_n)$, implemented using a construction of quantum logic gates. Local fields come from single qubit gates, and the full range of $\sigma^z\sigma^z$ and $\sigma^x\sigma^x$ couplings come from one or two CZ_ϕ gates in a combination with single qubit gates.

The pulse sequences are shown in Fig. S3 for the scaling experiment with nine qubits (Fig. 4.10 in Chapter 4), and for the random stoquastic and non-stoquastic problems with six to nine qubits (Fig. 4.11 in Chapter 4). Slow, rectangular-like pulses are frequency detunings, and rapidly oscillating waveforms denote microwave pulses. Numbers in the figure correspond to the following:

1. Initial state preparation: $|+\rangle^{\otimes N}$, with $N = 9$ qubits.
2. First Trotter step
3. Second Trotter step
4. $\sigma^z\sigma^z$ interaction: consisting of decoupling pulses, Q_0 being moved to an interaction frequency, and Q_1 performing the trajectory.

TABLE S1: Gate counts for pulse sequences in Fig. S3. We count idles as any duration of 10 ns or longer. Long idles are counted as a single idle, even though the relevant approach for estimating total process fidelities is by splitting idles in terms of durations of the microwave gates [17]. The gate counts are for the full algorithm, all Trotter steps as well as initialization.

	a	b	c	d	e
entangling CZ_ϕ gates	16	29	52	26	18
single qubit gates	263	550	1059	486	326
- microwave π and $\pi/2$	135	292	598	282	173
- idle	78	178	331	142	103
- virtual phase	50	80	130	62	50

5. Environmental decoupling pulses: π pulses around $\sigma^z\sigma^z$, but such that the ideal unitary is unchanged
6. Decoupling pulses to reduce parasitic interactions with idling qubits
7. Environmental decoupling pulses
8. Implementation of B_x. The decrease in amplitude with Trotter step reflects the decrease in B_x following the annealing schedule.
9. $\sigma^z\sigma^z$ interaction for an angle which requires 2 CZ_ϕ gates.
10. First Trotter step of the non-stoquastic problem evolution, showing both $\sigma^z\sigma^z$ and $\sigma^x\sigma^x$ interaction. Note that other qubits have to wait if a pair has an interaction strength which requires 2 CZ_ϕ gates.
11. $\sigma^z\sigma^z$ interaction with large and small angles
12. $\sigma^x\sigma^x$ interaction, showing the $\pi/2$ pulses for basis rotation.
13. Notice how $\sigma^x\sigma^x$ interaction in the second Trotter step is now done with only a single CZ_ϕ gate. The coupling strength is linearly turned on and phases increase, allowing the interaction to be implemented with a single entangling gate.
14. As a result the Trotter steps 2-5 are shorter than the first.
15. Qubit frequency configuration shown in Fig. S1b.

A gate count of the sequences is provided in Table S1.

B.8 Simulation Parameters

An overview of the number of Trotter steps, simulated times, coupling and field strengths for the performed experiments is shown in Table S2. For the single instances shown in Chapter 4 see Tables S4-S3.

B.9 Digital Evolution into GHZ State: Imaginary Parts and Ideal Adiabatic Evolution

The real and imaginary parts, as well as the ideal adiabatic evolution and target state for the experiment in Chapter 4 in Fig. 4.9 at $s = 1.0$ are shown in Fig. S4. The fidelity of the ideal adiabatic evolution with respect to the target state is 0.92.

TABLE S2: Simulation parameters for the experiments. Random problem denotes both the stoquastic and non-stoquastic one.

experiment	coupling	local field	Trotter steps	simulated time
ferromagnetic chain	$J_{zz} = 2$	None	5	$T = 3$
scaling (2-6 qubits)	$J_{zz} = 2$	None	3	$T = 0...1.5$
scaling (7-9 qubits)	$J_{zz} = 2$	None	2	$T = 0...1.5$
AF chain w. local field	$J_{zz} = -1.25$	middle qubit: $B_z = -3...3$	4	$T = 2.5$
random problem, 3 qubits	$-2... - 0.5$ or $0.5...2$	$-2...2$	5	$T = 3$
random problem, 6 qubits	$-2... - 0.5$ or $0.5...2$	$-2...2$	5	$T = 3$
random problem, 7 qubits	$-2... - 0.5$ or $0.5...2$	$-2...2$	2	$T = 1$
random problem, 8 qubits	$-2... - 0.5$ or $0.5...2$	$-2...2$	2	$T = 1$
random problem, 9 qubits	$-2... - 0.5$ or $0.5...2$	$-2...2$	2	$T = 1$

TABLE S3: Nine qubit stoquastic problem instance.

	Q_0	Q_1	Q_2	Q_3	Q_4	Q_5	Q_6	Q_7	Q_8
B_x	1.437	0.749	0.912	1.153	1.523	1.670	1.621	1.930	-0.899
B_z	-0.559	-1.078	-1.822	-0.407	0.652	1.675	1.362	0.302	-0.187
J_{zz}	-0.781	-1.672	0.520	0.635	0.812	-0.816	1.162	0.639	

The fidelity of the experimental data with respect to the ideal adiabatic evolution is 0.60.

B.10 Kink Likelihood for Two to Nine-Qubit Configurations

The kink likelihood for configurations with two to nine qubits is shown in Fig. S5. For two qubits, only a single kink is possible ($|01\rangle$ or $|10\rangle$), and initially no kink or a single kink are equally likely. When increasing the simulation time the kink likelihood decreases, and the likelihood of no kinks increases. This picture is repeated for all systems. For the seven to nine qubit systems, around $|J|T = 2$, the likelihood of kinks increases again. The experimental data closely follow the ideal digital evolution (dashed).

The differences in residual energies are plotted in Fig. S6, for three, six and nine qubits. The increase in difference for the nine qubit system near $|J|T = 3$ (dashed and dotted blue lines) is due to digitization error, as the experiment follows the ideal digital evolution to within a difference of $2|J|$ (solid blue line).

Table S4: Three qubit stoquastic problem instance.

	Q_0	Q_1	Q_2
B_x	-0.159	1.22	-1.93
B_z	-1.29	-1.45	-0.772
J_{zz}	-1.09	1.16	

Table S5: Three qubit non-stoquastic problem instance.

	Q_0	Q_1	Q_2
B_x	-1.18	-1.71	1.02
B_z	-0.875	0.781	-0.428
J_{xx}	-0.841	1.02	
J_{zz}	-0.757	1.32	

B.11 Local Fields and Long-Range Spin Parity Correlation

We explore the lifting of degeneracy with and the long-range effects of local fields. We apply a local Z field (B_Z) on the middle qubit of a five-qubit antiferromagnetic chain.

TABLE S6: Six qubit stoquastic problem instance.

	Q_0	Q_1	Q_2	Q_3	Q_4	Q_5
B_x	0.155	-1.238	1.789	0.899	-1.501	-1.309
B_z	0.468	-1.577	-1.183	-0.665	-0.928	-1.265
J_{zz}		1.476	-0.740	-0.765	-0.535	-0.966

TABLE S7: Six qubit non-stoquastic problem instance.

	Q_0	Q_1	Q_2	Q_3	Q_4	Q_5
B_x	-0.255	0.606	-1.735	0.732	1.586	-0.305
B_z	-1.672	-1.282	-1.532	-1.433	1.282	-1.765
J_{xx}		0.577	-1.954	-1.616	-1.517	-1.896
J_{zz}		-1.491	-1.349	-0.628	-1.287	-1.919

TABLE S8: Seven qubit non-stoquastic problem instance.

	Q_0	Q_1	Q_2	Q_3	Q_4	Q_5	Q_6
B_x	-1.335	0.760	-1.261	-0.221	-0.892	-1.321	0.133
B_z	-1.026	-1.896	-0.116	-0.619	-0.493	-1.316	-1.872
J_{xx}		1.891	1.517	1.568	0.748	1.419	-0.839
J_{zz}		-1.455	-0.588	-0.582	-1.223	-0.635	-0.614

In Fig. S7a we show the single spin magnetization $< \sigma_i^z >$ for all qubits of index i as a function of B_z. In the absence of a field, the state is degenerate, and the single qubit magnetizations are zero. With local field, the magnetization develops and displays the hallmark antiparallel configuration, following the ideal digital predictions (right). The experimental data follow the ideal digital results more closely for $B_z > 0$, we attribute this to gate errors arising from the asymmetry of implementation with sign. We also plot in Fig. S7b the parity $< \sigma_i^z \sigma_{i+d}^z >$ with distance d, averaged over B_z. The mean correlation alternates sign (not shown) and decreases with distance, following the ideal trend.

Spin parity correlations for the five qubit antiferromagnetic experiment are displayed in Fig. S8 as a function of distance d and magnetic field. The measured parity correlations (left) reflect the anti-ferromagnetic nature: the correlation is negative for odd distances and positive otherwise. The correlations follow the theory predictions (right) for either direction.

These experiment show that long-range correlations are generated in the system, even though the physical coupling of the system is nearest-neighbour only, and become visible when we apply local fields and lift the degeneracy of the antiferromagnetic state, creating classical Néel states.

B.12 Gate Calibrations

Variable single qubit microwave rotations are calibrated by inferring the rotation angle from measurements of the probability with amplitude (Fig. S9a). The tunable CZ_ϕ gate is calibrated by placing the static qubit in an equator state, and placing the other qubit in either $|0\rangle$ or $|1\rangle$, and varying the amplitude of the trajectory. By performing quantum state tomography on the static qubit the tunable phase becomes apparent, see Fig. S9b.

B.13 Comparison between Predicted and Experimental Fidelities

Here, we list comparisons between experiment, ideal digital evolution, ideal continuous evolution as well as the target state results, expressed as fidelities. We also show comparisons with uniformly chosen random probabilities as a baseline sanity check. A complete overview is shown in Table S9.

We also show the histograms of all fidelities in Fig. S10.

Fidelities for the example instances of Fig. 11 in Chapter 4 are in Table S10.

TABLE S9: Mean fidelities between the experimental data, the ideal digital evolution, ideal continuous evolution (ideal cont.) and target state. As a baseline sanity check, we also show comparisons with randomly generated data. The standard deviations from the mean are given.

data	ideal digital evolution	ideal continuous evolution	target state
	3 qubits, stoquastic		
experiment	0.706 ± 0.007	0.48 ± 0.01	0.36 ± 0.02
ideal digital		0.67 ± 0.01	0.46 ± 0.02
ideal cont.			0.61 ± 0.03
	3 qubits, non-stoquastic		
experiment	0.36 ± 0.01	0.220 ± 0.009	0.185 ± 0.009
ideal digital		0.49 ± 0.02	0.29 ± 0.02
ideal cont.			0.53 ± 0.03
	6 qubits, stoquastic		
experiment	0.714 ± 0.006	0.523 ± 0.008	0.296 ± 0.007
random	0.496 ± 0.007	0.340 ± 0.007	0.168 ± 0.005
ideal digital		0.73 ± 0.01	0.43 ± 0.01
ideal cont.			0.59 ± 0.01

data	ideal digital evolution	ideal continuous evolution	target state
		6 qubits, non-stoquastic	
experiment	0.739 ± 0.004	0.522 ± 0.008	0.380 ± 0.009
random	0.669 ± 0.004	0.470 ± 0.007	0.335 ± 0.008
ideal digital		0.526 ± 0.009	0.350 ± 0.009
ideal cont.			0.62 ± 0.01
		7 qubits, stoquastic	
experiment	0.645 ± 0.006	0.607 ± 0.006	0.215 ± 0.009
random	0.543 ± 0.006	0.534 ± 0.006	0.133 ± 0.006
ideal digital		0.883 ± 0.004	0.332 ± 0.009
ideal cont.			0.281 ± 0.009
		7 qubits, non-stoquastic	
experiment	0.632 ± 0.006	0.566 ± 0.006	0.311 ± 0.009
random	0.607 ± 0.005	0.553 ± 0.006	0.277 ± 0.008
ideal digital		0.812 ± 0.006	0.34 ± 0.01
ideal cont.			0.36 ± 0.01
		8 qubits, stoquastic	
experiment	0.606 ± 0.006	0.570 ± 0.006	0.164 ± 0.007
random	0.513 ± 0.006	0.509 ± 0.006	0.091 ± 0.004
ideal digital		0.873 ± 0.004	0.274 ± 0.008
ideal cont.			0.225 ± 0.007
		8 qubits, non-stoquastic	
experiment	0.572 ± 0.005	0.499 ± 0.006	0.245 ± 0.008
random	0.585 ± 0.005	0.517 ± 0.005	0.238 ± 0.007
ideal digital		0.775 ± 0.006	0.292 ± 0.009
ideal cont.			0.32 ± 0.01
		9 qubits, stoquastic	
experiment	0.583 ± 0.007	0.551 ± 0.006	0.122 ± 0.006
random	0.496 ± 0.006	0.481 ± 0.006	0.074 ± 0.004
ideal digital		0.862 ± 0.004	0.228 ± 0.007
ideal cont.			0.184 ± 0.007

data	ideal digital evolution	ideal continuous evolution	target state
	9 qubits, non-stoquastic		
experiment	0.587 ± 0.006	0.507 ± 0.006	0.236 ± 0.008
random	0.570 ± 0.004	0.495 ± 0.005	0.214 ± 0.008
ideal digital		0.747 ± 0.006	0.248 ± 0.008
ideal cont.			0.27 ± 0.01

TABLE S10: Fidelities and measures of success for the example instances in Fig. 11 between the experimental data, the ideal digital evolution, ideal continuous evolution (ideal cont.) and target state.

data	ideal digital evolution	ideal continuous evolution	target state
	3 qubits, stoquastic		
experiment	0.70	0.68	0.63
ideal digital		0.96	0.90
ideal cont.			0.92
	3 qubits, non-stoquastic		
experiment	0.48	0.43	0.42
ideal digital		0.82	0.60
ideal cont.			0.59
	6 qubits, stoquastic		
experiment	0.78	0.69	0.65
ideal digital		0.90	0.61
ideal cont.			0.62
	6 qubits, non-stoquastic		
experiment	0.76	0.72	0.42
ideal digital		0.65	0.38
ideal cont.			0.52
	9 qubits, stoquastic		
experiment	0.66	0.60	0.63
ideal digital		0.83	0.64
ideal cont.			0.77
	7 qubits, non-stoquastic		
experiment	0.71	0.76	0.71
ideal digital		0.77	0.53
ideal cont.			0.69

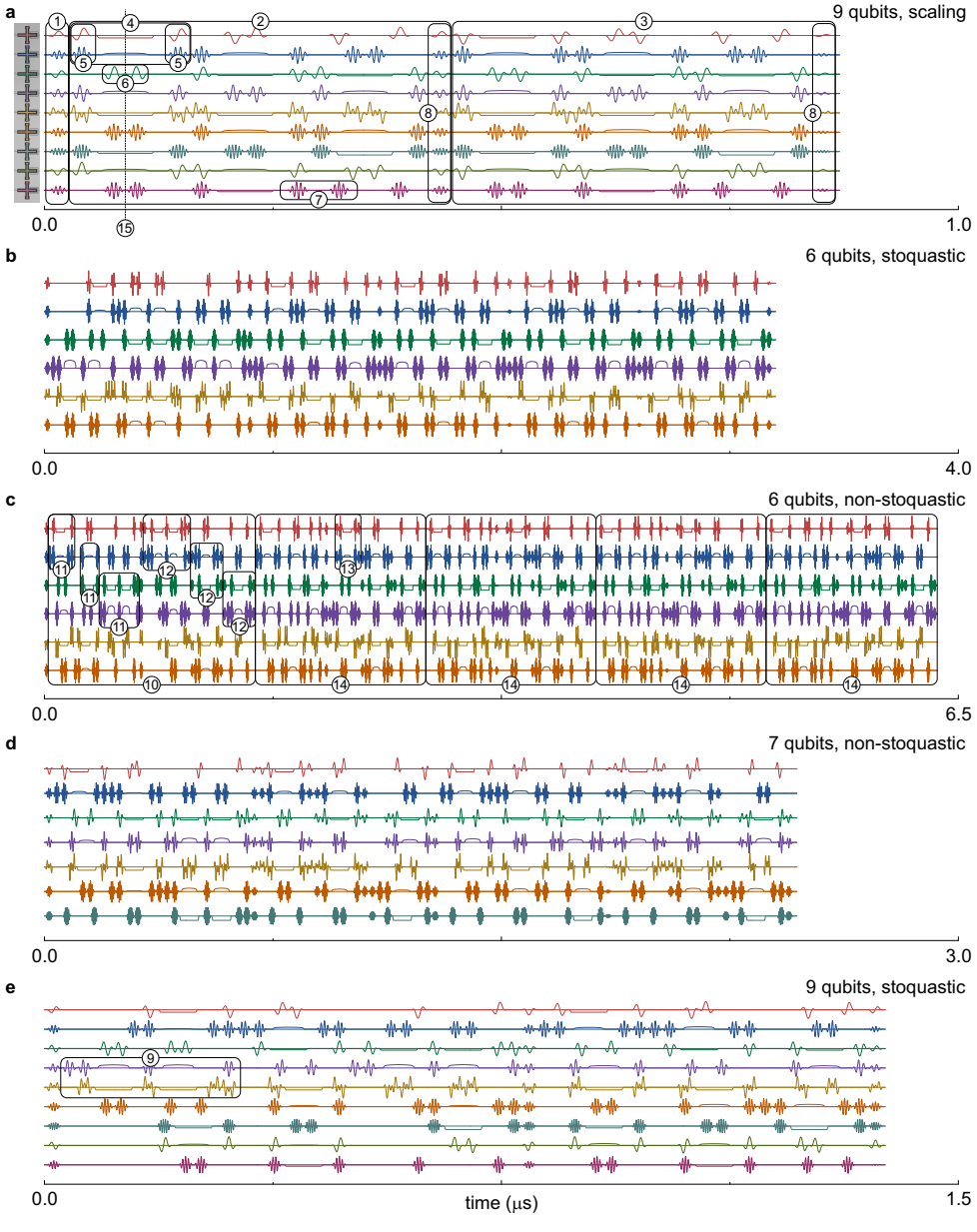

FIGURE S3: **Pulse sequences.** (a) Nine qubit scaling experiment at $T = 1$ from Fig. 4.10 in Chapter 4. (b) Six qubit stoquastic problem from Fig. 4.11b in Chapter 4. (c) Six qubit non-stoquastic problem from Fig. 4.11e in Chapter 4. (d) Seven qubit non-stoquastic problem. (e) Nine qubit stoquastic problem. The numbers in the figures are explained in the main text.

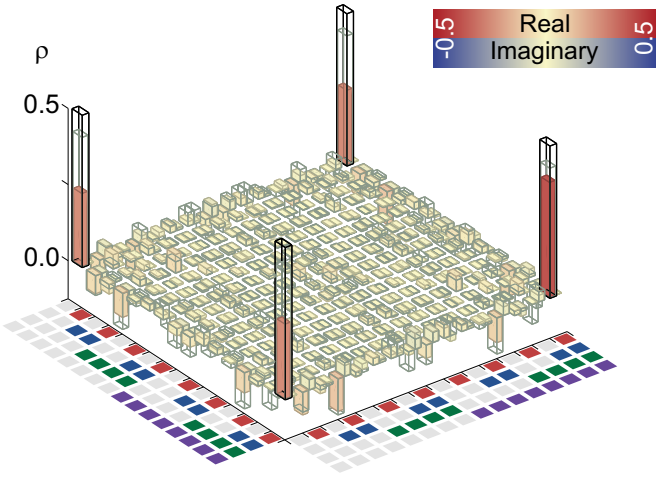

FIGURE S4: **Digital evolution into GHZ state: real, imaginary parts and ideal continuous time evolution.** Experimental data (colour), target state (black) and ideal continuous time evolution (gray) at $s = 1.0$. The leftmost red bars indicate the real part, the adjacent blue bars indicate the imaginary part. $\mathrm{Im}(\rho) < 0.05$.

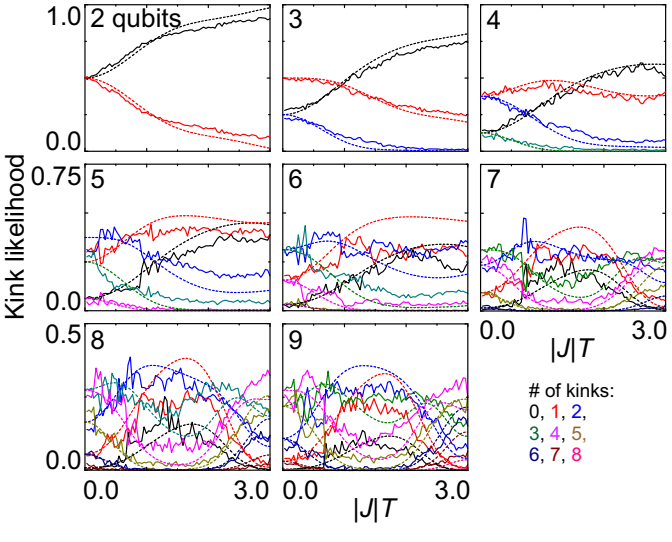

FIGURE S5: **Kink likelihood for two to nine qubit configurations.** Errors in ferromagnetic chains ($J = 2$) in configurations with two to nine qubits. Kink likelihood versus scaled time $|J|T$. Solid lines: experiment. Dashed lines: ideal digital evolution.

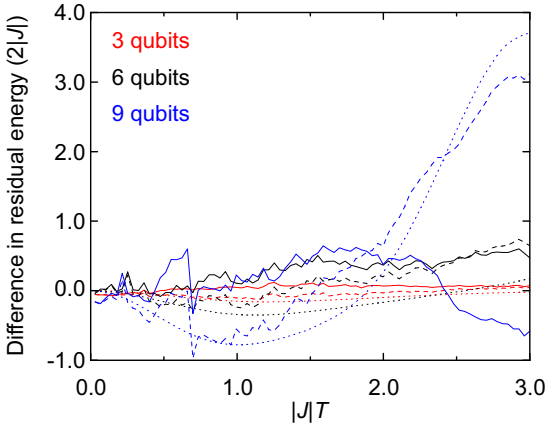

FIGURE S6: **Differences between residual energy for the experimental, ideal digital, and ideal continuous evolutions.** Residual energy difference for three, six, and nine qubits. Shown are the differences between the experiment and ideal digital evolution (solid lines), experiment and ideal continuous evolution (dashed), and between the ideal digital and continuous evolutions (dotted).

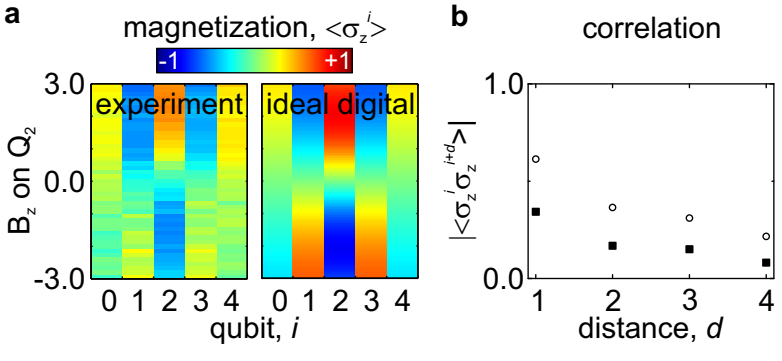

FIGURE S7: **Lifting degeneracy of a five-spin antiferromagnetic state.** Antiferromagnetic ($J_{zz} = -2$) problem with a tunable local field on qubit 3. (a) Single qubit magnetization $< \sigma^z >$ as a function of magnetic field for the experiment (left), and ideal digital evolution (right). (b) Mean experimental (closed) and theory (open) spin parity correlation versus distance. The absolute value shows the long-range correlations.

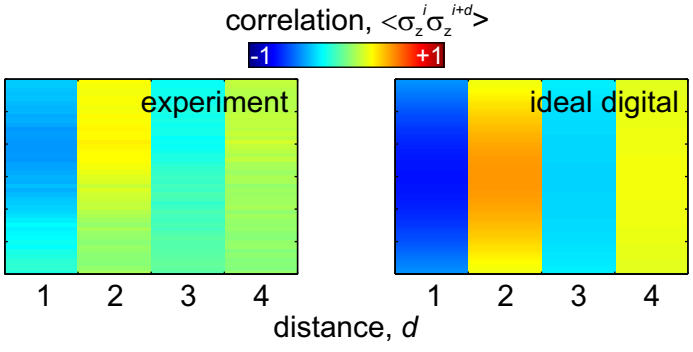

FIGURE S8: **Spin parity correlations in the antiferromagnetic state during lifting of degeneracy.** Left: Experimental data. Right: Ideal digitized evolution.

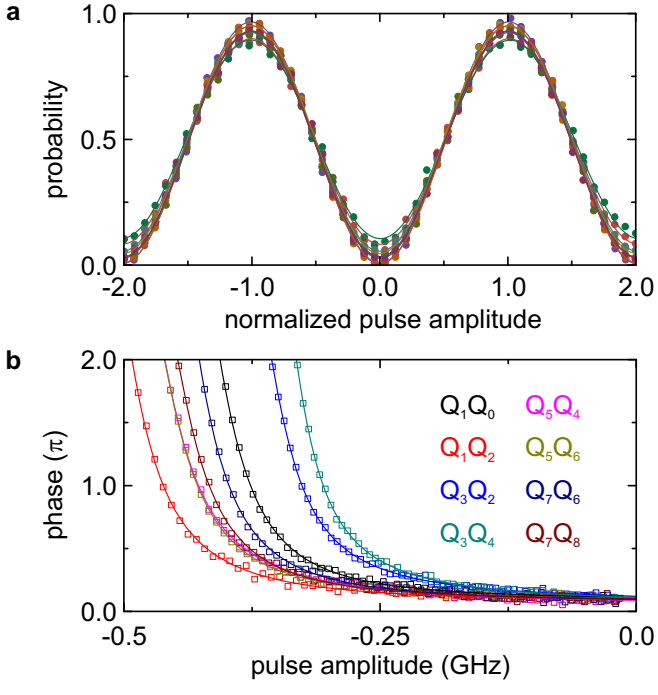

FIGURE S9: **Gate calibrations.** (a) Microwave rotation pulse calibrations for all nine qubits. Pulse amplitude is normalized to the amplitude of a π-pulse. Solid lines are fits to the data. Colours are linked to Fig. 4.8b in Chapter 4. (b) Controllable phase ϕ of the CZ_ϕ gate versus qubit detuning for all eight adjacent pairs. The difference between the curves is due to the qubits having different setpoints in frequency. Solid lines are fits to the data.

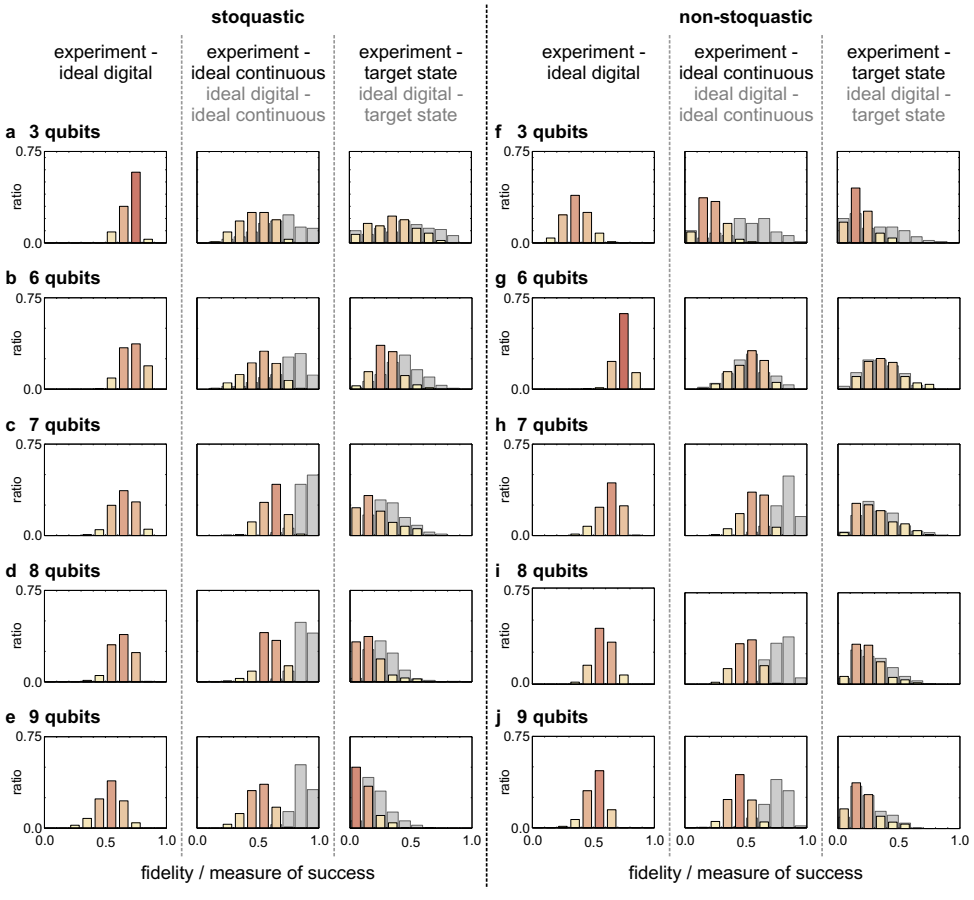

FIGURE S10: **Fidelity overview for the random stoquastic and non-stoquastic problems.** Here, we show normalized histograms of fidelities and measures of success for all experiments for both stoquastic and non-stoquastic problems. For each case we plot three histograms: On the left, we plot the fidelity of the experimental results with respect to the ideal digital evolution. In the middle, in colour we plot the fidelity of the experimental results with respect to the ideal, continuous time evolution for finite time. In the same figure, we plot in gray the fidelity of the ideal digital results with respect to the continuous, finite time evolution. On the right, we plot in colour the fidelity of the experimental results with respect to the ideal adiabatic evolution, and in gray the fidelity of the ideal digital results with respect to the ideal adiabatic evolution. (a, b, c, d, e) Results for random stoquastic problems with three, six, seven, eight and nine qubits. (f, g, h, i, j) Results for random non-stoquastic problems with three, six, seven, eight and nine qubits.

Appendix C

Aspects of Genetic Algorithms for Digital Quantum Simulations

In this Appendix, we discuss details useful for the understanding of the main results of Chapter 5.

C.1 Description of the Genetic Algorithm

In this section, we describe the GA [62, 140] used to obtain the decomposition of the local Trotter blocks [19, 21]. The sequence of quantum gates is codified in a matrix representing in the protocol the genetic code of an individual. This matrix contains as many columns (genes) as allowed resources, and sufficient rows to determine the type of gate and the qubits on which it acts. The next step is to engineer a fitness or evaluation function which maps every individual into a real number. This allows to classify the individuals with respect to an adequate criterion for the optimization purposes. In our case, the fitness function corresponds to the fidelity with respect

to the ideal block dynamics. Finally, each cycle of the algorithm consists of three stages: breeding, mutation, and natural selection.

In the breeding stage, a new generation of individuals is obtained by combining the genetic code of the predecessors, which provides the genetic code of the offspring. We have used a hierarchical combination method, which allows the number of broods of each individual to depend on its fidelity. In particular, for an initial population of 4 individuals sorted by fidelity, our algorithm creates an offspring of 9, 6 of which acquire genetic material of the first precursor, 5 of the second, 4 of the third, and 3 of the fourth. Notice that each newborn individual is produced with the genetic information of two predecessors, as it can be seen from the fact that adding the numbers of each progeny equals two times the number of newborn individuals. Notice that this is not the most general situation, since we could have considered individuals as a combination of more predecessors. Additionally, the amount of genes each precursor provides, in this case the number of matrix columns, also depends on the hierarchy induced by fidelity.

In the mutation stage, every individual is allowed to mutate by randomly modifying any sequence of genetic material, with equal probability for all individuals. This probability settles the threshold to overcome for a random number for a mutation event to occur, case in which another set of random numbers provides the new genes to insert in the genetic material.

In the last stage of the cycle, old and new generations of individuals are combined in the same population group. Afterwards, they are sorted depending on their fidelity, and those which show the highest fidelity are selected as the initial population of the forthcoming cycle.

We have observed that it is convenient to combine numerical trials with high and low mutation rates to enhance the breeding or the mutation stages depending on the intermediate results.

C.2 Number of Architectures

We derive here the formula $P = (q^2 - q)^n n!$ for the number of architectures in terms of the number of ancillary qubits q and the number of imperfect gates n. We impose the condition of applying each two-qubit gate once and only once, and that the gates are asymmetric, so applying it to qubits (i, j) is different to apply it to qubits (j, i). Therefore, one of the q qubits is selected as the control, and one of the remaining $q - 1$ as the target. This process is repeated for each of the n gates, so we obtain $(q(q-1))^n$ possibilities. Finally, the n gates may be applied in any possible order, so there are $n!$ re-orderings. Therefore, by combining both results, the number of total architectures turns into $n!\,(q^2 - q)^n$.

C.3 Errors in Architectures Building the CNOT Gate

We compare the mean error of the integrated CNOT gate obtained with GA over many realizations of imperfect gates with the average of the highest fidelity imperfect CNOT gate involved in the architecture. For this purpose, we take a sampling of 1000 different experiments, and we average the error of the best gate. We estimate the error of the integrated CNOT and obtain the percentage of improvement in the error. These results are summarized in Table S1 for the cases studied in the main manuscript. As it is shown, the probability to have a high-fidelity gate is increased when the number of gates is aucmented. Accordingly, there are more possible architectures that minimize the error in the integrated CNOT. For the case of $q = 5$ and $n = 7$, we obtain similar errors to the ones for $q = 4$. This could well be because the number of ancillary qubits is of the same order of the involved gates, and then no measurable improvement is expected since there is no cancellation of gate errors. Nevertheless, the optimal relation between number qubits and involved gates is still an open question.

TABLE S1: Average errors of integrated CNOTs and highest fidelity CNOT gates for the protocols involving q qubits and n gates.

Errors \ (q,n)	$(4,3)$	$(4,5)$	$(4,7)$	$(5,7)$
Error of best gate	0.1271	0.1205	0.1150	0.1150
Error of architecture	0.1771	0.0988	0.0807	0.0810
Approximate gain	-39%	18%	30%	30%

Bibliography

If I have seen further than others, it is by standing upon the shoulders of giants.

Isaac Newton

[1] R. P. Feynman, *"Simulating physics with computers",* International Journal of Theoretical Physics **21**, 467–488 (1982).

[2] M. A. Nielsen and I. L. Chuang, *Quantum Computation and Quantum Information.* Cambridge University Press, Cambridge, 2010.

[3] P. W. Shor, *"Polynomial-Time Algorithms for Prime Factorization and Discrete Logarithms on a Quantum Computer",* SIAM Review **41**, 303–332 (1999).

[4] L. K. Grover, *"A fast quantum mechanical algorithm for database search",* in *Proceedings of the twenty-eighth annual ACM symposium on Theory of computing - STOC '96*, pp. 212–219. ACM Press, New York, New York, USA, 1996.

[5] I. M. Georgescu, S. Ashhab, and F. Nori, *"Quantum simulation",* Reviews of Modern Physics **86**, 153–185 (2014).

[6] P. Jordan and E. Wigner, *"Über das Paulische Äquivalenzverbot",* Zeitschrift für Physik **47**, 631–651 (1928).

[7] S. B. Bravyi and A. Y. Kitaev, *"Fermionic Quantum Computation",* Annals of Physics **298**, 210–226 (2002).

[8] A. A. Houck, H. E. Türeci, and J. Koch, *"On-chip quantum simulation with superconducting circuits",* Nature Physics **8**, 292–299 (2012).

[9] R. Gerritsma, G. Kirchmair, F. Zähringer, E. Solano, R. Blatt, and C. F. Roos, *"Quantum simulation of the Dirac equation",* Nature **463**, 68–71 (2010).

[10] K. Kim, M.-S. Chang, S. Korenblit, R. Islam, E. E. Edwards, J. K. Freericks, G.-D. Lin, L.-M. Duan, and C. Monroe, *"Quantum simulation of frustrated Ising spins with trapped ions",* Nature **465**, 590–593 (2010).

[11] M. Greiner, O. Mandel, T. Esslinger, T. W. Hänsch, and I. Bloch, *"Quantum phase transition from a superfluid to a Mott insulator in a gas of ultracold atoms",* Nature **415**, 39–44 (2002).

[12] I. Bloch, J. Dalibard, and S. Nascimbène, *"Quantum simulations with ultracold quantum gases",* Nature Physics **8**, 267–276 (2012).

[13] P. W. Shor, *"Scheme for reducing decoherence in quantum computer memory",* Physical Review A **52**, R2493–R2496 (1995).

[14] A. M. Steane, *"Error Correcting Codes in Quantum Theory",* Physical Review Letters **77**, 793–797 (1996).

[15] S. L. Braunstein, *"Quantum error correction for communication with linear optics",* Nature **394**, 47–49 (1998).

[16] J. Chiaverini, D. Leibfried, T. Schaetz, M. D. Barrett, R. B. Blakestad, J. Britton, W. M. Itano, J. D. Jost, E. Knill, C. Langer, R. Ozeri, and D. J. Wineland, *"Realization of quantum error correction",* Nature **432**, 602–605 (2004).

[17] R. Barends, J. Kelly, A. Megrant, A. Veitia, D. Sank, E. Jeffrey, T. C. White, J. Mutus, A. G. Fowler, B. Campbell, Y. Chen, Z. Chen, B. Chiaro, A. Dunsworth, C. Neill, P. O'Malley, P. Roushan, A. Vainsencher, J. Wenner, A. N. Korotkov, A. N. Cleland, and J. M. Martinis, *"Superconducting*

quantum circuits at the surface code threshold for fault tolerance", Nature **508**, 500–503 (2014).

[18] D. Ristè, S. Poletto, M.-Z. Huang, A. Bruno, V. Vesterinen, O.-P. Saira, and L. DiCarlo, *"Detecting bit-flip errors in a logical qubit using stabilizer measurements",* Nature Communications **6**, 6983 (2015).

[19] S. Lloyd, *"Universal Quantum Simulators",* Science **273**, 1073–1078 (1996).

[20] H. F. Trotter, *"On the product of semi-groups of operators",* Proceedings of the American Mathematical Society **10**, 545–545 (1959).

[21] M. Suzuki, *"Fractal decomposition of exponential operators with applications to many-body theories and Monte Carlo simulations",* Physics Letters A **146**, 319–323 (1990).

[22] N. Wiebe, D. Berry, P. Høyer, and B. C. Sanders, *"Higher order decompositions of ordered operator exponentials",* Journal of Physics A: Mathematical and Theoretical **43**, 065203 (2010).

[23] B. P. Lanyon, C. Hempel, D. Nigg, M. Muller, R. Gerritsma, F. Zahringer, P. Schindler, J. T. Barreiro, M. Rambach, G. Kirchmair, M. Hennrich, P. Zoller, R. Blatt, and C. F. Roos, *"Universal Digital Quantum Simulation with Trapped Ions",* Science **334**, 57–61 (2011).

[24] Y. Salathé, M. Mondal, M. Oppliger, J. Heinsoo, P. Kurpiers, A. Potočnik, A. Mezzacapo, U. Las Heras, L. Lamata, E. Solano, S. Filipp, and A. Wallraff, *"Digital Quantum Simulation of Spin Models with Circuit Quantum Electrodynamics",* Physical Review X **5**, 021027 (2015).

[25] R. Barends, L. Lamata, J. Kelly, L. García-Álvarez, A. G. Fowler, A. Megrant, E. Jeffrey, T. C. White, D. Sank, J. Y. Mutus, B. Campbell, Y. Chen, Z. Chen, B. Chiaro, A. Dunsworth, I.-C. Hoi, C. Neill, P. J. J. O'Malley, C. Quintana, P. Roushan, A. Vainsencher, J. Wenner, E. Solano, and J. M. Martinis, *"Digital quantum simulation of fermionic models with a superconducting circuit",* Nature Communications **6**, 7654 (2015).

[26] R. Barends, A. Shabani, L. Lamata, J. Kelly, A. Mezzacapo, U. Las Heras, R. Babbush, A. G. Fowler, B. Campbell, Y. Chen, Z. Chen, B. Chiaro,

A. Dunsworth, E. Jeffrey, E. Lucero, A. Megrant, J. Y. Mutus, M. Neeley, C. Neill, P. J. J. O'Malley, C. Quintana, P. Roushan, D. Sank, A. Vainsencher, J. Wenner, T. C. White, E. Solano, H. Neven, and J. M. Martinis, *"Digitized adiabatic quantum computing with a superconducting circuit",* Nature **534**, 222–226 (2016).

[27] A. Mezzacapo, U. Las Heras, J. S. Pedernales, L. DiCarlo, E. Solano, and L. Lamata, *"Digital Quantum Rabi and Dicke Models in Superconducting Circuits",* Scientific Reports **4**, 7482 (2014).

[28] I. Arrazola, J. S. Pedernales, L. Lamata, and E. Solano, *"Digital-Analog Quantum Simulation of Spin Models in Trapped Ions",* Scientific Reports **6**, 30534 (2016).

[29] N. K. Langford, R. Sagastizabal, M. Kounalakis, C. Dickel, A. Bruno, F. Luthi, D. J. Thoen, A. Endo, and L. DiCarlo, *"Experimentally simulating the dynamics of quantum light and matter at ultrastrong coupling",* arXiv preprint 1610.10065 (2016).

[30] M. H. Devoret and R. J. Schoelkopf, *"Superconducting Circuits for Quantum Information: An Outlook",* Science **339**, 1169–1174 (2013).

[31] L. DiCarlo, J. M. Chow, J. M. Gambetta, L. S. Bishop, B. R. Johnson, D. I. Schuster, J. Majer, A. Blais, L. Frunzio, S. M. Girvin, and R. J. Schoelkopf, *"Demonstration of two-qubit algorithms with a superconducting quantum processor",* Nature **460**, 240–244 (2009).

[32] L. Steffen, Y. Salathe, M. Oppliger, P. Kurpiers, M. Baur, C. Lang, C. Eichler, G. Puebla-Hellmann, A. Fedorov, and A. Wallraff, *"Deterministic quantum teleportation with feed-forward in a solid state system",* Nature **500**, 319–322 (2013).

[33] T. Niemczyk, F. Deppe, H. Huebl, E. P. Menzel, F. Hocke, M. J. Schwarz, J. J. Garcia-Ripoll, D. Zueco, T. Hümmer, E. Solano, A. Marx, and R. Gross, *"Circuit quantum electrodynamics in the ultrastrong-coupling regime",* Nature Physics **6**, 772–776 (2010).

[34] P. Forn-Díaz, J. Lisenfeld, D. Marcos, J. J. García-Ripoll, E. Solano, C. J. P. M. Harmans, and J. E. Mooij, *"Observation of the Bloch-Siegert Shift in a Qubit-Oscillator System in the Ultrastrong Coupling Regime",* Physical Review Letters **105**, 237001 (2010).

[35] J. Casanova, G. Romero, I. Lizuain, J. J. García-Ripoll, and E. Solano, *"Deep Strong Coupling Regime of the Jaynes-Cummings Model",* Physical Review Letters **105**, 263603 (2010).

[36] F. Yoshihara, T. Fuse, S. Ashhab, K. Kakuyanagi, S. Saito, and K. Semba, *"Superconducting qubitoscillator circuit beyond the ultrastrong-coupling regime",* Nature Physics (2016).

[37] A. Blais, R.-S. Huang, A. Wallraff, S. M. Girvin, and R. J. Schoelkopf, *"Cavity quantum electrodynamics for superconducting electrical circuits: An architecture for quantum computation",* Physical Review A **69**, 062320 (2004).

[38] I. Chiorescu, P. Bertet, K. Semba, Y. Nakamura, C. J. P. M. Harmans, and J. E. Mooij, *"Coherent dynamics of a flux qubit coupled to a harmonic oscillator",* Nature **431**, 159–162 (2004).

[39] A. Wallraff, D. I. Schuster, A. Blais, L. Frunzio, R.-S. Huang, J. Majer, S. Kumar, S. M. Girvin, and R. J. Schoelkopf, *"Strong coupling of a single photon to a superconducting qubit using circuit quantum electrodynamics",* Nature **431**, 162–167 (2004).

[40] V. Bouchiat, D. Vion, P. Joyez, D. Esteve, and M. H. Devoret, *"Quantum coherence with a single Cooper pair",* Physica Scripta **1998**, 165 (1998).

[41] Y. Nakamura, Y. A. Pashkin, and J. S. Tsai, *"Coherent control of macroscopic quantum states in a single-Cooper-pair box",* Nature **398**, 786–788 (1999).

[42] J. E. Mooij, T. P. Orlando, L. Levitov, L. Tian, C. H. der Wal, and S. Lloyd, *"Josephson persistent-current qubit",* Science **285**, 1036–1039 (1999).

[43] J. M. Martinis, S. Nam, J. Aumentado, and C. Urbina, *"Rabi oscillations in a large Josephson-junction qubit",* Physical Review Letters **89**, 117901 (2002).

[44] D. Vion, *"Manipulating the Quantum State of an Electrical Circuit",* Science **296**, 886–889 (2002).

[45] J. Koch, T. M. Yu, J. Gambetta, A. A. Houck, D. I. Schuster, J. Majer, A. Blais, M. H. Devoret, S. M. Girvin, and R. J. Schoelkopf, *"Charge-insensitive qubit design derived from the Cooper pair box",* Physical Review A **76**, 042319 (2007).

[46] V. E. Manucharyan, J. Koch, L. I. Glazman, and M. H. Devoret, *"Fluxonium: Single Cooper-Pair Circuit Free of Charge Offsets",* Science **326**, 113–116 (2009).

[47] M. Steffen, S. Kumar, D. P. DiVincenzo, J. R. Rozen, G. A. Keefe, M. B. Rothwell, and M. B. Ketchen, *"High-Coherence Hybrid Superconducting Qubit",* Physical Review Letters **105**, 100502 (2010).

[48] A. Lupascu, S. Saito, T. Picot, P. C. de Groot, C. J. P. M. Harmans, and J. E. Mooij, *"Quantum non-demolition measurement of a superconducting two-level system",* Nature Physics **3**, 119–125 (2007).

[49] S. Sachdev, *Quantum Phase Transitions.* Cambridge University Press, Cambridge, England, 1999.

[50] H. M. Ronnow, *"Quantum Phase Transition of a Magnet in a Spin Bath",* Science **308**, 389–392 (2005).

[51] A. Georges, G. Kotliar, W. Krauth, and M. J. Rozenberg, *"Dynamical mean-field theory of strongly correlated fermion systems and the limit of infinite dimensions",* Reviews of Modern Physics **68**, 13–125 (1996).

[52] I. I. Rabi, *"On the Process of Space Quantization",* Physical Review **49**, 324–328 (1936).

[53] E. T. Jaynes and F. W. Cummings, *"Comparison of quantum and semiclassical radiation theories with application to the beam maser",* Proceedings of the IEEE **51**, 89–109 (1963).

[54] R. H. Dicke, *"Coherence in Spontaneous Radiation Processes",* Physical Review **93**, 99–110 (1954).

[55] M. Tavis and F. W. Cummings, *"Exact solution for an N-molecule-radiation-field Hamiltonian",* Physical Review **170**, 379–384 (1968).

[56] D. Braak, *"Integrability of the Rabi Model",* Physical Review Letters **107**, 100401 (2011).

[57] A. J. Leggett, S. Chakravarty, A. T. Dorsey, M. P. A. Fisher, A. Garg, and W. Zwerger, *"Dynamics of the dissipative two-state system",* Reviews of Modern Physics **59**, 1 (1987).

[58] D. Porras and J. I. Cirac, *"Bose-Einstein Condensation and Strong-Correlation Behavior of Phonons in Ion Traps",* Physical Review Letters **93**, 263602 (2004).

[59] K. Seo and L. Tian, *"Quantum phase transition in a multiconnected superconducting Jaynes-Cummings lattice",* Physical Review B **91**, 195439 (2015).

[60] Y. Zhang, L. Yu, J. Q. Liang, G. Chen, S. Jia, and F. Nori, *"Quantum phases in circuit QED with a superconducting qubit array",* Scientific Reports **4**, 064509 (2014).

[61] E. J. Pritchett, C. Benjamin, A. Galiautdinov, M. R. Geller, A. T. Sornborger, P. C. Stancil, and J. M. Martinis, *"Quantum Simulation of Molecular Collisions with Superconducting Qubits",* arXiv preprint 1008.0701 (2010).

[62] E. Alpaydin, *Introduction to Machine Learning.* MIT, Cambridge, MA, 3 ed., 2014.

[63] B. Gross, *"A solar energy system that tracks the sun",* TED talk (2003).

[64] G. S. Hornby, A. Globus, D. S. Linden, and J. D. Lohn, *Collection of Technical Papers of the Space 2006 Conference.* American Institute of Aeronautics and Astronautics, Inc., Reston, 2006.

[65] T. Geijtenbeek, M. van de Panne, and A. F. van der Stappen, *"Flexible muscle-based locomotion for bipedal creatures",* ACM Transactions on Graphics **32**, 1–11 (2013).

[66] R. S. Zebulum, M. A. C. Pacheco, and M. M. B. R. Vellasco, *Evolutionary electronics, automatic design of electronic circuits and systems by genetic algorithms.* CRC Press, Boca Raton, FL, 2002.

[67] W. M. Aly, *"Analog electric circuits synthesis using a genetic algorithms approach",* Int. J. Comput. Appl. **121**, 28 (2015).

[68] N. Spagnolo, E. Maiorino, C. Vitelli, M. Bentivegna, A. Crespi, R. Ramponi, P. Mataloni, R. Osellame, and F. Sciarrino, *"Learning an unknown transformation via a genetic approach",* arXiv preprint 1610.03291 (2016).

[69] J. Bang and S. Yoo, *"A genetic-algorithm-based method to find unitary transformations for any desired quantum computation and application to a one-bit oracle decision problem",* Journal of the Korean Physical Society **65**, 2001–2008 (2014).

[70] A. Fedorov, L. Steffen, M. Baur, M. P. da Silva, and A. Wallraff, *"Implementation of a Toffoli gate with superconducting circuits",* Nature **481**, 170–172 (2011).

[71] A. A. Abdumalikov Jr, J. M. Fink, K. Juliusson, M. Pechal, S. Berger, A. Wallraff, and S. Filipp, *"Experimental realization of non-Abelian non-adiabatic geometric gates",* Nature **496**, 482–485 (2013).

[72] J. M. Chow, J. M. Gambetta, A. D. Córcoles, S. T. Merkel, J. A. Smolin, C. Rigetti, S. Poletto, G. A. Keefe, M. B. Rothwell, J. R. Rozen, M. B. Ketchen, and M. Steffen, *"Universal Quantum Gate Set Approaching Fault-Tolerant Thresholds with Superconducting Qubits",* Physical Review Letters **109**, 060501 (2012).

[73] M. Neeley, R. C. Bialczak, M. Lenander, E. Lucero, M. Mariantoni, A. D. O'Connell, D. Sank, H. Wang, M. Weides, J. Wenner, Y. Yin, T. Yamamoto, A. N. Cleland, and J. M. Martinis, *"Generation of three-qubit entangled states using superconducting phase qubits",* Nature **467**, 570–573 (2010).

[74] M. D. Reed, L. DiCarlo, S. E. Nigg, L. Sun, L. Frunzio, S. M. Girvin, and R. J. Schoelkopf, *"Realization of three-qubit quantum error correction with superconducting circuits",* Nature **482**, 382–385 (2012).

[75] J. J. García-Ripoll, E. Solano, and M. A. Martin-Delgado, *"Quantum simulation of Anderson and Kondo lattices with superconducting qubits",* Physical Review B **77**, 024522 (2008).

[76] L. Tian, *"Circuit QED and Sudden Phase Switching in a Superconducting Qubit Array",* Physical Review Letters **105**, 167001 (2010).

[77] F. Mei, V. M. Stojanović, I. Siddiqi, and L. Tian, *"Analog superconducting quantum simulator for Holstein polarons",* Physical Review B **88**, 224502 (2013).

[78] D. Ballester, G. Romero, J. J. García-Ripoll, F. Deppe, and E. Solano, *"Quantum Simulation of the Ultrastrong-Coupling Dynamics in Circuit Quantum Electrodynamics",* Physical Review X **2**, 021007 (2012).

[79] J. S. Pedernales, R. Di Candia, D. Ballester, and E. Solano, *"Quantum simulations of relativistic quantum physics in circuit QED",* New Journal of Physics **15**, 055008 (2013).

[80] O. Viehmann, J. von Delft, and F. Marquardt, *"Observing the Nonequilibrium Dynamics of the Quantum Transverse-Field Ising Chain in Circuit QED",* Physical Review Letters **110**, 030601 (2013).

[81] B. P. Lanyon, J. D. Whitfield, G. G. Gillett, M. E. Goggin, M. P. Almeida, I. Kassal, J. D. Biamonte, M. Mohseni, B. J. Powell, M. Barbieri, A. Aspuru-Guzik, and A. G. White, *"Towards quantum chemistry on a quantum computer",* Nature Chemistry **2**, 106–111 (2010).

[82] J. Casanova, A. Mezzacapo, L. Lamata, and E. Solano, *"Quantum Simulation of Interacting Fermion Lattice Models in Trapped Ions",* Physical Review Letters **108**, 190502 (2012).

[83] A. Mezzacapo, J. Casanova, L. Lamata, and E. Solano, *"Digital Quantum Simulation of the Holstein Model in Trapped Ions",* Physical Review Letters **109**, 200501 (2012).

[84] D. W. Berry, G. Ahokas, R. Cleve, and B. C. Sanders, *"Efficient Quantum Algorithms for Simulating Sparse Hamiltonians",* Communications in Mathematical Physics **270**, 359–371 (2007).

[85] S. Chen, L. Wang, S.-J. Gu, and Y. Wang, *"Fidelity and quantum phase transition for the Heisenberg chain with next-nearest-neighbor interaction",* Physical Review E **76**, 061108 (2007).

[86] L. F. Santos, F. Borgonovi, and F. M. Izrailev, *"Chaos and Statistical Relaxation in Quantum Systems of Interacting Particles",* Physical Review Letters **108**, 094102 (2012).

[87] P. W. Anderson, *"The Resonating Valence Bond State in La2CuO4 and Superconductivity",* Science **235**, 1196–1198 (1987).

[88] J. Majer, J. M. Chow, J. M. Gambetta, J. Koch, B. R. Johnson, J. A. Schreier, L. Frunzio, D. I. Schuster, A. A. Houck, A. Wallraff, A. Blais, M. H. Devoret, S. M. Girvin, and R. J. Schoelkopf, *"Coupling superconducting qubits via a cavity bus",* Nature **449**, 443–447 (2007).

[89] S. Filipp, M. Göppl, J. M. Fink, M. Baur, R. Bianchetti, L. Steffen, and A. Wallraff, *"Multimode mediated qubit-qubit coupling and dark-state symmetries in circuit quantum electrodynamics",* Physical Review A **83**, 063827 (2011).

[90] C. Rigetti, J. M. Gambetta, S. Poletto, B. L. T. Plourde, J. M. Chow, A. D. Córcoles, J. A. Smolin, S. T. Merkel, J. R. Rozen, G. A. Keefe, M. B. Rothwell, M. B. Ketchen, and M. Steffen, *"Superconducting qubit in a waveguide cavity with a coherence time approaching 0.1 ms",* Physical Review B **86**, 100506 (2012).

[91] R. Bianchetti, S. Filipp, M. Baur, J. M. Fink, M. Göppl, P. J. Leek, L. Steffen, A. Blais, and A. Wallraff, *"Dynamics of dispersive single-qubit readout in circuit quantum electrodynamics",* Physical Review A **80**, 043840 (2009).

[92] A. Dewes, F. R. Ong, V. Schmitt, R. Lauro, N. Boulant, P. Bertet, D. Vion, and D. Esteve, *"Characterization of a Two-Transmon Processor with Individual Single-Shot Qubit Readout",* Physical Review Letters **108**, 057002 (2012).

[93] G. Vidal and R. F. Werner, *"Computable measure of entanglement",* Physical Review A **65**, 032314 (2002).

[94] U. Las Heras, A. Mezzacapo, L. Lamata, S. Filipp, A. Wallraff, and E. Solano, *"Digital Quantum Simulation of Spin Systems in Superconducting Circuits",* Physical Review Letters **112**, 200501 (2014).

[95] D. Braak, *"Solution of the Dicke model for N = 3",* Journal of Physics B: Atomic, Molecular and Optical Physics **46**, 224007 (2013).

[96] G. Günter, A. A. Anappara, J. Hees, A. Sell, G. Biasiol, L. Sorba, S. De Liberato, C. Ciuti, A. Tredicucci, A. Leitenstorfer, and R. Huber, *"Sub-cycle switch-on of ultrastrong lightmatter interaction",* Nature **458**, 178–181 (2009).

[97] A. Crespi, S. Longhi, and R. Osellame, *"Photonic Realization of the Quantum Rabi Model",* Physical Review Letters **108**, 163601 (2012).

[98] K. Hepp and E. H. Lieb, *"On the superradiant phase transition for molecules in a quantized radiation field: the dicke maser model",* Annals of Physics **76**, 360–404 (1973).

[99] Y. K. Wang and F. T. Hioe, *"Phase Transition in the Dicke Model of Superradiance",* Physical Review A **7**, 831–836 (1973).

[100] H. J. Carmichael, C. W. Gardiner, and D. F. Walls, *"Higher order corrections to the Dicke superradiant phase transition",* Physics Letters A **46**, 47–48 (1973).

[101] R. Blatt and C. F. Roos, *"Quantum simulations with trapped ions",* Nature Physics **8**, 277–284 (2012).

[102] A. Aspuru-Guzik and P. Walther, *"Photonic quantum simulators",* Nature Physics **8**, 285–291 (2012).

[103] A. Blais, J. Gambetta, A. Wallraff, D. I. Schuster, S. M. Girvin, M. H. Devoret, and R. J. Schoelkopf, *"Quantum-information processing with circuit quantum electrodynamics",* Physical Review A **75**, 032329 (2007).

[104] N. Wiebe, D. W. Berry, P. Høyer, and B. C. Sanders, *"Simulating quantum dynamics on a quantum computer",* Journal of Physics A: Mathematical and Theoretical **44**, 445308 (2011).

[105] R. Di Candia, E. P. Menzel, L. Zhong, F. Deppe, A. Marx, R. Gross, and E. Solano, *"Dual-path methods for propagating quantum microwaves",* New Journal of Physics **16**, 15001 (2014).

[106] L. Lamata, J. León, T. Schätz, and E. Solano, *"Dirac Equation and Quantum Relativistic Effects in a Single Trapped Ion",* Physical Review Letters **98**, 253005 (2007).

[107] M. Lewenstein, A. Sanpera, V. Ahufinger, B. Damski, A. Sen, and U. Sen, *"Ultracold atomic gases in optical lattices: mimicking condensed matter physics and beyond",* Advances in Physics **56**, 243–379 (2007).

[108] J. Koch, A. A. Houck, K. L. Hur, and S. M. Girvin, *"Time-reversal-symmetry breaking in circuit-QED-based photon lattices",* Physical Review A **82**, 043811 (2010).

[109] A. van Oudenaarden and J. E. Mooij, *"One-Dimensional Mott Insulator Formed by Quantum Vortices in Josephson Junction Arrays",* Physical Review Letters **76**, 4947–4950 (1996).

[110] P. Rotondo, M. Cosentino Lagomarsino, and G. Viola, *"Dicke Simulators with Emergent Collective Quantum Computational Abilities",* Physical Review Letters **114**, 143601 (2015).

[111] J. Q. You, X.-F. Shi, X. Hu, and F. Nori, *"Quantum emulation of a spin system with topologically protected ground states using superconducting quantum circuits",* Physical Review B **81**, 014505 (2010).

[112] S. Mostame, J. Huh, C. Kreisbeck, A. J. Kerman, T. Fujita, A. Eisfeld, and A. Aspuru-Guzik, *"Towards Outperforming Classical Algorithms with Analog Quantum Simulators",* arXiv preprint 1502.00962 (2015).

[113] A. Chiesa, P. Santini, D. Gerace, J. Raftery, A. A. Houck, and S. Carretta, *"Digital quantum simulators in a scalable architecture of hybrid spin-photon qubits",* Scientific Reports **5**, 16036 (2015).

[114] U. Las Heras, L. García-Álvarez, A. Mezzacapo, E. Solano, and L. Lamata, *"Quantum simulation of spin chains coupled to bosonic modes with superconducting circuits",* in *Mathematics for Industry 11*, R. S. Anderssen, P. Broadbridge, Y. Fukumoto, K. Kajiwara, T. Takagi, E. Verbitskiy, and M. Wakayama, eds. Springer, Japan, 2015.

[115] M. R. Geller, J. M. Martinis, A. T. Sornborger, P. C. Stancil, E. J. Pritchett, and A. Galiautdinov, *"Universal quantum simulation with pre-threshold superconducting qubits: Single-excitation subspace method",* EPJ Quantum Technology **2**, 8 (2012).

[116] E. Farhi, J. Goldstone, S. Gutmann, and M. Sipser, *"Quantum Computation by Adiabatic Evolution",* arXiv preprint quant–ph/0001106 (2000).

[117] E. Farhi, J. Goldstone, S. Gutmann, J. Lapan, A. Lundgren, and D. Preda, *"A quantum adiabatic evolution algorithm applied to random instances of an NP-complete problem",* Science **292**, 472–475 (2001).

[118] H. Nishimori, *Statistical Physics of Spin Glasses and Information Processing: An Introduction.* Oxford Univ. Press, Statistical Physics of Spin Glasses and Information Processing: An Introduction (Oxford Univ. Press, 2001)., 2001.

[119] S. B. Bravyi and A. Y. Kitaev, *"Quantum codes on a lattice with boundary",* arXiv preprint quant–ph/9811052 (1998).

[120] A. G. Fowler, M. Mariantoni, J. M. Martinis, and A. N. Cleland, *"Surface codes: towards practical large-scale quantum computation",* Phys. Rev. A **86**, 32324 (2012).

[121] S. Lloyd and B. M. Terhal, *"Adiabatic and Hamiltonian computing on a 2D lattice with simple two-qubit interactions",* New Journal of Physics **18**, 023042 (2016).

[122] E. Crosson, E. Farhi, C. Y.-Y. Lin, H.-H. Lin, and P. Shor, *"Different Strategies for Optimization Using the Quantum Adiabatic Algorithm",* arXiv preprint 1401.7320 (2014).

[123] R. Babbush, P. J. Love, and A. Aspuru-Guzik, *"Adiabatic Quantum Simulation of Quantum Chemistry",* Scientific Reports **4**, 6603 (2014).

[124] M. Troyer and U.-J. Wiese, *"Computational Complexity and Fundamental Limitations to Fermionic Quantum Monte Carlo Simulations",* Physical Review Letters **94**, 170201 (2005).

[125] S. Boixo, V. N. Smelyanskiy, A. Shabani, S. V. Isakov, M. Dykman, V. S. Denchev, M. H. Amin, A. Y. Smirnov, M. Mohseni, and H. Neven, *"Computational multiqubit tunnelling in programmable quantum annealers",* Nature Communications **7**, 10327 (2016).

[126] J. T. Seeley, M. J. Richard, and P. J. Love, *"The Bravyi-Kitaev transformation for quantum computation of electronic structure",* The Journal of Chemical Physics **137**, 224109 (2012).

[127] W. van Dam, M. Mosca, and U. Vazirani, *"How powerful is adiabatic quantum computation?",* in *Proceedings 2001 IEEE International Conference on Cluster Computing*, pp. 279–287. IEEE Comput. Soc, 2002.

[128] M. Born and V. Fock, *"Beweis des Adiabatensatzes",* Zeitschrift für Physik **51**, 165–180 (1928).

[129] D. Aharonov, W. van Dam, J. Kempe, Z. Landau, S. Lloyd, and O. Regev, *"Adiabatic Quantum Computation Is Equivalent to Standard Quantum Computation",* SIAM Review **50**, 755–787 (2008).

[130] A. Mezzacapo, L. Lamata, S. Filipp, and E. Solano, *"Many-Body Interactions with Tunable-Coupling Transmon Qubits",* Physical Review Letters **113**, 050501 (2014).

[131] L. García-Álvarez, J. Casanova, A. Mezzacapo, I. L. Egusquiza, L. Lamata, G. Romero, and E. Solano, *"Fermion-Fermion Scattering in Quantum Field Theory with Superconducting Circuits",* Physical Review Letters **114**, 070502 (2015).

[132] M.-H. Yung, J. Casanova, A. Mezzacapo, J. McClean, L. Lamata, A. Aspuru-Guzik, and E. Solano, *"From transistor to trapped-ion computers for quantum chemistry",* Scientific Reports **4**, 3589 (2014).

[133] D. Poulin, M. B. Hastings, D. Wecker, N. Wiebe, A. C. Doherty, and M. Troyer, *"The Trotter Step Size Required for Accurate Quantum Simulation of Quantum Chemistry",* Quantum Information and Computation **15**, 361 (2015).

[134] U. Las Heras, L. García-Álvarez, A. Mezzacapo, E. Solano, and L. Lamata, *"Fermionic models with superconducting circuits",* EPJ Quantum Technology **2**, 8 (2015).

[135] M. Steffen, W. van Dam, T. Hogg, G. Breyta, and I. Chuang, *"Experimental Implementation of an Adiabatic Quantum Optimization Algorithm",* Physical Review Letters **90**, 067903 (2003).

[136] R. Barends, J. Kelly, A. Megrant, D. Sank, E. Jeffrey, Y. Chen, Y. Yin, B. Chiaro, J. Mutus, C. Neill, P. O'Malley, P. Roushan, J. Wenner, T. C. White, A. N. Cleland, and J. M. Martinis, *"Coherent Josephson Qubit Suitable for Scalable Quantum Integrated Circuits",* Physical Review Letters **111**, 080502 (2013).

[137] J. Kelly, R. Barends, A. G. Fowler, A. Megrant, E. Jeffrey, T. C. White, D. Sank, J. Y. Mutus, B. Campbell, Y. Chen, Others, Z. Chen, B. Chiaro, A. Dunsworth, I.-C. Hoi, C. Neill, P. J. J. O'Malley, C. Quintana, P. Roushan, A. Vainsencher, J. Wenner, A. N. Cleland, and J. M. Martinis, *"State preservation by repetitive error detection in a superconducting quantum circuit",* Nature **519**, 66–69 (2015).

[138] T. W. B. Kibble, *"Some implications of a cosmological phase transition",* Physics Reports **67**, 183–199 (1980).

[139] D. W. Berry, A. M. Childs, R. Cleve, R. Kothari, and R. D. Somma, *"Simulating Hamiltonian Dynamics with a Truncated Taylor Series",* Physical Review Letters **114**, 090502 (2015).

[140] L. D. Chambers, *Practical Handbook of Genetic Algorithms.* CRC Press, Boca Raton, FL, 1998.

[141] D. Deutsch, *"Quantum Theory, the Church-Turing Principle and the Universal Quantum Computer",* Proceedings of the Royal Society of London A: Mathematical, Physical and Engineering Sciences **400**, 97–117 (1985).

[142] U. Alvarez-Rodriguez, M. Sanz, L. Lamata, and E. Solano, *"Biomimetic Cloning of Quantum Observables",* Scientific Reports **4**, 467–488 (2014).

[143] U. Alvarez-Rodriguez, M. Sanz, L. Lamata, and E. Solano, *"Artificial Life in Quantum Technologies",* Scientific Reports **6**, 20956 (2016).

[144] R. Sweke, M. Sanz, I. Sinayskiy, F. Petruccione, and E. Solano, *"Digital quantum simulation of many-body non-Markovian dynamics",* Physical Review A **94**, 022317 (2016).

[145] G. C. Knee and W. J. Munro, *"Optimal Trotterization in universal quantum simulators under faulty control",* Physical Review A **91**, 052327 (2015).

[146] L. García-Álvarez, U. Las Heras, A. Mezzacapo, M. Sanz, E. Solano, and L. Lamata, *"Quantum chemistry and charge transport in biomolecules with superconducting circuits",* Scientific Reports **6**, 27836 (2016).

[147] V. Nebendahl, H. Häffner, and C. F. Roos, *"Optimal control of entangling operations for trapped-ion quantum computing",* Physical Review A **79**, 012312 (2009).

[148] T. Choi, S. Debnath, T. A. Manning, C. Figgatt, Z.-X. Gong, L.-M. Duan, and C. Monroe, *"Optimal Quantum Control of Multimode Couplings between Trapped Ion Qubits for Scalable Entanglement",* Physical Review Letters **112**, 190502 (2014).

[149] S. Machnes, U. Sander, S. J. Glaser, P. de Fouquières, A. Gruslys, S. Schirmer, and T. Schulte-Herbrüggen, *"Comparing, optimizing, and benchmarking quantum-control algorithms in a unifying programming framework",* Physical Review A **84**, 022305 (2011).

[150] C. Eichler, Y. Salathe, J. Mlynek, S. Schmidt, and A. Wallraff, *"Quantum-Limited Amplification and Entanglement in Coupled Nonlinear Resonators",* Physical Review Letters **113**, 110502 (2014).

[151] F. Motzoi, J. M. Gambetta, P. Rebentrost, and F. K. Wilhelm, *"Simple Pulses for Elimination of Leakage in Weakly Nonlinear Qubits",* Physical Review Letters **103**, 110501 (2009).

[152] J. M. Gambetta, F. Motzoi, S. T. Merkel, and F. K. Wilhelm, *"Analytic control methods for high-fidelity unitary operations in a weakly nonlinear oscillator",* Physical Review A **83**, 012308 (2011).

[153] L. M. K. Vandersypen and I. L. Chuang, *"NMR techniques for quantum control and computation",* Reviews of Modern Physics **76**, 1037–1069 (2005).

[154] S. Filipp, P. Maurer, P. J. Leek, M. Baur, R. Bianchetti, J. M. Fink, M. Göppl, L. Steffen, J. M. Gambetta, A. Blais, and A. Wallraff, *"Two-Qubit State Tomography Using a Joint Dispersive Readout",* Physical Review Letters **102**, 200402 (2009).

[155] J. F. Poyatos, J. I. Cirac, and P. Zoller, *"Complete Characterization of a Quantum Process: The Two-Bit Quantum Gate",* Physical Review Letters **78**, 390–393 (1997).

[156] I. L. Chuang and M. A. Nielsen, *"Prescription for experimental determination of the dynamics of a quantum black box",* Journal of Modern Optics **44**, 2455–2467 (1997).

[157] A. G. Kofman and A. N. Korotkov, *"Two-qubit decoherence mechanisms revealed via quantum process tomography",* Physical Review A **80**, 042103 (2009).

[158] N. Schuch and J. Siewert, *"Natural two-qubit gate for quantum computation using the <math display="inline"> <mi>XY</mi> </math> interaction",* Physical Review A **67**, 032301 (2003).

[159] T. Wu and L. Ye, *"Implementing Two-Qubit SWAP Gate with SQUID Qubits in a Microwave Cavity via Adiabatic Passage Evolution",* International Journal of Theoretical Physics **51**, 1076–1081 (2012).

[160] A. D. Córcoles, J. M. Gambetta, J. M. Chow, J. A. Smolin, M. Ware, J. Strand, B. L. T. Plourde, and M. Steffen, *"Process verification of two-qubit quantum gates by randomized benchmarking",* Physical Review A **87**, 030301 (2013).

[161] E. Knill, D. Leibfried, R. Reichle, J. Britton, R. B. Blakestad, J. D. Jost, C. Langer, R. Ozeri, S. Seidelin, and D. J. Wineland, *"Randomized benchmarking of quantum gates",* Physical Review A **77**, 012307 (2008).

[162] J. M. Chow, J. M. Gambetta, L. Tornberg, J. Koch, L. S. Bishop, A. A. Houck, B. R. Johnson, L. Frunzio, S. M. Girvin, and R. J. Schoelkopf,

"Randomized Benchmarking and Process Tomography for Gate Errors in a Solid-State Qubit", Physical Review Letters **102**, 090502 (2009).

[163] J. Kelly, R. Barends, B. Campbell, Y. Chen, Z. Chen, B. Chiaro, A. Dunsworth, A. G. Fowler, I.-C. Hoi, E. Jeffrey, A. Megrant, J. Mutus, C. Neill, P. J. J. O'Malley, C. Quintana, P. Roushan, D. Sank, A. Vainsencher, J. Wenner, T. C. White, A. N. Cleland, and J. M. Martinis, *"Optimal Quantum Control Using Randomized Benchmarking",* Physical Review Letters **112**, 240504 (2014).

[164] A. Kitaev, A. Shen, and M. Vyalyi, *Classical and Quantum Computation*, volume 47 of *Graduate Studies in Mathematics*. American Mathematical Society, Providence, Rhode Island, 2002.

[165] A. Mizel, D. A. Lidar, and M. Mitchell, *"Simple Proof of Equivalence between Adiabatic Quantum Computation and the Circuit Model",* Physical Review Letters **99**, 070502 (2007).

[166] V. N. Smelyanskiy, U. v. Toussaint, and D. A. Timucin, *"Dynamics of quantum adiabatic evolution algorithm for Number Partitioning",* arXiv preprint quant–ph/0202155 (2002).

[167] S. Garnerone, P. Zanardi, and D. A. Lidar, *"Adiabatic Quantum Algorithm for Search Engine Ranking",* Physical Review Letters **108**, 230506 (2012).

[168] H. Neven, V. S. Denchev, G. Rose, and W. G. Macready, *"Training a Binary Classifier with the Quantum Adiabatic Algorithm",* arXiv preprint 0811.0416 (2008).

[169] F. Gaitan and L. Clark, *"Ramsey Numbers and Adiabatic Quantum Computing",* Physical Review Letters **108**, 010501 (2012).

[170] A. Lucas, *"Ising formulations of many NP problems",* Frontiers in Physics **2**, 5 (2014).

[171] A. Das and B. K. Chakrabarti, eds., *Quantum Annealing and Other Optimization Methods*, volume 679 of *Lecture Notes in Physics*. Springer Berlin Heidelberg, Berlin, Heidelberg, 2005.

[172] S. W. Shin, G. Smith, J. A. Smolin, and U. Vazirani, *"Comment on "Distinguishing Classical and Quantum Models for the D-Wave Device"",* arXiv preprint 1404.6499 (2014).

[173] I. Zintchenko, M. B. Hastings, and M. Troyer, *"From local to global ground states in Ising spin glasses",* Physical Review B **91**, 024201 (2015).

[174] J. D. Biamonte and P. J. Love, *"Realizable Hamiltonians for universal adiabatic quantum computers",* Physical Review A **78**, 012352 (2008).

[175] S. Bravyi, D. P. DiVincenzo, R. I. Oliveira, and B. M. Terhal, *"The complexity of stoquastic local Hamiltonian problems",* Quantum Inf. Comput. **8**, 361–385 (2008).

[176] T. Cubitt and A. Montanaro, *"Complexity classification of local Hamiltonian problems",* arXiv preprint 1311.3161 (2013).

[177] J. Kempe, A. Kitaev, and O. Regev, *"The Complexity of the Local Hamiltonian Problem",* SIAM Journal on Computing **35**, 1070–1097 (2006).

[178] Y. Cao, R. Babbush, J. Biamonte, and S. Kais, *"Hamiltonian gadgets with reduced resource requirements",* Physical Review A **91**, 012315 (2015).

[179] R. Babbush, B. O'Gorman, and A. Aspuru-Guzik, *"Resource efficient gadgets for compiling adiabatic quantum optimization problems",* Annalen der Physik **525**, 877–888 (2013).

[180] A. M. Childs, E. Farhi, and J. Preskill, *"Robustness of adiabatic quantum computation",* Physical Review A **65**, 012322 (2001).

[181] S. Matsuura, H. Nishimori, T. Albash, and D. A. Lidar, *"Mean Field Analysis of Quantum Annealing Correction",* Physical Review Letters **116**, 220501 (2016).

[182] M. H. S. Amin, C. J. S. Truncik, and D. V. Averin, *"Role of single-qubit decoherence time in adiabatic quantum computation",* Physical Review A **80**, 022303 (2009).

[183] R. Di Candia, B. Mejia, H. Castillo, J. S. Pedernales, J. Casanova, and E. Solano, *"Embedding Quantum Simulators for Quantum Computation of Entanglement",* Physical Review Letters **111**, 240502 (2013).

[184] M. B. Hastings, D. Wecker, B. Bauer, and M. Troyer, *"Improving Quantum Algorithms for Quantum Chemistry",* Quantum Information and Computation **15**, 1–21 (2014).

[185] J. Huyghebaert and H. D. Raedt, *"Product formula methods for time-dependent Schrodinger problems",* Journal of Physics A: Mathematical and General **23**, 5777–5793 (1990).

[186] D. Poulin, A. Qarry, R. Somma, and F. Verstraete, *"Quantum Simulation of Time-Dependent Hamiltonians and the Convenient Illusion of Hilbert Space",* Physical Review Letters **106**, 170501 (2011).

[187] R. Babbush, D. W. Berry, I. D. Kivlichan, A. Y. Wei, P. J. Love, and A. Aspuru-Guzik, *"Exponentially more precise quantum simulation of fermions II: Quantum chemistry in the CI matrix representation",* arXiv preprint 1506.01029 (2015).

[188] W. H. Zurek, U. Dorner, and P. Zoller, *"Dynamics of a Quantum Phase Transition",* Physical Review Letters **95**, 105701 (2005).

[189] T. Caneva, R. Fazio, and G. E. Santoro, *"Quantum annealing of an infinite-range transverse-field Ising model",* Journal of Physics: Conference Series **143**, 012004 (2009).

[190] S. Suzuki, *"Cooling dynamics of pure and random Ising chains",* Journal of Statistical Mechanics: Theory and Experiment **2009**, P03032 (2009).

[191] S. Suzuki, *"Kibble-Zurek mechanism in simulated annealing and quantum annealing",* Journal of Physics: Conference Series **302**, 012046 (2011).

[192] J. M. Martinis and M. R. Geller, *"Fast adiabatic qubit gates using only σ z control",* Physical Review A **90**, 022307 (2014).

[193] P. J. J. O'Malley, J. Kelly, R. Barends, B. Campbell, Y. Chen, Z. Chen, B. Chiaro, A. Dunsworth, A. G. Fowler, I.-C. Hoi, E. Jeffrey, A. Megrant,

J. Mutus, C. Neill, C. Quintana, P. Roushan, D. Sank, A. Vainsencher, J. Wenner, T. C. White, A. N. Korotkov, A. N. Cleland, and J. M. Martinis, *"Qubit Metrology of Ultralow Phase Noise Using Randomized Benchmarking"*, Physical Review Applied **3**, 044009 (2015).